



Universiteit
Leiden
The Netherlands

Engineered 3D-Vessels-on-Chip to study effects of dynamic fluid flow on human induced pluripotent stem cell derived endothelial cells

Graaf, M.N.S. de

Citation

Graaf, M. N. S. de. (2023, April 6). *Engineered 3D-Vessels-on-Chip to study effects of dynamic fluid flow on human induced pluripotent stem cell derived endothelial cells*. Retrieved from <https://hdl.handle.net/1887/3590465>

Version: Publisher's Version

License: [Licence agreement concerning inclusion of doctoral thesis in the Institutional Repository of the University of Leiden](#)

Downloaded from: <https://hdl.handle.net/1887/3590465>

Note: To cite this publication please use the final published version (if applicable).



Engineered 3D-Vessels-on-Chip
to study effects of dynamic fluid flow on
human induced pluripotent stem cell derived
endothelial cells

Engineered 3D-Vessels-on-Chip to study effects of dynamic fluid flow on
human induced pluripotent stem cell derived endothelial cells

Mees N.S. de Graaf

Mees N.S. de Graaf

Engineered 3D-Vessels-on-Chip
to study effects of dynamic fluid flow on human
induced pluripotent stem cell derived-
endothelial cells

Mees N.S. de Graaf

Colophon

Engineered 3D-Vessels-on-Chip to study effects of dynamic fluid flow on human induced pluripotent stem cell derived-endothelial cells

Mees N.S. de Graaf asserts the moral right to be identified as the author of this work.

ISBN: 978-94-6483-031-6

All rights reserved. No part of this publication may be reproduced stored in a retrieval system or transmitted in any form or any means without permission of the author, or, when applicable, of the publishers of the scientific papers.

The research described in this thesis was conducted at the department of Anatomy & Embryology of the Leiden University Medical Center, Leiden the Netherlands. It was supported by the Dutch Science Council (NWO) under the Gravitation Grant Netherlands-Organ-on-Chip Initiative 'NOCI' Program (Grant no. 424024.003.001)

Printed by Ridderprint | www.ridderprint.nl

Copyright © 2023, M.N.S. de Graaf, Wassenaar,
The Netherlands

**Engineered 3D-Vessels-on-Chip
to study effects of dynamic fluid flow on human
induced pluripotent stem cell derived-endothelial
cells**

Proefschrift

ter verkrijging van
de graad van doctor aan de Universiteit Leiden,
op gezag van rector magnificus prof.dr.ir. H. Bijl,
volgens besluit van het college voor promoties
te verdedigen op donderdag 6 april 2023
klokke 10:00 uur

door
Mees Nicolaas Simon de Graaf
geboren te Weesp
in 1985

Promotor

Prof. Dr. C. L. Mummery

Co-Promotor

Dr. V. V. Orlova

Promotiecommissie

Prof. Dr. P.C.J.J. Passier, Universiteit Twente

Prof. Dr. Ir. A. van den berg, Universiteit Twente

Prof. Dr. A.M.J.M. van den Maagenberg

Prof. Dr. D.J.M. Peters

Prof. Dr. A. D. van der Meer, Universiteit Twente

Dr. M. Mastrangeli, TU Delft

Dr. Ir. B.J. van Meer

Voor Stella, Gia & Luc

Table of Content

1. General Introduction	7
2. Scalable Microphysiological System to Model Three-Dimensional Blood Vessels.....	23
3. Pressure-Driven Perfusion System to Control, Multiplex and Recirculate Cell Culture Medium for Organs-on-Chips.....	55
4. Multiplexed fluidic circuit board for controlled perfusion of 3D blood Vessels-on-a-Chip	83
5. Perfusable Engineered capillary using hydrogel guided self-assembly on-Chip and human iPSC-derived vascular cells.....	125
6. General Discussion	145
7. Addendum.....	157

Chapter one:

General introduction

1.1 Introduction

Blood vessels make up the vascular system of the body. They are crucial for the function of all cells and tissues since they essential oxygen and nutrients and remove waste products¹. The vascular system can be broadly divided into macro-vasculature and the micro vasculature².

The macrovasculature makes up the artery and venous systems and its primary function to distribute blood throughout the body. Vessels of the macrovasculature have diameters ranging from 3 cm at the aorta to 200 μm at smaller arteries and veins. The microvasculature by contrast is much smaller, 200 to 5 μm , and is made up of arterioles, capillaries and venules. This vascular-system directs blood flow to and acts as barrier between blood and individual tissues. Selectivity towards chemical compounds, electrolytes and immune cells of the tissue barriers varies from tissue-to-tissue and conditions³. For instance, a mature blood-brain-barrier (BBB) is a highly selective and controlled barrier that protects brain tissue from a multiplicity high risk pathogens and in general prevents immune cell and drug access^{4,5}. This also means that, for example, chemotherapeutic drugs are unable to cross the BBB, making brain malignancies difficult to treat. By contrast, the kidney-blood- (with small fenestrae or pores) or liver-blood barriers (with sinusoids or large gaps) are not selective at all which allows "sieving" and rapid detoxification of the blood⁶. These phenotypic differences all contribute to sustaining organ functionality and in creating *in vitro* models of the vasculature, it is important that this is also taken into consideration.

Diseases of the vascular system and approaches to therapy

Many diseases are associated with development of aberrant vasculature, either as inducer of disease or collateral damage resulting from other insults to organ tissue. Some are introduced briefly in the following section since they form the underlying reason for building synthetic vessel-on-chip models as described in this thesis. A diseased vasculature can result in many different diseases that range from atherosclerosis⁷, vascular dementia^{8,9} and cancer¹⁰, to haemorrhaging conditions that can be life-threatening¹¹. Aside from chronic conditions mentioned above, diseased vasculature can also lead to a vast range of acute conditions like thrombosis¹², aneurism¹³ and anaphylactic shock^{14,15}, that are difficult to prevent and can have severe outcomes.

One reason that it has been difficult to find therapies and the high failure-rate of drugs that do enter clinical trials is the lack of appropriate pre-clinical models to predict patient specific responses and correctly identify off-target effects¹⁶. Drug discovery worldwide is a multibillion-euro industry that attempts to improve the quality of life for millions of patients¹⁷. Although the industry has the highest standards for patient safety and drug efficacy, almost 90% of developed medicines fail in clinical trials due to unexpected

adverse effects or low efficacy^{18,19}. This imposes risk to patients and loss of valuable resources and time.

In the conventional drug discovery pipeline, candidate drugs are initially extensively tested using a combination of *in vitro* cell cultures and in (humanized) animal models. The most promising then enter the clinical phase, where firstly safety testing begins on small groups of (usually young, male) volunteers (phase I, safety and feasibility) then moves to tests in small groups of patients (phase II, potential efficacy, comparing treated versus untreated groups). At each step, drugs are eliminated and only a small group reach phase III (efficacy in a large, randomized population of patient).

Drug responses are often the result of complex multicellular interplay, the drug delivery route (e.g. intravenous, oral) and metabolic processes for example in the liver contributing to the net effect^{20,21}. Even for drugs that reach the market, only 1 in 10 patients will respond to widely prescribed drugs²². For this reason, the field of pharmacogenetics demonstrated the need for precision and personalized medicine²³.

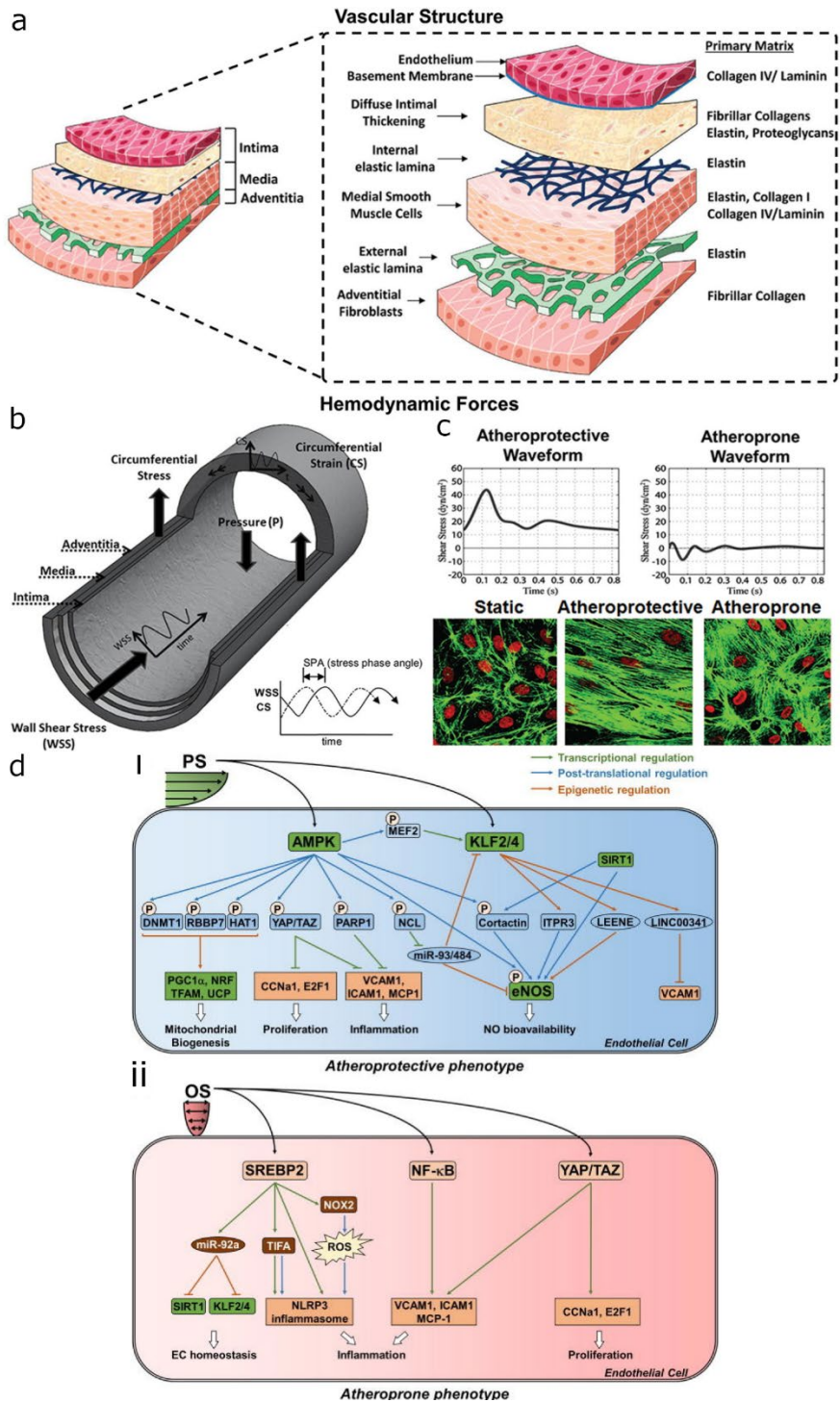
Animal models are useful to test drugs and gain more insight into drug distribution and clearance in a complex system but due in part to interspecies differences, direct translation to humans is often not possible or not relevant for all patients²⁴⁻²⁷. In addition, extensive use of animal models except where absolutely essential is ethically under debate due to animal welfare considerations and legislation in many jurisdictions already requires reduction, refinement and replacement of animal models with ethically acceptable alternatives^{28,29}.

Blood Vessel Anatomy

A blood vessel is composed out of three distinct layers (Figure 1a). The internal vessel wall, or *tunica intima*, is lined with a single layer of Endothelial cells (ECs). The ECs form the barrier between blood and tissue. ECs are phenotypically highly heterogeneous throughout the (human) body and this heterogeneity is controlled by many environmental factors, from surrounding tissue type and growth factors to oxygen levels or mechanical stimuli³⁰.

ECs are surrounded by the *tunica media* which is composed of a basement membrane and pericytes or smooth muscle cells, referred to as mural cells. The mural cells mechanically support ECs and allow efficient blood flow-distribution by contracting and dilating. This changes the vessel diameter and can direct blood according to tissue demands.

The macrovasculature also has an additional layer, the *tunica adventitia*, to support the vessels whereas the microvasculature is embedded inside the organs.



Vascular phenotype

As mentioned earlier, the EC-phenotype is highly heterogenic across the different organs³¹. ECs form a tissue-specific-barrier between circulating blood and the tissue itself that is vital for oxygen and nutrient delivery, waste removal and bidirectional immune-cell trafficking³². For instance, in addition to controlling selective transport the BBB maintains glucose and ion gradients to support high neuronal activity³³. This contrasts with the non-specific blood barrier of the liver and kidney that allows fast detoxification of the body³⁶. These different EC-phenotypes are essential for maintaining organ-homeostasis and because of their different barrier-functions, blood vessels are a major determinant of the absorption, distribution, metabolism excretion (ADME) of drugs and thus determine effective drug doses^{37,38}.

This EC-phenotype tissue specificity is highly plastic and constantly changing under influence of many biological cues that include not only the surrounding tissue cells but also the extracellular matrix (ECM), fluid flow rate and drugs^{30,39,40}.

Haemodynamics are essential pathway modulators

Haemodynamic forces like wall shear stress (WSS) and circumferential stress (CS) are important modulators of cell signal transduction (Figure 1b and c)^{35,41-44}. For instance, different WSS-profiles directly influence the EC-mural cell interactions. WSS is the force parallel to the flow direction exerted on the vessel wall. ECs have multiple different molecular sensors and pathways that can directly detect haemodynamic forces and react to any local differences like primary ciliary⁴⁵, Piezo-1⁴⁶⁻⁴⁸, integrins⁴⁹, cellular junctions⁵⁰.

WSS can have different waveforms for example; unidirectional or oscillatory. Inside an artery an unidirectional flow is considered an athero-protective waveform whereas oscillatory flow is athero-prone for the EC-phenotype (Figure 1b and c)⁵¹. These different waveforms directly control the EC- signal transduction (Figure 1 d). As these different flow patterns modulate important nodes of other signalling pathways, of for instance the TNF-alpha transduction, haemodynamic forces may have major implications in the inflammation response^{52,53}. In standard, static *in vitro* cell culture, exposure of ECs to TNF-alpha results in loss of cell junctions, increasing leucocyte adhesion and apoptosis. When cells are exposed to TNF-alpha combined with unidirectional WSS, the subsequent complex signal transduction pathways result in an opposite, anti-inflammatory responses

Figure 1: Vascular structure and haemodynamic forces. (a) blood vessels typically consist of 3 distinct cellular layers separated by a layer of ECM. (b) Important haemodynamic forces are WSS and circumferential stress (c) different wavefronts result in different cellular morphology. (d) different wavefronts are important modulators of cellular transduction. Unidirectional flow results in an athero-protective phenotype as bidirectional flow can result in an atheroprone phenotype. Figure Panels a, b and c adapted from Pradhan et. al³⁴ Panel d adapted from He et al.³⁵

These differences illustrate the need to account for biomechanical forces in considering drug responses both *in vivo* and *in vitro* models.

Cells used in current *in vitro* models

Broadly speaking, immortalized cell lines or primary cells are used as a basis for developing human models of disease and in early drug screening platforms.

Primary cells derived from donors and generally retain a tissue specific phenotype for a certain time in culture. However, they have a limited capacity for expansion in culture and quickly reach senescence so that eventually only relatively few experiments can be carried out with one cell batch⁵⁶. Donor-to-donor variation and reproducibility of primary cell experiments means that considerable effort is required to create large cell batches or compare new batches with a master cell bank. Furthermore, primary cells can lose important traits when in cell culture, essentially de-differentiating, in part due to missing biochemical and biomechanical signals in their natural environment or 2D culture conditions on hard (plastic) tissue culture substrate⁵⁷.

Immortalized cell lines (either derived from tumors or created by transformation of primary cells in culture through, for example, expression of oncogenes or induction of telomerase activity) bypass cellular senescence and thus can easily be expanded for experimental purposes virtually indefinitely⁵⁸⁻⁶⁰. However, although immortalized cells may retain some cell specific features, important phenotypic traits can be lost or altered during prolonged passage e.g. through genetic drift or acquisition of *de novo* mutations, influencing experimental results⁶¹. These changes in genotype and karyotype limits their use as *bon fide* models and an entirely representative of their tissue of origin⁶²⁻⁶⁴.

Human induced pluripotent stem cells (hiPSC) as *in vitro* models

Human induced pluripotent stem cells (hiPSC) are demonstrating increasing potential as valuable cell sources for drug discovery and disease modelling (Figure 2) ⁶⁵. hiPSC can be derived from virtually every healthy individual or patient by reprogramming somatic cells through the introduction of four transcription factors⁶⁶. Different cell types can be used as a somatic cell source including fibroblasts, peripheral blood cells⁶⁸, hair follicles⁶⁹ or even (kidney)cells that can be collected from urine⁷⁰. These non-invasive methods allow the easy generation of hiPSC lines containing the complete genotype of the individual from whom they were derived. This allows testing of drug effects or building of disease models on a wider range of genetic backgrounds (SNP-variations) prior to clinical studies. Second, hiPSCs are capable of differentiating to all cell types of the human body by administering growth factors, small molecules or ECM in sequences that mimic that in embryonic development.

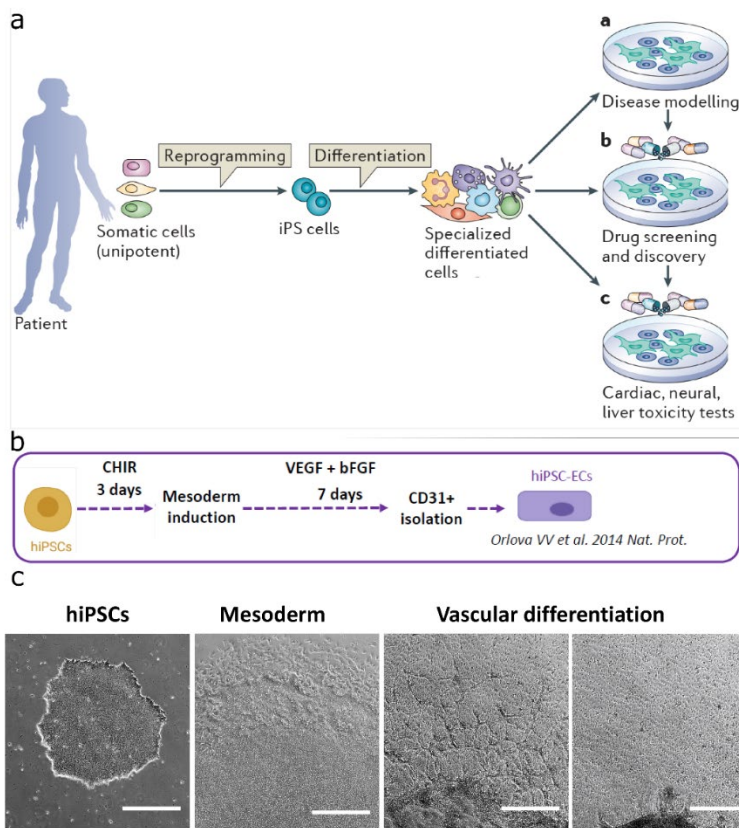
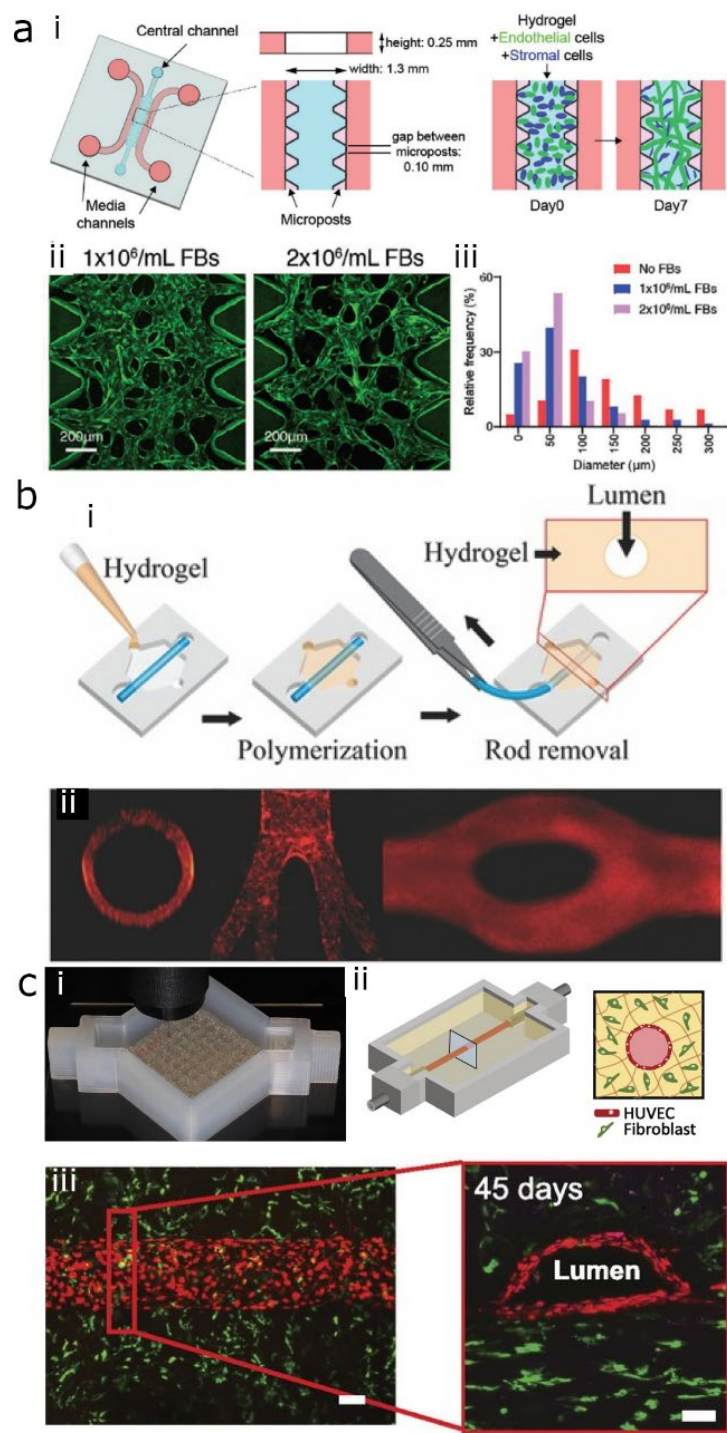


Figure 2: hiPSCs and vascular differentiation. (a) hiPSC can be derived from virtually any patient by reprogramming somatic cells. These pluripotent stem cells can be then differentiated to specialized cells which can be used for either disease modelling, drug discovery and toxicity tests. Figure adapted from Bellin et al. (2012)⁶⁵ (b) Differentiation protocol from hiPSC towards endothelial cells Figure adapted from Marc Vila Cuenca, (c) Widefield images show morphology changes of hiPSCs towards endothelial cells. Figure adapted from Orlova et al (2014)⁶⁷

This allows for the generation of cell types that are difficult to harvest from primary tissue such as neurons and cardiomyocytes because biopsies for these tissues are highly invasive. Thirdly, in the case of genetic diseases caused by known mutations, it is possible to repair the gene of interest using genome editing techniques, particularly CRISPR/Cas9, and generate isogenic controls for comparison without the mutation and also to create isogenic co-cultures where greater *in vitro* tissue complexity is required for the model⁷¹.

Finally, hiPSC have self-renewal capabilities and, when properly maintained, form an unlimited source of undifferentiated cells or banked differentiated cells with less batch-to-batch variation as compared to primary cells, allowing batch-to-batch reproducibility to be measured and more robust experiments. Genetic modification using Crispr/Cas9 techniques also allows the generation



of genetically encoded reporter lines that can be used for various experimental outputs including monitoring changes in structural marker proteins or cellular parameters like calcium flux or membrane potential⁷²⁻⁷⁴.

In vitro differentiation of endothelial cell from hiPSCs starts by inducing mesoderm formation followed by endothelial specification (Figure. 2b)⁶⁷. These differentiation protocols take 10 days and by cell selection yield cryopreserved-vials of pure, isogenic batches of hiPSC-derived ECs ideal for assay development.

Although hiPSC derived ECs have many advantages over primary and immortalized cell lines, they also have disadvantages. hiPSC derivatives are generally considered “immature”, meaning the cells may lack a complete adult organ-specific phenotype. The maturity of the EC-phenotype can be improved by modifying differentiation⁷⁵, co-culturing with tissue specific cells⁷⁶ and the exposure to haemodynamic forces⁷⁷. The following section describes a number of engineered systems that have been examined towards this goal of improving phenotypic realism and increasing maturation state of the hiPSC-derived vessels.

Organ on chip

Microphysiological systems (MPS) or “Organs-on-a-Chip” (OoC), are being developed to combine different biological cues and biomechanical stimuli to promote mature cellular responses *in vitro* that resemble those *in vivo*⁷⁸. Different OoCs are being developed from different organs: Heart-on-Chip, Gut-on-Chip, and Brain-on-Chip are already advanced models for this purpose and are increasingly used to investigate aspects of human physiology. Different OoCs can also be combined to investigate how different organs influence each other⁷⁹.

3D-Vessel on chips

As the vasculature is a vital component of every organ, different types of Vessel-on-Chips (VoCs) and Organ-barriers are being developed to mimic for example the BBB^{80,81}, glomerular -barrier^{82,83}, alveolar-barrier⁸⁴⁻⁸⁶ and the placenta-barrier on-Chip⁸⁷. Many methods are being used for VoCs to combine different tissue-specific cell types with multiple vascular cell types and include haemodynamic forces like those *in vivo*. These methods include self-assembly or self-organization of the vascular cells in various types of

Figure 3: Common methodologies to engineer 3D-VoCs. (a)(i) Cellular self-assembly comprises of mixing vascular and tissue specific cells with ECM. **(ii)(iii)** network formation is depending on cellular composition adapted from Wan et al. (2022)⁸⁸. **(b) (i)** Template casting comprises of casting ECM around a tubular template. **(ii)** cell can be seeded in the resulting lumen. Figure adapted from Jimenez-torres et al (2016)⁹⁰(c)(i)(ii) Bioprinting allows the formation of complex 3D structures **(iii)** multiple cell types can be cultured for extended periods of time, however shape of cross-sectional flow fields depend on bio-ink parameters, figure adapted from Kolesky et al (2016)⁹³

chambers or devices^{80,88,89}, template “casting”⁹⁰⁻⁹² and 3D bioprinting⁹³. Each of these methods has their advantages and disadvantages and different approaches are used to investigate different aspects of vascular function or development. Cellular self-assembly has been a widely adopted methodology where ECs are mixed with ECM and allowed to form a 3D capillary bed autonomously (Figure 3a)⁸⁹. Different cell types can be combined in different ECMs to model for example a microvascular BBB⁸⁰. However, these self-assembled capillary beds, have one major limitation: there is no spatial control of the capillary bed and therefore all samples have different geometries and diameters. This variation makes it difficult to introduce uniform haemodynamic forces as every cell in the systems experiences these differently depending on their position and the diameter of the vessel in which they are situated⁹⁴. To include controlled haemodynamics forces, scaffolds can be engineered with more defined geometries. Cells can be seeded into these scaffolds in any combination and density. The scaffolds can be fabricated for example using template casting⁹⁰ or 3D bioprinting^{93,95} (Figure 3b and c). By simply casting a hydrogel around a tube-like template, like a hypodermic needle, scaffolds can be engineered that are suitable quickly and easily suitable for cell seeding. 3D-bioprinting allows the engineering of higher order structures which can also be used to model the complex flow patterns observed for instance at vascular bifurcations. Although these methods allow the inclusion of all aspects of the vasculature, the vessels in the models are typically larger than *in vivo*⁹⁶ which could impact how cells interact with each other and how scaling of the haemodynamic forces and metabolic parameters is carried out⁹⁷.

Current limitations of VoC models

Although many methods support the generation of complex 3D vascular models, their adoption is still rather limited to biomedical research. This is because many methods have been developed as proof-of-concept but not with the intention to be low tech and easy to implement. Adoption by non-specialist labs is often limited: methodologies are complex, not scalable, require specialised equipment and expertise or the reagents and tools are expensive⁹⁸.

1.2 Aim and scope of this Thesis

To improve the predictive power of *in vitro* models, vascular biology needs to be integrated into functional and preferably facile technology. This thesis describes the development of 3D microfluidic blood Vessel-on-Chip models that can be used for applications such as disease modelling and drug discovery. The cellular components of the VoCs are derived from hiPSCs and consist of vascular ECs and pericytes. The methods were developed to include adjustable microfluidic flow that can mimic haemodynamic forces of different blood vessels with different diameters and the option to incorporate additional tissue specific cells, which expands the flexibility of the technology.

The overall aim is to improve cellular responses such that it more closely resembles that of vascular cells in blood vessels in health and disease.

In **Chapter 2**, a method is described on to generate 3D VoCs suitable for hiPSC-derived vascular cells. It optimizes an existing protocol that employs a microfluidic technique called viscous finger patterning (VFP) and it overcomes two mayor limitations of current techniques: it is a scalable method that does not require the use of highly specialized equipment or expertise and it is capable of generating uniform haemodynamic forces within the vascular architectures over extended lengths that to date have not been achieved.

Chapter 3 describes a custom PID-controller that controls the perfusion of microfluidic OoCs. This controller is essential for the perfusion and recirculation of the developed fluidic circuit board. It represents an advance on current software control of this type of system.

In **Chapter 4** a multiplexing Fluidic Circuit Board (FCB) is described that is capable of generating equal wall shear stress in parallel to 3D-VoCs with intrinsic diameter variation. The FCB also allows the control of circumferential stress the 3D-VoCs which can be used to model different (patho-) physiological conditions.

Chapter 5 describes on the development of a realistically-sized vascular capillary network model. The methodology combines mask-less photolithography techniques and cellular self-assembly to engineer true 3D vascular capillary mimics.

Together, the research described in this thesis, provides significant practical and theoretical advances that can improve the utility of VoC systems to biological laboratories. This type of multidisciplinary link between device engineering and testing cells increasingly used in biomedical research because they are representative human disease models, will contribute to more widespread adoption of OoC technology. This is considered in more depth in the General Discussion in **Chapter 6**.

References

- 1 Reiterer, M. & Branco, C. M. Endothelial cells and organ function: applications and implications of understanding unique and reciprocal remodelling. *Febs J* **287**, 1088-1100, doi:10.1111/febs.15143 (2020).
- 2 Climie, R. E. *et al.* Macrovasculature and Microvasculature at the Crossroads Between Type 2 Diabetes Mellitus and Hypertension. *Hypertension* **73**, 1138-1149, doi:10.1161/HYPERTENSIONAHA.118.11769 (2019).
- 3 Aird, W. C. Phenotypic heterogeneity of the endothelium: I. Structure, function, and mechanisms. *Circ Res* **100**, 158-173, doi:10.1161/01.RES.0000255691.76142.4a (2007).
- 4 Abbott, N. J., Ronnback, L. & Hansson, E. Astrocyte-endothelial interactions at the blood-brain barrier. *Nat Rev Neurosci* **7**, 41-53, doi:10.1038/nrn1824 (2006).
- 5 Pardridge, W. M. Molecular biology of the blood-brain barrier. *Mol Biotechnol* **30**, 57-70, doi:10.1385/MB:30:1:057 (2005).
- 6 Aird, W. C. Phenotypic heterogeneity of the endothelium: II. Representative vascular beds. *Circ Res* **100**, 174-190, doi:10.1161/01.RES.0000255690.03436.ae (2007).
- 7 Libby, P., Aikawa, M. & Jain, M. K. 285-306 (Springer Berlin Heidelberg).
- 8 Wang, F. *et al.* Dysfunction of Cerebrovascular Endothelial Cells: Prelude to Vascular Dementia. *Front Aging Neurosci* **10**, 376, doi:10.3389/fnagi.2018.00376 (2018).
- 9 Quick, S., Moss, J., Rajani, R. M. & Williams, A. A Vessel for Change: Endothelial Dysfunction in Cerebral Small Vessel Disease. *Trends Neurosci* **44**, 289-305, doi:10.1016/j.tins.2020.11.003 (2021).
- 10 Nikitenko, L. & Boshoff, C. 307-334 (Springer Berlin Heidelberg).
- 11 Mackow, E. R., Gorbunova, E. E. & Gavrilovskaya, I. N. Endothelial cell dysfunction in viral hemorrhage and edema. *Front Microbiol* **5**, 733, doi:10.3389/fmicb.2014.00733 (2014).
- 12 Wang, M., Hao, H., Leeper, N. J., Zhu, L. & Early Career, C. Thrombotic Regulation From the Endothelial Cell Perspectives. *Arterioscler Thromb Vasc Biol* **38**, e90-e95, doi:10.1161/ATVBAHA.118.310367 (2018).
- 13 Sheinberg, D. L. *et al.* Endothelial dysfunction in cerebral aneurysms. *Neurosurg Focus* **47**, E3, doi:10.3171/2019.4.FOCUS19221 (2019).
- 14 Hou, P. C. *et al.* Endothelial Permeability and Hemostasis in Septic Shock: Results From the ProCESS Trial. *Chest* **152**, 22-31, doi:10.1016/j.chest.2017.01.010 (2017).
- 15 Joffe, J., Hellman, J., Ince, C. & Ait-Oufella, H. Endothelial Responses in Sepsis. *Am J Respir Crit Care Med* **202**, 361-370, doi:10.1164/rccm.201910-1911TR (2020).
- 16 Sun, D., Gao, W., Hu, H. & Zhou, S. Why 90% of clinical drug development fails and how to improve it? *Acta Pharm Sin B* **12**, 3049-3062, doi:10.1016/j.apsb.2022.02.002 (2022).
- 17 DiMasi, J. A., Grabowski, H. G. & Hansen, R. W. Innovation in the pharmaceutical industry: New estimates of R&D costs. *J Health Econ* **47**, 20-33, doi:10.1016/j.jhealeco.2016.01.012 (2016).
- 18 Dowden, H. & Munro, J. Trends in clinical success rates and therapeutic focus. *Nat Rev Drug Discov* **18**, 495-496, doi:10.1038/d41573-019-00074-z (2019).
- 19 Harrison, R. K. Phase II and phase III failures: 2013-2015. *Nat Rev Drug Discov* **15**, 817-818, doi:10.1038/nrd.2016.184 (2016).
- 20 Rautio, J. *et al.* Prodrugs: design and clinical applications. *Nat Rev Drug Discov* **7**, 255-270, doi:10.1038/nrd2468 (2008).
- 21 Rautio, J., Meanwell, N. A., Di, L. & Hageman, M. J. The expanding role of prodrugs in contemporary drug design and development. *Nat Rev Drug Discov* **17**, 559-587, doi:10.1038/nrd.2018.46 (2018).
- 22 Schork, N. J. Personalized medicine: Time for one-person trials. *Nature* **520**, 609-611, doi:10.1038/520609a (2015).
- 23 Roses, A. D. Genome-based pharmacogenetics and the pharmaceutical industry. *Nat Rev Drug Discov* **1**, 541-549, doi:10.1038/nrd840 (2002).
- 24 Jansen, K., Pou Casellas, C., Groenink, L., Wever, K. E. & Masereeuw, R. Humans are animals, but are animals human enough? A systematic review and meta-analysis on interspecies differences in renal drug clearance. *Drug Discov Today* **25**, 706-717, doi:10.1016/j.drudis.2020.01.018 (2020).
- 25 Franjic, D. *et al.* Transcriptomic taxonomy and neurogenic trajectories of adult human, macaque, and pig hippocampal and entorhinal cells. *Neuron* **110**, 452-469 e414, doi:10.1016/j.neuron.2021.10.036 (2022).
- 26 Carr, J. & Wilhelm, D. L. Interspecies Differences in Response to Polypeptides as Permeability Factors. *Nature* **208**, 653-&, doi:DOI 10.1038/208653a0 (1965).

- 27 Robinson, N. B. *et al.* The current state of animal models in research: A review. *Int J Surg* **72**, 9-13, doi:10.1016/j.ijssu.2019.10.015 (2019).
- 28 Reduce, refine, replace. *Nat Immunol* **11**, 971, doi:10.1038/nri1110-971 (2010).
- 29 Kirschner, K. M. Reduce, replace, refine-Animal experiments. *Acta Physiol (Oxf)* **233**, e13726, doi:10.1111/apha.13726 (2021).
- 30 Aird, W. C. Endothelial cell heterogeneity. *Cold Spring Harb Perspect Med* **2**, a006429, doi:10.1101/cshperspect.a006429 (2012).
- 31 Kalucka, J. *et al.* Single-Cell Transcriptome Atlas of Murine Endothelial Cells. *Cell* **180**, 764-779 e720, doi:10.1016/j.cell.2020.01.015 (2020).
- 32 Muller, W. A. Leukocyte-endothelial-cell interactions in leukocyte transmigration and the inflammatory response. *Trends Immunol* **24**, 327-334, doi:10.1016/s1471-4906(03)00117-0 (2003).
- 33 Daneman, R. & Prat, A. The Blood-Brain Barrier. *Cold Spring Harbor Perspectives in Biology* **7**, a020412, doi:10.1101/cshperspect.a020412 (2015).
- 34 Pradhan, S. *et al.* Biofabrication Strategies and Engineered In Vitro Systems for Vascular Mechanobiology. *Adv Healthc Mater* **9**, e1901255, doi:10.1002/adhm.201901255 (2020).
- 35 He, M., Martin, M., Marin, T., Chen, Z. & Gongol, B. Endothelial mechanobiology. *APL Bioeng* **4**, 010904, doi:10.1063/1.5129563 (2020).
- 36 Poisson, J. *et al.* Liver sinusoidal endothelial cells: Physiology and role in liver diseases. *Journal of Hepatology* **66**, 212-227, doi:https://doi.org/10.1016/j.jhep.2016.07.009 (2017).
- 37 Tibbitts, J., Canter, D., Graff, R., Smith, A. & Khawli, L. A. Key factors influencing ADME properties of therapeutic proteins: A need for ADME characterization in drug discovery and development. *mAbs* **8**, 229-245, doi:10.1080/19420862.2015.1115937 (2016).
- 38 Vugmeyster, Y., Harrold, J. & Xu, X. Absorption, Distribution, Metabolism, and Excretion (ADME) Studies of Biotherapeutics for Autoimmune and Inflammatory Conditions. *The AAPS Journal* **14**, 714-727, doi:10.1208/s12248-012-9385-y (2012).
- 39 Aird, W. C. Spatial and temporal dynamics of the endothelium. *J Thromb Haemost* **3**, 1392-1406, doi:10.1111/j.1538-7836.2005.01328.x (2005).
- 40 Langenkamp, E. & Molema, G. Microvascular endothelial cell heterogeneity: general concepts and pharmacological consequences for anti-angiogenic therapy of cancer. *Cell Tissue Res* **335**, 205-222, doi:10.1007/s00441-008-0642-4 (2009).
- 41 Anwar, M. A., Shalhoub, J., Lim, C. S., Gohel, M. S. & Davies, A. H. The effect of pressure-induced mechanical stretch on vascular wall differential gene expression. *J Vasc Res* **49**, 463-478, doi:10.1159/000339151 (2012).
- 42 Chatterjee, S. Endothelial Mechanotransduction, Redox Signaling and the Regulation of Vascular Inflammatory Pathways. *Front Physiol* **9**, 524, doi:10.3389/fphys.2018.00524 (2018).
- 43 Gordon, E., Schimmel, L. & Frye, M. The Importance of Mechanical Forces for in vitro Endothelial Cell Biology. *Front Physiol* **11**, 684, doi:10.3389/fphys.2020.00684 (2020).
- 44 Shirinsky, V. P. *et al.* Mechano-chemical control of human endothelium orientation and size. *J Cell Biol* **109**, 331-339, doi:10.1083/jcb.109.1.331 (1989).
- 45 Hierck, B. P. *et al.* Primary cilia sensitize endothelial cells for fluid shear stress. *Dev Dyn* **237**, 725-735, doi:10.1002/dvdy.21472 (2008).
- 46 Ranade, S. S. *et al.* Piezo1, a mechanically activated ion channel, is required for vascular development in mice. *Proc Natl Acad Sci U S A* **111**, 10347-10352, doi:10.1073/pnas.1409233111 (2014).
- 47 Wang, S. *et al.* Mechanosensation by endothelial PIEZO1 is required for leukocyte diapedesis. *Blood* **140**, 171-183, doi:10.1182/blood.2021014614 (2022).
- 48 Friedrich, E. E. *et al.* Endothelial cell Piezo1 mediates pressure-induced lung vascular hyperpermeability via disruption of adherens junctions. *Proc Natl Acad Sci U S A* **116**, 12980-12985, doi:10.1073/pnas.1902165116 (2019).
- 49 Shyy, J. Y. & Chien, S. Role of integrins in endothelial mechanosensing of shear stress. *Circ Res* **91**, 769-775, doi:10.1161/01.res.0000038487.19924.18 (2002).
- 50 Wallez, Y. & Huber, P. Endothelial adherens and tight junctions in vascular homeostasis, inflammation and angiogenesis. *Biochim Biophys Acta* **1778**, 794-809, doi:10.1016/j.bbame.2007.09.003 (2008).
- 51 Dai, G. *et al.* Distinct endothelial phenotypes evoked by arterial waveforms derived from atherosclerosis-susceptible and -resistant regions of human vasculature. *Proc Natl Acad Sci U S A* **101**, 14871-14876, doi:10.1073/pnas.0406073101 (2004).
- 52 Urschel, K., Worner, A., Daniel, W. G., Garlich, C. D. & Cicha, I. Role of shear stress patterns in the TNF-alpha-induced atherogenic protein expression and monocytic cell adhesion to endothelium. *Clin Hemorheol Microcirc* **46**, 203-210, doi:10.3233/CH-2010-1346 (2010).

- 53 Garin, G. *et al.* Flow antagonizes TNF- α signaling in endothelial cells by inhibiting caspase-dependent PKC ζ processing. *Circ Res* **101**, 97-105, doi:10.1161/CIRCRESAHA.107.148270 (2007).
- 54 Cicha, I. & Urschel, K. TNF- α in the cardiovascular system: from physiology to therapy. *International Journal of Interferon, Cytokine and Mediator Research*, **9**, doi:10.2147/ijcmr.s64894 (2015).
- 55 Yamawaki, H., Lehoux, S. & Berk, B. C. Chronic physiological shear stress inhibits tumor necrosis factor-induced proinflammatory responses in rabbit aorta perfused ex vivo. *Circulation* **108**, 1619-1625, doi:10.1161/01.Cir.0000089373.49941.C4 (2003).
- 56 Gillooly, J. F., Hayward, A., Hou, C. & Burleigh, J. G. Explaining differences in the lifespan and replicative capacity of cells: a general model and comparative analysis of vertebrates. *Proc Biol Sci* **279**, 3976-3980, doi:10.1098/rspb.2012.1129 (2012).
- 57 Berthier, E., Young, E. W. & Beebe, D. Engineers are from PDMS-land, Biologists are from Polystyrenia. *Lab Chip* **12**, 1224-1237, doi:10.1039/c2lc20982a (2012).
- 58 Bodnar, A. G. *et al.* Extension of Life-Span by Introduction of Telomerase into Normal Human Cells. *Science* **279**, 349-352, doi:10.1126/science.279.5349.349 (1998).
- 59 Kwakkenbos, M. J., Helden, P. M., Beaumont, T. & Spits, H. Stable long-term cultures of self-renewing B cells and their applications. *Immunological Reviews* **270**, 65-77, doi:10.1111/imr.12395 (2016).
- 60 Henle, W. & Henle, G. Epidemiologic aspects of epstein-barr virus (ebv)-associated diseases. *Annals of the New York Academy of Sciences* **354**, 326-331, doi:10.1111/j.1749-6632.1980.tb27975.x (1980).
- 61 Balzer, V. *et al.* Re-evaluation of the hCMEC/D3 based in vitro BBB model for ABC transporter studies. *Eur J Pharm Biopharm* **173**, 12-21, doi:10.1016/j.ejpb.2022.02.017 (2022).
- 62 Mkrtchyan, H. *et al.* Molecular cytogenetic characterization of the human cerebral microvessel endothelial cell line hCMEC/D3. *Cytogenet Genome Res* **126**, 313-317, doi:10.1159/000253080 (2009).
- 63 Landry, J. J. *et al.* The genomic and transcriptomic landscape of a HeLa cell line. *G3 (Bethesda)* **3**, 1213-1224, doi:10.1534/g3.113.005777 (2013).
- 64 Frattini, A. *et al.* High variability of genomic instability and gene expression profiling in different HeLa clones. *Sci Rep* **5**, 15377, doi:10.1038/srep15377 (2015).
- 65 Bellin, M., Marchetto, M. C., Gage, F. H. & Mummery, C. L. Induced pluripotent stem cells: the new patient? *Nat Rev Mol Cell Biol* **13**, 713-726, doi:10.1038/nrm3448 (2012).
- 66 Takahashi, K. *et al.* Induction of pluripotent stem cells from adult human fibroblasts by defined factors. *Cell* **131**, 861-872, doi:10.1016/j.cell.2007.11.019 (2007).
- 67 Orlova, V. V. *et al.* Generation, expansion and functional analysis of endothelial cells and pericytes derived from human pluripotent stem cells. *Nat Protoc* **9**, 1514-1531, doi:10.1038/nprot.2014.102 (2014).
- 68 Staerk, J. *et al.* Reprogramming of human peripheral blood cells to induced pluripotent stem cells. *Cell Stem Cell* **7**, 20-24, doi:10.1016/j.stem.2010.06.002 (2010).
- 69 Maherali, N. *et al.* A high-efficiency system for the generation and study of human induced pluripotent stem cells. *Cell Stem Cell* **3**, 340-345, doi:10.1016/j.stem.2008.08.003 (2008).
- 70 Zhou, T. *et al.* Generation of human induced pluripotent stem cells from urine samples. *Nat Protoc* **7**, 2080-2089, doi:10.1038/nprot.2012.115 (2012).
- 71 Bassett, A. R. Editing the genome of hiPSC with CRISPR/Cas9: disease models. *Mammalian Genome* **28**, 348-364, doi:10.1007/s00335-017-9684-9 (2017).
- 72 Yiangou, L. *et al.* Optogenetic Reporters Delivered as mRNA Facilitate Repeatable Action Potential and Calcium Handling Assessment in Human iPSC-Derived Cardiomyocytes. *Stem Cells* **40**, 655-668, doi:10.1093/stmcls/sxac029 (2022).
- 73 Sun, Y.-H. *et al.* Human induced pluripotent stem cell line with genetically encoded fluorescent voltage indicator generated via CRISPR for action potential assessment post-cardiogenesis. *Stem Cells* **38**, 90-101, doi:10.1002/stem.3085 (2020).
- 74 Jiang, Y. *et al.* An Ultrasensitive Calcium Reporter System via CRISPR-Cas9-Mediated Genome Editing in Human Pluripotent Stem Cells. *iScience* **9**, 27-35, doi:10.1016/j.isci.2018.10.007 (2018).
- 75 Rosa, S. *et al.* Functional characterization of iPSC-derived arterial- and venous-like endothelial cells. *Sci Rep* **9**, 3826, doi:10.1038/s41598-019-40417-9 (2019).
- 76 Helle, E. *et al.* HiPS-Endothelial Cells Acquire Cardiac Endothelial Phenotype in Co-culture With hiPS-Cardiomyocytes. *Front Cell Dev Biol* **9**, 715093, doi:10.3389/fcell.2021.715093 (2021).
- 77 Helle, E., Ampuja, M., Antola, L. & Kivela, R. Flow-Induced Transcriptomic Remodeling of Endothelial Cells Derived From Human Induced Pluripotent Stem Cells. *Front Physiol* **11**, 591450, doi:10.3389/fphys.2020.591450 (2020).

- 78 Ingber, D. E. Human organs-on-chips for disease modelling, drug development and personalized medicine. *Nat Rev Genet* **23**, 467-491, doi:10.1038/s41576-022-00466-9 (2022).
- 79 Cochrane, A. *et al.* Advanced in vitro models of vascular biology: Human induced pluripotent stem cells and organ-on-chip technology. *Adv Drug Deliv Rev* **140**, 68-77, doi:10.1016/j.addr.2018.06.007 (2019).
- 80 Adriani, G., Ma, D., Pavesi, A., Kamm, R. D. & Goh, E. L. A 3D neurovascular microfluidic model consisting of neurons, astrocytes and cerebral endothelial cells as a blood-brain barrier. *Lab Chip* **17**, 448-459, doi:10.1039/c6lc00638h (2017).
- 81 Herland, A. *et al.* Distinct Contributions of Astrocytes and Pericytes to Neuroinflammation Identified in a 3D Human Blood-Brain Barrier on a Chip. *Plos One* **11**, e0150360, doi:10.1371/journal.pone.0150360 (2016).
- 82 Petrosyan, A. *et al.* A glomerulus-on-a-chip to recapitulate the human glomerular filtration barrier. *Nature Communications* **10**, doi:10.1038/s41467-019-11577-z (2019).
- 83 Musah, S. *et al.* Mature induced-pluripotent-stem-cell-derived human podocytes reconstitute kidney glomerular-capillary-wall function on a chip. *Nat Biomed Eng* **1**, 0069, doi:10.1038/s41551-017-0069 (2017).
- 84 Zamprogno, P. *et al.* Second-generation lung-on-a-chip with an array of stretchable alveoli made with a biological membrane. *Commun Biol* **4**, doi:10.1038/s42003-021-01695-0 (2021).
- 85 Stucki, A. O. *et al.* A lung-on-a-chip array with an integrated bio-inspired respiration mechanism. *Lab Chip* **15**, 1302-1310, doi:10.1039/c4lc01252f (2015).
- 86 Huh, D. *et al.* Reconstituting Organ-Level Lung Functions on a Chip. *Science* **328**, 1662-1668, doi:doi:10.1126/science.1188302 (2010).
- 87 Blundell, C. *et al.* Placental Drug Transport-on-a-Chip: A Microengineered In Vitro Model of Transporter-Mediated Drug Efflux in the Human Placental Barrier. *Adv Healthc Mater* **7**, 1700786, doi:10.1002/adhm.201700786 (2018).
- 88 Wan, Z. *et al.* A Robust Method for Perfusable Microvascular Network Formation In Vitro. *Small Methods* **6**, e2200143, doi:10.1002/smt.202200143 (2022).
- 89 Vila Cuenca, M. *et al.* Engineered 3D vessel-on-chip using iPSC-derived endothelial- and vascular smooth muscle cells. *Stem Cell Rep* **16**, 2159-2168, doi:10.1016/j.stemcr.2021.08.003 (2021).
- 90 Jimenez-Torres, J. A., Peery, S. L., Sung, K. E. & Beebe, D. J. LumeNEXT: A Practical Method to Pattern Luminal Structures in ECM Gels. *Adv Healthc Mater* **5**, 198-204, doi:10.1002/adhm.201500608 (2016).
- 91 Arik, Y. B. *et al.* Microfluidic organ-on-a-chip model of the outer blood-retinal barrier with clinically relevant read-outs for tissue permeability and vascular structure. *Lab Chip* **21**, 272-283, doi:10.1039/d0lc00639d (2021).
- 92 Dessalles, C. A., Ramon-Lozano, C., Babataheri, A. & Barakat, A. I. Luminal flow actuation generates coupled shear and strain in a microvessel-on-chip. *Biofabrication* **14**, doi:10.1088/1758-5090/ac2baa (2021).
- 93 Kolesky, D. B., Homan, K. A., Skylar-Scott, M. A. & Lewis, J. A. Three-dimensional bioprinting of thick vascularized tissues. *Proc Natl Acad Sci U S A* **113**, 3179-3184, doi:10.1073/pnas.1521342113 (2016).
- 94 Kim, S., Lee, H., Chung, M. & Jeon, N. L. Engineering of functional, perfusable 3D microvascular networks on a chip. *Lab Chip* **13**, 1489-1500, doi:10.1039/c3lc41320a (2013).
- 95 Kolesky, D. B. *et al.* 3D bioprinting of vascularized, heterogeneous cell-laden tissue constructs. *Adv Mater* **26**, 3124-3130, doi:10.1002/adma.201305506 (2014).
- 96 Barrs, R. W., Jia, J., Silver, S. E., Yost, M. & Mei, Y. Biomaterials for Bioprinting Microvasculature. *Chemical Reviews* **120**, 10887-10949, doi:10.1021/acs.chemrev.0c00027 (2020).
- 97 Wikswo, J. P. *et al.* Scaling and systems biology for integrating multiple organs-on-a-chip. *Lab Chip* **13**, 3496, doi:10.1039/c3lc50243k (2013).
- 98 Busek, M., Aizenshtadt, A., Amirolo-Martinez, M., Delon, L. & Krauss, S. Academic User View: Organ-on-a-Chip Technology. *Biosensors* **12**, 126, doi:10.3390/bios12020126 (2022).

Chapter two:

Scalable Microphysiological System to Model Three-Dimensional Blood Vessels

Mees N. S. de Graaf¹, Amy Cochrane¹, Francijna E. van den Hil¹, Wesley Buijsman^{2,3}, Andries D. van der Meer², Albert van den Berg³, Christine L. Mummery^{1,2}, Valeria V. Orlova¹

¹ Department of Anatomy and Embryology, Leiden University Medical Center

² Applied Stem Cell Technologies, University of Twente

³ BIOS Lab on a Chip, University of Twente

Published in APL Bioengineering 3, 026105 (2019);
<https://doi.org/10.1063/1.5090986>



Abstract

Blood vessel models are increasingly recognized as having value in understanding disease and drug discovery. However, continued improvements are required to more accurately reflect human vessel physiology. Realistic three-dimensional (3D) in vitro cultures of human vascular cells inside microfluidic chips, or vessels-on-chips (VoC), could contribute to this since they can recapitulate aspects of the in vivo microenvironment by including mechanical stimuli such as shear stress. Here, we used human induced pluripotent stem cells as a source of endothelial cells (hiPSC-ECs), in combination with a technique called viscous finger patterning (VFP) towards this goal. We optimised VFP to create hollow structures in collagen I extracellular-matrix inside microfluidic chips. Lumen formation success rate was over 90% and the resulting cellularized lumens had a consistent diameter over their full length, averaging $336 \pm 15 \mu\text{m}$. Importantly, hiPSC-ECs cultured in these 3D microphysiological systems formed stable and viable vascular structures within 48 hours. Furthermore, this system could support co-culture of hiPSC-ECs with primary human brain vascular pericytes (HBVPs), demonstrating their ability to accommodate biologically relevant combinations of multiple vascular cell types. Our protocol for VFP is more robust than previously published methods with respect to success rates and reproducibility of diameter between- and within channels. This, in combination with the ease of preparation, makes hiPSC-EC based VoC a low-cost platform for future studies in personalised disease modelling.

2.1 Introduction

Blood vessels are lined with endothelial cells (ECs) and surrounded by mural cells called smooth muscle cells or pericytes. The interaction between mural cells and ECs provides many vessels with stability and abnormal interactions can lead to conditions such as haemorrhage, vascular dementia and chronic infection¹⁻³. Furthermore, EC and mural cell interaction influences the selectivity of the barrier, which determines whether compounds can enter or are excluded from an organ, and they are therefore important factors in drug efficacy and tissue selectivity^{4,5}. Studying interaction between ECs and mural cells can be complex; for instance, combining three-dimensional (3D) geometry and controlled fluid flow is challenging *in vitro*. Pseudo-capillary vascular networks can be generated when culturing vascular cells in conventional two-dimensional (2D) tissue culture plastic dishes but these lack the lumen of vasculature *in vivo*^{6,7}. By contrast, ECs can self-organize in 3D culture environments into complex vascular capillary networks in which a perfusable lumen develops with diameters ranging from approximately 10 μm (the size of an *in vivo* capillary) to 100 μm ⁸. However, precise control of the network geometry during self-organization is challenging and this creates intrinsic variation in wall shear stress when fluid flow is introduced. Wall shear stress is an important determinant of vascular function⁹. Its magnitude can be estimated by assuming blood vessels are straight cylinders with a constant flow rate and viscosity, using the following equation ^{8,10}:

$$\tau = \frac{32 \mu Q}{\pi d^3} \quad (1)$$

(Where τ : shear stress [Pa], μ : viscosity of the fluid [Pa * s], Q: flow rate [m^3/s], d: diameter [m])

In order to generate 3D vessels as experimentally tractable models with controlled geometries, techniques other than self-organization are necessary. Microphysiological systems (MPS) have been reported in which vascular cells are cultured in large-diameter, patterned 3D lumen inside a microfluidic chip¹¹. These MPS are also referred to as 'vessel-on-chip' (VoC) systems. Many different engineering techniques are being developed to produce more complex MPS. Most often, VoCs are fabricated by patterning an extracellular matrix with a small-diameter needle^{12,13}. This method yields reproducible lumens using straightforward methodology but scaling up of experiments is labour intensive and removing the template without disturbing the structure is challenging. An alternative method is viscous finger patterning (VFP). VFP is a microfluidic technique that exploits the difference in viscosity between two fluids to generate a scaffold that can be used for cell culture¹⁴⁻¹⁶. When a less viscous fluid displaces a viscous fluid in a confined channel, the less viscous fluid flows in a "finger-like" shape through the middle of the channel; this is referred to as the Saffman-Taylor finger (Figure 1*bi-iii*)¹⁷. When the viscous fluid is a soluble hydrogel that can gelate, this results in a hollow

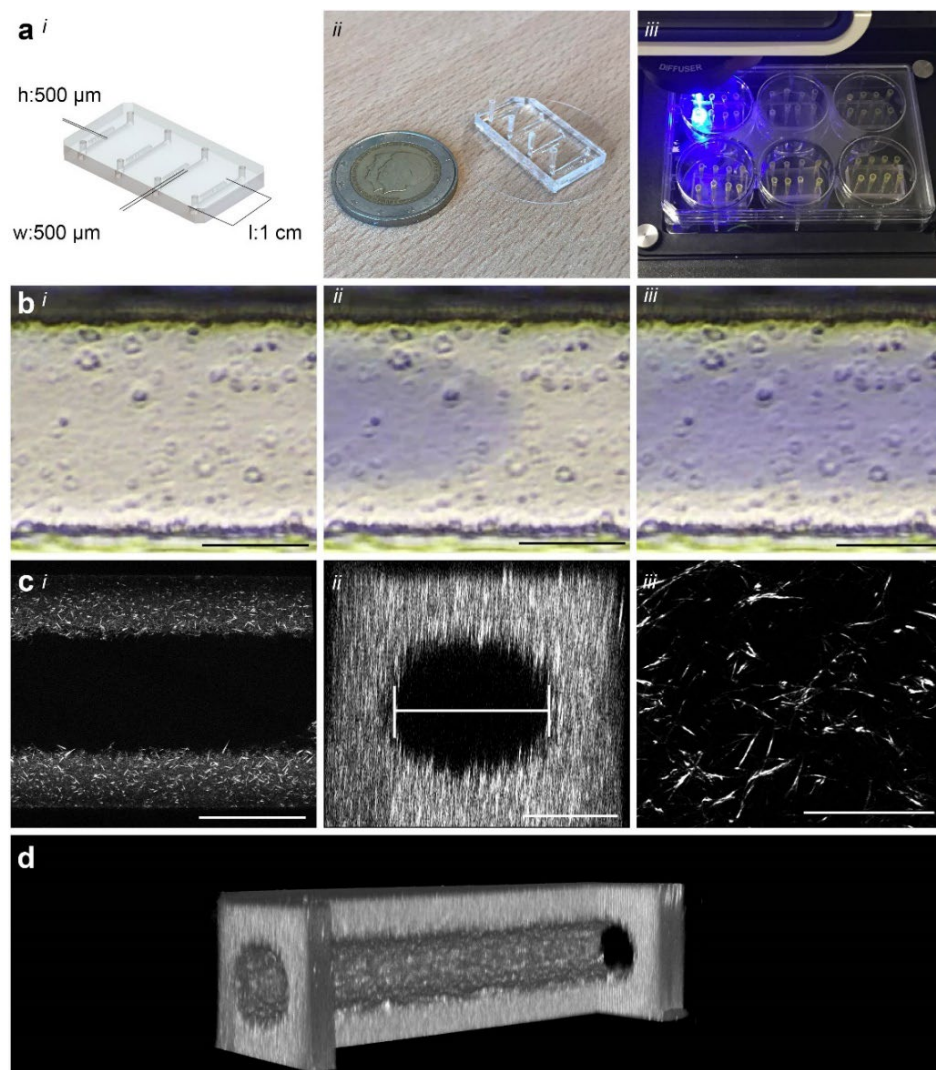


Figure 1: Microfluidic design and patterning collagen scaffold. (a). (i) Schematic of the microfluidic chip showing dimensions and layout of the microfluidic platform, four straight channels on a single chip with designed parameters $500\ \mu\text{m} \times 500\ \mu\text{m} \times 1\ \text{cm}$ ($w \times h \times l$) (ii) Photograph of the real microfluidic device showing four channels ready to be patterned, two-euro coin as size reference (iii) Photograph demonstrating ease of use and medium throughput capacity of this setup. The microfluidic device fits in 6-well plates allowing analyses medium throughput in a conventional biological workflow. Manual preparation of patterning of these 24 lumens is typically 10 minutes. (b) Time-lapse of Viscous finger patterning images showing PBS with blue food dye travelling through collagen solution in a $500\ \mu\text{m}$ wide channel (i) $t=0$ collagen is injected (ii) PBS finger travels through the channel (iii) PBS-finger has completely traversed the channel and displaced the centre of the collagen (c) (i) 20x magnification confocal slice of a patterned lumen with $5\ \text{mg/ml}$ collagen I; note the absence of fibril structure in the centre where the "finger" displaced the collagen. (ii) XZ- reconstruction showing the flow field of the scaffold. Diameter is determined by the widest slice of a reconstructed image (iii) 63x magnification showing a detailed view of the fibril structure of collagen I (d) 3D cut-out reconstruction of a 2-photon second harmonic generation image showing the collagen scaffold. One side has been cut out to demonstrate the inside of the scaffold.

structure resembling a lumen. The width of the Saffmann-Taylor finger is approximately half of the channel width and height assuming sufficient difference in viscosity, no interface tension and sufficient velocity¹⁸. However, in practice, the dimensions achieved by several groups is approximately 60-80% of the channel dimensions^{14,16}. A major benefit of VFP is that it can be easily scaled up as it only requires pipetting two fluids in a microfluidic channel. A downside of VFP to fabricate VoC systems is that the procedure to form the lumen is sensitive to many factors, such as extracellular matrix concentration and pH, timing, pressure and inlet and outlet geometries. Fabrication of VoC systems can thus be challenging and inherently variable.

Besides the method of fabrication, the biological aspect also needs to be considered. Typically, *in vitro* models incorporate primary human cells⁶. Although these cells are widely available from commercial sources or can be isolated directly from various human tissues, their supply is finite since they are not immortal. In addition, they exhibit donor-to-donor variability. This can negatively affect reproducibility and robustness of *in vitro* models. Human induced pluripotent stem cells (hiPSCs) can be used to generate vascular cells through differentiation with high reproducibility and robustness and therefore could improve cell quality and sustainability of VoC systems by allowing repeated return to the same (cryopreserved) single cell source¹⁹⁻²¹. hiPSCs are derived by reprogramming somatic cells to a pluripotent state using four transcription factors: c-myc, Sox 2, Oct4, Klf4²². hiPSCs can be differentiated to all cells of the body including vascular cells if provided with the right growth factors. We have developed methods which support differentiation of ECs from hiPSCs (hiPSC-ECs) under defined culture conditions and have shown that these cells are functional in a multiplicity of assays *in vivo* and *in vitro*^{23,24}. hiPSCs can be derived from patients with specific disease genotypes or healthy control individuals with minimally invasive tissue collection²⁵. Furthermore, hiPSCs allow generation of cell types that are typically difficult to harvest from patients, like neurons from the brain or cardiomyocytes from the heart. Using advanced genetic modification, molecular indicators and markers can be introduced for live cell imaging and analysis²⁶. Using the same techniques, isogenic healthy control hiPSC lines can be derived by genetic repair of the disease-causing mutation, minimizing differences and allowing effects of the mutation of interest to be studied independent of genetic background.

Here, we describe a robust and reproducible method to generate VoC systems using an optimized VFP protocol for dynamic flow experiments. We use hiPSC-ECs, rather than those isolated from primary tissues or blood from donors, to allow the inclusion of genetically marked cells into the device so that they can be precisely tracked. The system we describe represents an important advance in the fabrication of robust, low-cost VoC systems that will enable future dynamic studies in disease modelling and drug development.

2.2 Results

To optimise the VFP-technique, straight flow channels with fixed dimensions of 500 μm \times 500 μm \times 1 cm ($w \times h \times l$, Figure 1ai)) were designed to facilitate lumen formation. Master-moulds were fabricated with SU-8 photolithography to produce flow channels that were

highly similar. Polydimethylsiloxane (PDMS) casting of the master-moulds was used to fabricate chips by conventional soft lithography. Analysis of the PDMS cast showed that, on average, channels had a width of $496 \pm 3.7 \mu\text{m}$ and height of $527 \pm 1.2 \mu\text{m}$, an aspect ratio of 1.06 (data not shown).

First, lumens were patterned as described by Bischel et al. with a minor modification (protocol 1: passive pumping (PP), Figure S1)¹⁴. This method relies on medium flow driven by the differential surface tension of a small droplet placed on the inlet and a large droplet on the outlet of the microfluidic channel. When the droplet on the outlet is sufficiently large, the force generated by passive pumping can be calculated using the following equation [2]²⁷

$$\Delta P = \frac{2\gamma}{r} \quad (2)$$

(where P: pressure [Pa], γ : surface tension [N/m], r: radius curvature of droplet [m])

This shows that a smaller initial droplet (i.e. higher curvature) generates more force. This curvature depends on the dimensions of the inlet, volume of the applied droplet and hydrophobicity of the surface. Patterned collagen I was imaged using two-photon second harmonic generation (2P-SHG, Figure 1c,d) and the diameter was analysed. The diameter was defined as the widest part of the reconstructed flow area (Figure 1cii). In our hands, the protocol had a success rate (defined as generation of a perfusable lumen with the diameter $<400 \mu\text{m}$) of 90-100% depending on the operator. When comparing lumen diameter in the middle section of the flow channel, we observed that the average lumen diameter was $261 \pm 28 \mu\text{m}$, which is similar to that reported by others previously with comparable flow channel dimensions (cf $256 \pm 21 \mu\text{m}$)¹⁵. However, the analysis showed a significant entry effect so that these lumens gradually decreased in diameter over the length of the channel (Figure 2ai and 2b, blue line). Diameter analysis showed high inter-lumen variation, with diameters ranging from 220-320 μm (Fig 2d and Figure S3). We further observed additional variation when this protocol was performed by different operators. Interestingly, we observed that the lumen diameter was typically the smallest at around 5-7 mm from the inlet (Figure 2b).

We next patterned lumens by applying a modified protocol described by Herland et al.¹⁶; which relies on hydrostatic pressure on the chip inlets to drive lumen formation. As reported previously and from our experience, air-

bubbles were the major cause of failure with this protocol (data not shown). We therefore modified the protocol by introducing an additional step that included inserting an empty pipette tip prior to injecting the collagen (protocol 2: gravity driven (GD), Figure S1b). This allowed addition of PBS to the top of the collagen without introducing air bubbles. Lumens were imaged with 2p-SHG and the diameters measured (Figure 2aⁱⁱ and 2b, orange line and Figure S4). Interestingly, the lumens patterned following this adaption showed a uniform diameter at the beginning of the channel, with gradual widening of the lumen at the end (Figure 2aⁱⁱ and 2b, orange line). The GD protocol had a high success rate (defined as perfusable lumen with a diameter <400 μm) and improved intra-lumen diameter profile (Figure 2c); however, with the parameters used, this protocol was sensitive to small deviations in the volume and the height resulting in relatively high inter-lumen variation (Figure 2d). We also noticed that the GD protocol failed with some batches of collagen possibly due to batch-to-batch differences. To successfully initiate patterning with these collagen batches, more pressure was required (i.e. more driver fluid) which resulted in a widening of the lumen like that reported by Herland et al.

In order to generate uniform lumens with more pressure and less volume, we combined the protocols for passive pumping and extension of the pathway. To consistently extend the pathway, pipette tips were cut using a customized mould that resulted in uniform end lengths of 7 mm (protocol 3: extended passive pumping (EPP), Figure S1a). Lumens were imaged with 2P-SHG and the diameter measured (Figure 2aⁱⁱⁱ and 2b, grey line and Figure S4). Diameters typically showed a small oscillating trend around the average diameter across the average width of $255 \pm 12 \mu\text{m}$ (Figure 2d, Figure S4). Levene's statistical test showed non-equal variance ($p=0.007$), confirming smaller variance in diameter of lumens patterned using the EPP protocol (protocol 3) than the lumens patterned using the PP or GD protocols (protocol 1 and protocol 2 respectively). length of the channel. All lumens ($n=10$) had similar diameters with an As expected, one-way ANOVA analysis indicated no differences between the means ($p=0.654$). In higher throughput

of 3D vessels generated using the optimized EPP protocol. The flow profile was determined by the assessment of the velocity of the fluorescent beads that were perfused at a specific flow rate (20 $\mu\text{l}/\text{min}$).

Distances travelled by individual beads were manually measured at the specific segments of the channel to reconstitute the flow profile (Figure 5a,b). Shear stress was calculated from maximum velocity and diameter at the specific segments of the channel (Figure 5c, $N=1$). The cultured lumen was segmented into three Regions of Interest (ROI 1-3) and the average diameter was determined. ROI (ROI 1:320 μm , ROI2:290 μm ROI3: 300 μm) Flow profile analyses showed that on average the flow rates are comparable with

each other and the set flow rate (ROI 1: $18.8 \pm 1.3 \mu\text{l/min}$, ROI 2: $17.8 \pm 1.5 \mu\text{l/min}$, ROI 3: $18.0 \pm 0.6 \mu\text{l/min}$ (cf set flowrate: $20 \mu\text{l/min}$). The corresponding shear stress was calculated using equation 1. This analysis showed that, on average, shear stress was 0.27 Pa with a maximum of 13 % deviation within the ROIs thus validating the channels as being capable of producing equal sheer stresses along their length.

2.3 Discussion

To generate robust *in vitro* 3D vascular models, it is essential to balance bioengineering with cell biology; cell survival and functionality must be compatible with scaffold design. An important feature for high-utility technology is that it yields technical replicates regardless of operator. Currently, 3D vessels are fabricated by encapsulating and removing a small-diameter needle or PDMS rods in an extracellular matrix^{12,29–32}. Although this method is straightforward and reproducible, it is laborious and difficult to scale up. To address this, we investigated the VFP the described by Beebe et al and showed it to be easily implementable and scalable but we observed gradual narrowing of the patterned lumen along its length. This change in lumen shape is a challenge in the context of dynamic studies since the ECs are subject to significantly different shear stresses when exposed to flow (up to 3-fold in a single channel). Shear stress has a pivotal role in cell fate and behaviour and intra-lumen variation would reduce the uniformity of results *a priori* in a single channel and require elaborate downstream analyses to interpret results. Diameter variation should therefore be kept to a minimum^{10,33}. In this study we showed that by modifying the existing protocol by extending the entry length, we could rapidly generate reproducible 3D vascular structures with reduced variance without increasing difficulties in the technical preparation or requiring specialized equipment. The method proved to be scalable and typically 24 channels could be patterned by one person within 10 minutes. The protocol is low cost and can be easily implemented in a non-specialist biology lab. We further showed that these 3D vascular structures could support the culture of either hiPSC-ECs or cocultures of hiPSC-ECs and primary mural cells (HBVPs).

To generate circular lumens, we designed flow channels with a square cross-section. However, since manufacturing variability can be expected, dimensions were verified by analysing the cross-section of a PDMS cast. This showed that the resulting flow channel has a width approximately as designed ($500 \text{ cf } 496 \mu\text{m}$). However, the height appeared to be consistently $529 \mu\text{m}$, giving an aspect ratio (AR) of 1.06. It was therefore expected that the patterned lumens would also have an AR of 1.06.

In confocal microscopy, it is essential to use an immersion medium that exactly matches the refractive index of the sample to minimize differences in z-reconstruction³⁴. The refraction index of a collagen I hydrogel has been

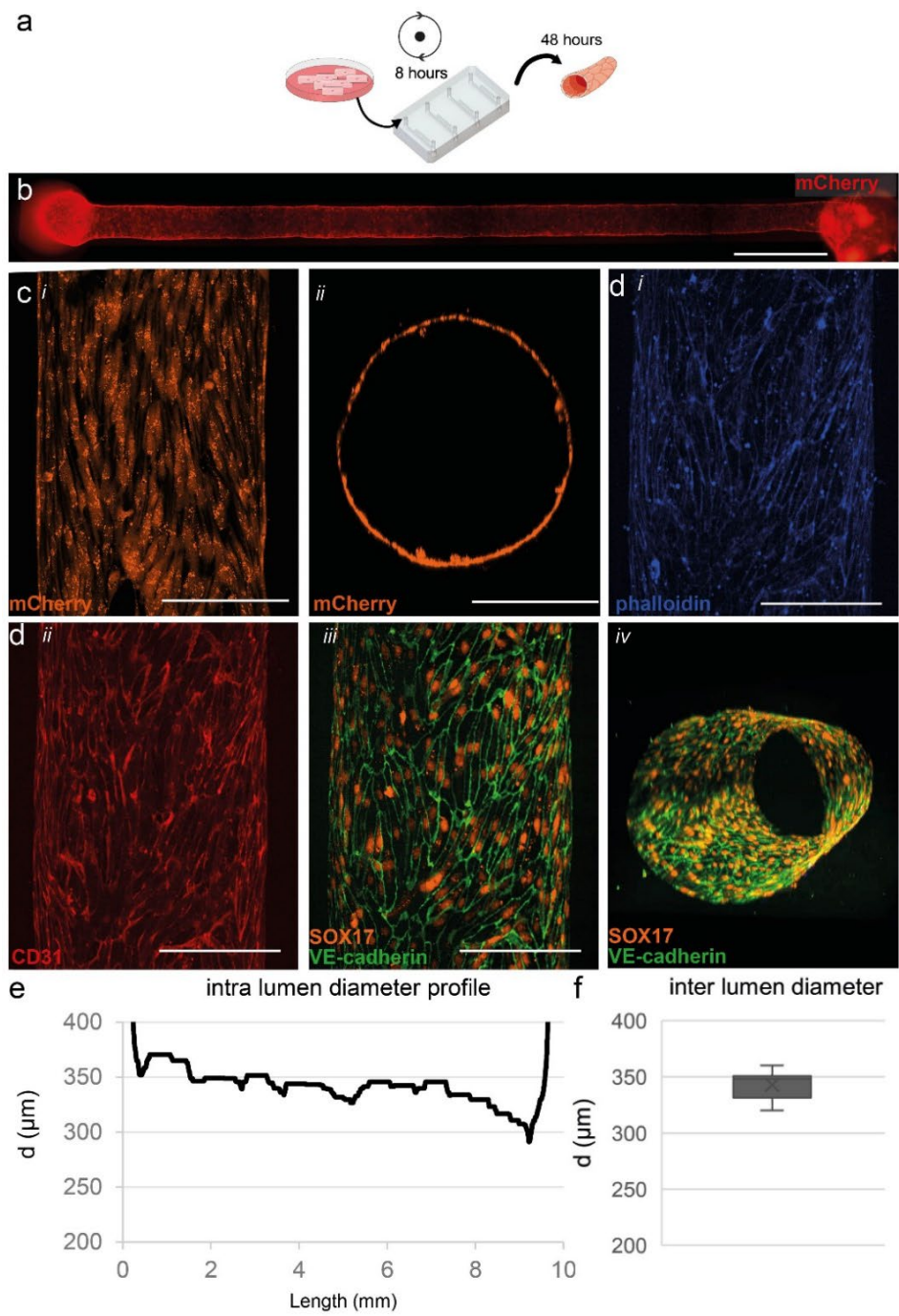
reported to be 1.336, close to that of water (1.333)³⁵. However, depending on structure, concentration, and hydration this value variable, ranging from 1.3-1.5^{36,37}.

To investigate how this effect influences our diameter analyses, we imaged one lumen with three different immersion media. We observed that although the height was significantly affected by this refraction index mismatch, the width was not (Figure S6). Therefore, the diameter can be estimated by measuring the maximum width of a reconstructed lumen regardless of immersion medium or dry objectives. Dry objectives have major benefits in that they have typically longer working distance ranges and are able to switch to multiple fields during image acquisition, improving the throughput of confocal analyses.

As reported by Bischel et al., the diameter of the patterned lumen depends on the viscosity of the collagen, the velocity of patterning, and the dimensions of the microfluidic channel. The viscosity of collagen is highly dependent on its concentration³⁸. Therefore, mixing a homogenous collagen solution is crucial for reproducibility between experiments. The stock solution of highly concentrated rat-tail collagen is extremely viscous and adhesive to standard pipette-tips and deviations were observed between different mixing batches. To optimize reproducibility between experiments, we found it best that the quantity of collagen be verified by weight and then diluted accordingly.

Furthermore, we observed during the throughput optimisation step that when many lumens were patterned from a single mixing batch, those last showed inconsistent lumen shapes. For this reason, we rigorously mixed the collagen, prepared it in small batches and used it immediately for optimal reproducibility. We observed that most lumens generated using protocol 1 tended to have a minimum diameter 5-7 mm from the inlet of the channel. By contrast, we observed a stable diameter at the beginning of the lumens patterned with protocol 2 and propose that extension of the pathway prior to the microfluidic channel could improve lumen diameter profile.

To extend the pathway, we inserted 7 mm cut pipette tips in the outlet prior patterning for three reasons. First, this prevents the narrowing of the patterned lumen near the inlet. By removing both pipette tips whilst twisting, the inlet and outlets are collagen-free allowing easy connection to a microfluidic flow system. Second, the shape of the driving droplet is not dependent on the hydrophobicity of the PDMS. The hydrophobicity of the microfluidic device changes after plasma treatment and surface functionalization and post-treatment, in a time-dependent manner and this introduces an extra variable³⁹. By using an untreated, defined material, this hydrophobicity is constant and results in a constant driving force. Finally, patterning is less dependent on manufacturing errors like damaged or bent inlets by punching or casting variability. To cut these tips with a consistent



length, we made a custom cutting guide. Using 3 mm and 5 mm extensions, we observed a distinct entry effect with a constriction at the inlet of the channel. Using the 7 mm extension this entry effect was reduced or vague.

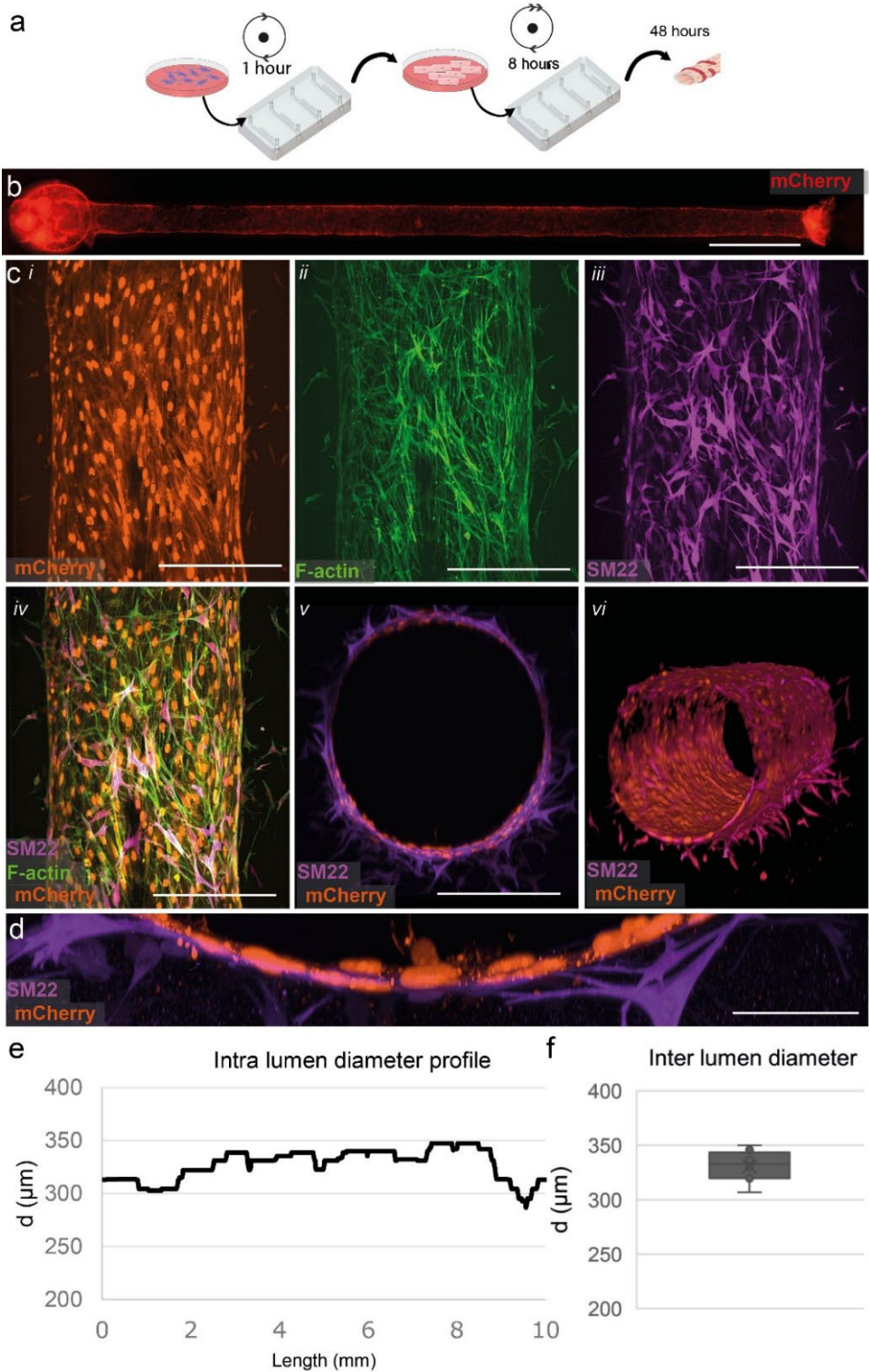
It is important to use only straight cut tips of consistent length as an entry effect can be observed when tips are too short. To optimize the total length, we tested different tip lengths using the same diameter. Further extension could remove this entry effect completely, however required more collagen. Therefore, designated 7 mm as optimum. The patterned lumens are elastic and are significantly deformed by cell seeding during injection; however, we observed that this deformation is uniform and reproducible when similar pressures were applied during cell seeding experiments, the overall success was 88/96 (92%) of all attempts, defined as perfusable lumen with diameters $<400\text{ }\mu\text{m}$. while reducing the total length. These shortened tips were inserted such that their total height was respectively 3 mm, 5 mm and 7 mm from the coverslip. With the 3- and 5-mm extension, we observed an entry effect with a sudden decrease in diameter followed by a consistent diameter, similar to what was observed in the PP-protocol. With the 7 mm extension this effect was not observed or was less distinct (Figure S5).

The reason for failure was introduction of air bubbles that prevented patterning. To further optimize this protocol, we tested different path lengths to reduce total collagen volume. By first cutting a pipette tip at 7 mm and then shortening this small tip to 2 to 3 mm we kept the inlet diameter similar

In parallel, next to the patterning protocol, we also optimized cell seeding into the scaffolds. hiPSCs were genetically engineered to express the fluorescent protein mCherry ubiquitously and differentiated to ECs as described previously^{23,24,28}. This allowed live cell imaging in 3D in real time. We tested various seeding densities (data not shown) and found that 1×10^7 cells/ml was optimal for complete- and uniform channel coverage and high cell viability.

The microfluidic devices were slowly rotated for 8 hours to allow even cell attachment around the complete lumen (Figure 3a). After 48 hours, live cells

Figure 3: Three-dimensional cell culture of hiPSC-ECs. (a) Schematic overview of cell seeding procedure and culture in microfluidic devices. hiPSC-ECs were seeded and cultured for 48 hours in static conditions. (b) Widefield image shows an even and consistent mCherry signal demonstrating uniform coverage of hiPSC-ECs along the whole lumen in a collagen scaffold. (c) (i) Top-down view of live cell confocal image (ii) XY-reconstruction of the live cell confocal microscopy confirms complete coverage around the perimeter of the lumen (d) Top-down reconstruction of the lumen visualised using the following markers (i) F-actin (phalloidin, visualised in blue) (ii) CD31 (visualised in red) and (iii) VE-Cadherin (visualised in green) at the periphery of the hiPSC-ECs co-stained with SOX17 (visualised in orange) localised at the nuclei of endothelial cells showing alignment with the longitudinal axis of the lumen (iv) 3D reconstruction of the engineered vessel showing VE-cadherin and SOX17 around the complete periphery of the lumen and a more detailed reconstruction is presented in videoS1 (e) Analyses of the full-length channel shows a uniform diameter with small tapering near the outlet (f) Diameter analysis of cellularized lumens ($n=8$), on average $343 \pm 12\text{ }\mu\text{m}$. Scale bars, b: $1000\text{ }\mu\text{m}$, c, d: $200\text{ }\mu\text{m}$



were imaged using an EVOS fluorescence microscope (Figure 3b). Even distribution of fluorescence from the mCherry expressing ECs was observed across the entire length of each channel. Further analyses using confocal fluorescence microscopy confirmed even coverage around the perimeter of the lumen (Figure 3*ci* and *cii*). Analysis of the vessel diameter ($n=8$) showed an average width of $343 \pm 12 \mu\text{m}$ (Figure 3f). The diameter profile was essentially uniform but was on average significantly wider than bare collagen lumens. VoCs were fixed and immunostained for the endothelial-specific markers CD31, SOX17 and VE-cadherin (Figure 3d). VE-cadherin was observed at the cell-cell junctions of the ECs, demonstrating uniform EC interaction and monolayer formation (Figure 3*diii*).

To further recapitulate the architecture of *in vivo* vasculature, we generated 3D vessels with supporting mural cells (Figure 4). First, we seeded primary human brain vascular pericytes (HBVPs) into the lumen scaffold and rotated for 1 hour (Figure 4a). Next, hiPSC-ECs were seeded as described before and cultured for 48 hours. Uniform coverage by hiPSC-ECs was observed across the entire length of the scaffold similar to the monoculture (Figure 4b). HBVPs were also found evenly distributed across the microfluidic channel. This was evident in immunofluorescence images taken using spinning disk confocal microscopy which showed a uniform endothelial cell layer with adjacent mural cells, as visualized by mCherry (hiPSC-ECs), F-actin (hiPSC-ECs and HBVPs) and SM22 (mural cell-specific marker to label HBVPs) (Figure 4*ci-vi*, Supplementary Video). Notably, close interaction was observed between the HBVPs and hiPSC-ECs (Figure 4d). Importantly, measurement of the diameter of these vessels in the cocultures was comparable to that in the monocultures $331 \pm 13 \mu\text{m}$ ($n=8$, non-significant p value = 0.18, Figure 4f). Typically, the diameter profile of the co-cultures shows a similar uniform expansion. To further explore the applicability of the technology in functional studies, such as a shear-stress analysis and modelling endothelial-leukocyte interaction under flow, we determined the flow profile across the entire length of the channel. It is important to point out that introduction of air bubbles severely deform the patterned lumens and must be avoided. This stable diameter ensured more

Figure 4: Three-dimensional coculture of hiPSC-ECs and HBVPs. (a) Schematic overview of the protocol for cell seeding and culture in microfluidic devices. (b) Widefield image shows an even and consistent mCherry signal demonstrating uniform coverage of hiPSC-ECs along the whole lumen in collagen gel, similar to that of the monoculture (c) Top-down view of immunofluorescent staining showing close interaction of EC and pericytes (i) mCherry expressing ECs (visualized in orange) (ii) F-actin (visualized in green) (iii) SM22 staining HBVPs (visualized in magenta) and (iv) merged image of EC- and SMC- markers. (v) XZ-view demonstrating lumen lined with mCherry labelled ECs (orange) surrounded by HBVPs (magenta). (vi) 3D reconstruction of the vascular tube, a complete reconstruction is presented in video S2. (d) High magnification of cross section, demonstrating close interaction between the inner EC-layer and surrounding HBVP supporting cells. (e) Diameter analyses of a full-length channel show uniform channel similar to monoculture. (f) Diameter analysis of the cellularized channel, on average $331 \pm 13 \mu\text{m}$ ($n=8$). Scalebars, b: $1000 \mu\text{m}$, c: $200 \mu\text{m}$, d: $50 \mu\text{m}$.

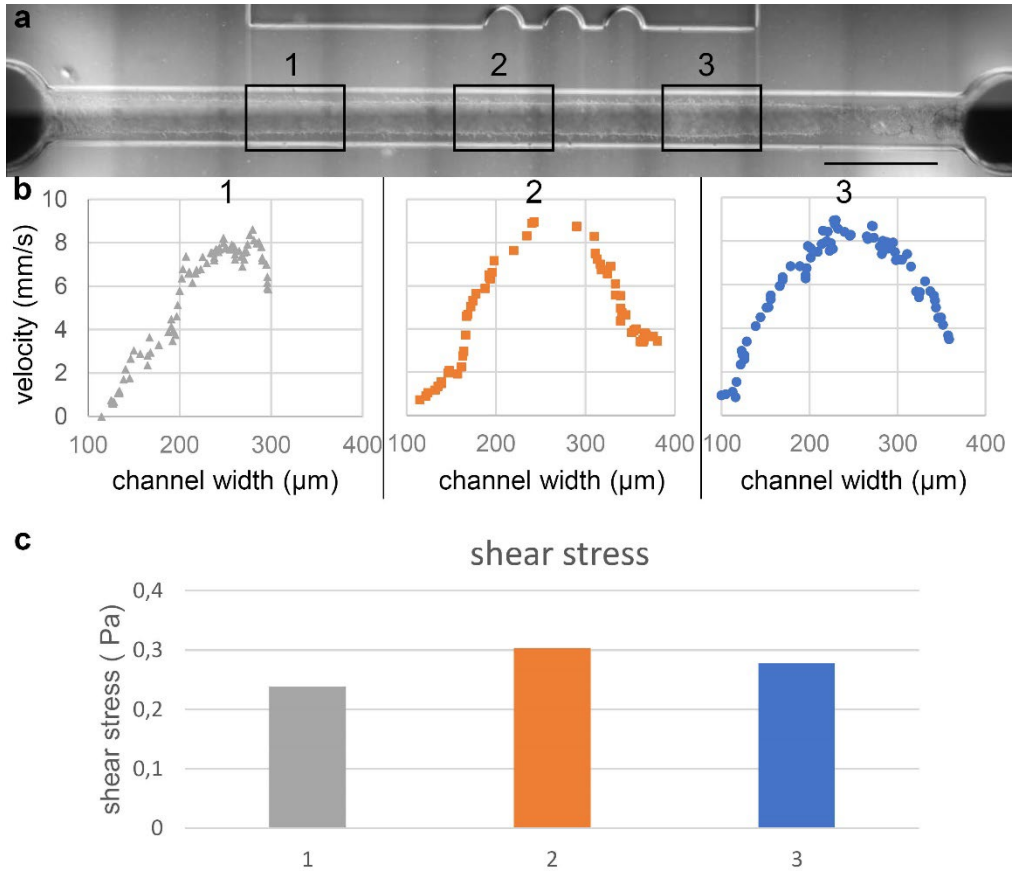


Figure 5: Analysis of the flow profile. (a) Widefield image of the perfused lumen. Boxes are showing the pre-determined regions of interest (ROI) at 2.5 mm, 5 mm and 7.5 mm from the inlet. The average diameter of ROI 1; 320 μm , ROI 2: 290 μm , ROI 3, 300 μm . A full impression of the perfused lumen is presented in video S3. **(b)** Velocity profile reconstructed of 30 frames per ROI showing maximum velocity in the centre of the lumen. Some interaction of the beads with the cell wall can be observed. Using maximum velocity and assuming laminar flow the volumetric flow rate is determined to be respectively 19 $\mu\text{m}/\text{min}$, 18 $\mu\text{m}/\text{min}$, 18 $\mu\text{m}/\text{min}$. **(c)** Calculated shear stress per ROI using the determined flow rates and measure diameters. ROI 1 0.24 Pa, ROI 2: 0.30 Pa and ROI 0.28 Pa.

uniform physiological conditions for cells seeded in the lumen, as evidenced by particle image velocimetry, allowing more accurate dynamic experiments to be performed. ~ 0.3 Pa is a physiologically low shear stress; however, with our current system, higher velocities could not be measured as the individual particles were not detected in two successive frames.

2.4 Conclusion and Future outlook

Lumens patterned using our protocol with standardized parameters resulted in high reproducibility in the fabrication of VoC systems without specialized structures consisting of hiPSCs-derived vascular cells. Furthermore, these vascular models were perfusable with minimal variation in shear stress. This

will eventually allow isogenic cells to be cultured as 3D vessels *in vitro* that recapitulate *in vivo* architecture. Combination of vascular and inflammatory cell types differentiated from hiPSCs may help to determine which cellular component of the vessel wall is affected by (genetic) disease and cause the disease phenotype. This platform was demonstrated to be fully compatible with various microscopes in conventional biological workflow. While we used straight channels here, the protocol is easily adapted to curved channels with similar results (Figure S7). This can be relevant for some pathologies that equipment. It also proved to be rapidly scalable and applicable to vascular result in different fluid mechanical conditions, such as atherosclerotic plaques in blood vessels, and could be modelled with this adaptable protocol.

2.5 Acknowledgments

Dr. Konstantinos Anastassiadis of the TU Dresden for kindly providing the following constructs: pPB-CAG-mCherry and pCMV-hyPBASE. The authors acknowledge the funding received from the Dutch Science Foundation (NWO) under the Gravitation Grant 'NOCI' Program (Grant no. 024.003.001) and this project has received funding from the European Union's Horizon 2020 research and innovation program under the Marie Skłodowska Curie grant agreement No. 707404.

2.6 Materials and Methods

Generation of mCherry expressing hiPSC line

NCRM-1 hiPSC line was obtained from RUDCR Infinite Biologicals at Rutgers University (originally generated by NIH Center for Regenerative Medicine (NIH CRM)), additional information available in public database: <https://hpscereg.eu/cell-line/CRMi003-A>. Ethics approval is not required. The NCRM-1 line is a male control reference line obtained from CD34+ cord blood cells and is reprogrammed with an episomal plasmid. The cell line was modified in-house with a mCherry expression cassette under a CMV early enhancer/chicken β actin (CAG) promoter using a previously established protocol⁴⁰.

Differentiation hiPSC-ECs

hiPSC-ECs were differentiated using a previous protocol with minor modifications^{23,28}. Briefly, hiPSCs were maintained in TeSR™-E8™ medium on vitronectin-coated 6-well plates and seeded at day-1. Twenty-four hours after seeding E8 medium was replaced with B(P)EL medium supplemented with 8 μ M CHIR. On the day -1, the medium was replaced with B(P)EL medium supplemented with 50 ng/ml VEGF (R&D systems) and 10 μ M SB431542 (Tocris Bioscience) and refreshed on days 7-9. hiPSC-ECs were isolated on day 10 using CD31-Dynabeads™ (Invitrogen) as previously described²⁸. hiPSC-ECs from cryo-preserved batches were used in all further experiments.

Thawing and expanding of hiPSC-ECs

hiPSC-ECs cells were thawed, resuspended in complete Endothelial cell serum-free medium (EC-SFM, Gibco, cat. no. 11111-044) and plated on a 0.1% gelatine-coated culture flask in complete EC-SFM, as previously described²⁸. Cells were used for experiments when nearly confluent by visual inspection, typically at day 4. Cells were harvested using TrypLE™ according to the manufacturer's instruction. All hiPSC-ECs were used at passage #2.

Fabrication of microfluidic devices

Master-moulds for the microfluidic devices were designed in SolidWorks (Dassault Systèmes SolidWorks Corp.) and fabricated in a cleanroom by SU-8 photolithography at the University of Twente. Dimensions of flow channels were 1 cm × 500 µm × 500 µm (l × w × h, fig 1a). To fabricate the microfluidic devices, Polydimethylsiloxane (PDMS, Sylgard 184, Dow Corning) base agent was mixed 10:1 with curing-agent and poured onto the master-mould to yield a PDMS slab with a thickness of approximately 5 mm. This thickness created a more stable platform for pipetting without deforming the channels by manual handling. The PDMS was degassed for one hour at room temperature under vacuum and cured at 75 °C for 180 minutes. After curing, the PDMS was cooled to room temperature and carefully peeled off. Inlet holes were punched with Uni-Core punch (1.2 mm, GE Healthcare) and the microfluidic chip was cut to fit the cover glass. Round cover glasses (#1.5, ø 34 mm Thermo scientific) were spin-coated with 100 µl PDMS (5 seconds 1000 RPM, 30 seconds 4000RPM, PDMS prepared as described above). The spin-coated cover glass and the prepared microfluidic devices were air plasma treated (2 minutes, 50 mA at 20 Pa) and contact bonded. To functionalize PDMS to covalently bind collagen I and support the scaffold, a 2-step process was carried out immediately after contact bonding. 5 % (v/v) (3-Aminopropyl)-triethoxysilane (APTES, Sigma-Aldrich) was prepared fresh in distilled water (Gibco®), injected in the channels and incubated for 30 minutes at RT. Channels were thoroughly rinsed with absolute ethanol and dried using a nitrogen-gas flow. Channels were subsequently injected with 10%(v/v) Glutaraldehyde (Sigma-Aldrich, in dH₂O) and incubated at RT for 30 minutes. Channels were thoroughly rinsed with absolute ethanol, dried with a nitrogen gas flow and baked at 75 °C for at least 5 hours to evaporate any residual ethanol and glutaraldehyde. It is essential to remove any residual glutaraldehyde and ethanol as this will affect cell viability.

Preparation of collagen I solution

The preparation of collagen I is an important step for reproducible lumens. High concentration rat tail collagen I (Corning) was prepared to a final concentration of 5 mg/ml on ice. Briefly, a stock solution was prepared using M199 medium 10X (Gibco®), distilled water (Gibco®) and 1M sodium hydroxide according to the manufacturer's instructions. The appropriate amount of collagen I was pipetted in an empty vial using a positive

displacement-pipette and weighed to verify quantity. The proper amount of stock solution was added to the collagen and carefully mixed. pH was adjusted with sodium hydroxide by adding until the colour of the mixture changed from yellow to pink indicating a pH of approximately 7.4. The pH of collagen I is crucial for the mechanical properties; therefore care must be taken to perform this step as reproducibly as possible⁴¹. The collagen I mixture was always thoroughly mixed and spun down to remove air bubbles and kept on ice. Mixed collagen was used within 10 minutes.

Patterning of lumens using Viscous Finger Patterning

A schematic representation of all methods is given in Figure S1. The protocol as published by Bischel et al. was performed with a minor adaption as presented in Figure S1 protocol 1. To be able to connect the microfluidic devices to a microfluidic pump a large outlet port was not possible. For this reason, we left a pipette tip filled with collagen behind to reduce the surface tension. The protocol published by Herland et al. was modified to improve success-rate by inserting an empty pipette tip before injecting the collagen (Figure S1 protocol 2: GD). This allows applying the PBS to induce the needed hydrostatic pressure without a manual error.

Our protocol (Figure S1 protocol 3 EPP) is as follows. A standard P10 pipette tip (Greiner Bio-One #741015) was cut at approximately 7 mm from the tip using a custom fabricated cutting guide and inserted into the outlet of the microfluidic channel. 10 μ l of collagen I mixture was injected via the inlet of the channel with a P10 pipette tip until the meniscus of the collagen I mixture reached the outlet of the microfluidic channel. The pipette tip was carefully and smoothly ejected from the pipette, keeping the meniscus at the outlet and leaving the pipette tip and the remaining collagen in the inlet. To achieve this, when attaching the pipette tip to the pipette, it is important to press only lightly to ensure a smooth release. Immediately, 3.5 μ l of PBS was carefully pipetted on top of the collagen in the small tip to initiate patterning. Patterning typically takes 15 seconds and can be confirmed by disappearing of the applied droplet and a rise in the collagen level in the opposite tip. Alternatively, PBS can be supplemented with contrasting food dye for visual confirmation of patterning. However, this affects surface tension and requires an extra washing step before cell seeding as the compounds might influence cells or (fluorescent) microscopy. Immediately after patterning lumens, were incubated for 30 minutes at 37 °C in a humid incubator. After 30 minutes, EGM-2 medium (Lonza) was pipetted in the pipette tip and channels were incubated overnight at 37 °C to allow the pH to set. Prior to cell seeding, pipette tips were removed in a smooth twisting motion. To prevent the formation of air bubbles and deformation of the patterned collagen, the cut pipette tip was first removed and inserted a new pipette tip. The medium was then added to this pipette tip and the intact pipette tip removed. A new pipette

tip was then carefully inserted. These pipette-tips aids injecting cells into the channels and act as medium reservoirs.

Three-dimensional cell-culture

Primary human brain vascular pericytes (HBVP, ScienCell) were obtained and cultured in pericyte medium (ScienCell). Cells were harvest using TrypLE™, and resuspended at a concentration of 3.3×10^6 cells/ml. 10 μ l of cell suspension was carefully injected using gel loading pipette-tips. Care was given not to introduce any air-bubbles that might deform the collagen scaffold. This was achieved by generating a small droplet in the pipette-tip before inserting. The microfluidic device was put on a rotator (0.4 RPM, channel longitudinal axis in line with rotating axis) to allow even distribution of cells for 1 hour at 37 °C. hiPSC-ECs were harvested as described above and resuspended at a concentration of 1×10^7 cells/ml. 5 μ l of cell suspension was carefully injected using gel loading pipette-tips. The microfluidic device was put on a rotator (0.4 RPM, channel longitudinal axis in line with rotating axis) and slowly rotated for 8 hours at 37 °C to ensure complete coverage of the lumen. For monocultures, only ECs were seeded. Microfluidic devices were placed in a 6-well culture plate and incubated under static conditions at 37 °C. dH₂O was added between wells to prevent evaporation. Culture Medium (EGM-2+ pen/strep) was supplemented with VEGF (50 ng/ml) and refreshed every 24 hours.

Two-photon second harmonic generation

Unstained Collagen I was imaged using two-photon second harmonic generation (2P-SHG) with a Leica SP5 confocal microscope and a multi-photon laser tuned at 810 nm. Emitted light was detected with a BG38 band-pass filter (CWL 470) before the detector.

Flow profile analysis

Microfluidic channels were placed on a microscope and connected to a 1 ml syringe pump (Cole Palmer) using 45° 20g blunt needles. Culture medium was supplemented with 5 μ m fluorescent beads and the flow rate was set to 20 μ l/min. The flow was allowed to settle for 1 minute after which 30 frames per location were recorded at a pre-determined location (2.5 mm, 5 mm, 7.5 mm of the channel) at a frame rate of 30 frames per second. All frames were combined per location to reconstitute the flow profile and the maximum velocity was determined. The average diameter of the location was determined using a widefield image and the local shear stress was calculated using equation 1 using the calculated values assuming the viscosity of 37C medium reported as 0.0008⁸.

Live cell imaging

Wide-field microscopy was performed using EVOS FL auto 2 microscope with a 4× (NA 0.4) air objective. Live cell confocal microscopy was performed using

a Leica SP5 inverted microscope using mCherry excitation/emission settings and a 20×(NA 0.75) water immersion objective.

Immunofluorescence staining

Cells were fixed by injecting 4 % PFA solution in the channels and incubated for 15 minutes at RT. Cells were subsequently permeabilised using 0.1 % (v/v) Triton-X 100 in PBS(-) for 10 minutes at RT. Channels were blocked with 1 % BSA in PBS(-) (w/w) for 30 minutes at RT. Primary antibodies were diluted (1:200) and injected into the channels and incubated overnight at 4 °C. Samples were rinsed three times with PBS(-). Secondary antibodies were diluted (1:300) in 1 % BSA and injected into the channels. Channels were incubated at RT for 1 hour and washed three times with PBS(-) for 10 minutes. DAPI was used to stain cell nuclei. After washing steps, pipette-tips were filled with PBS(-) to prevent drying out and were stored in the dark at 4 °C until imaging.

Fluorescence imaging

Immuno-stained cells were imaged using a Leica SP8 microscope equipped with a Dragonfly® spinning disk (Andor) using 20× (NA 0.75) water objective or 63× oil (NA 1.4).

Image handling

Images generated with the Leica SP5 were handled using Fiji ImageJ software. Images generated with the Leica SP8 spinning disk were handled with Imaris software (Bitplane, Oxford Instruments). For a top-down view, a full Z-stack was halved. A maximum projection of the halved stack was made to visualize the top monolayer.

Diameter analyses

In Fiji ImageJ Z-stacks were resliced with 10 µm spacing to XZ-view to visualize the formed lumen. For 2p-SHG, the stack was smoothed to reduce gaps and the average intensity and standard deviation inside the lumen were measured. A threshold value was calculated with the following equation:

$$\text{Threshold} = \text{Average mean} + 3 \times \text{Stdv} \quad (3)$$

The ImageJ magic wand-tool was programmed to trace the inner lining, and an ellipse was fitted. From the measurement, the width of the object was retrieved. Measurements under 100 µm and above 400 µm were excluded and replaced by an interpolated value. Full-length channels were plotted against the length. For inter lumen analyses, 1.5 mm around the centre of the channel was measured and the average diameter was taken as the diameter of that channel. Cell covered lumens were manually measured using an XZ-reconstruction and measured outside the mCherry signal. Results are shown as average diameter ± standard deviation.

Statistical analysis

Statistical analyses were performed with the IBM SPSS 25 software package. A Kolmogorov-Smirnoff test was performed to test for normal or uniform distribution. A test of homogeneity of variances (Levene's test) was performed to compare variances of the analysed diameters. One-way ANOVA test was performed to compare the means.

Supplementary materials

See supplementary material for a detailed overview of all viscous finger patterning protocols performed, 2P-SHG cross sections of all lumens analysed, representative diameter analyses of the pathway length optimisation and the XZ reconstruction and analyses of a lumen imaged using different immersion media. Supplementary videos of the 3d reconstruction of the monoculture and co-cultures and an example of the flow profile are also available.

References

1. Zhao, Z., Nelson, A. R., Betsholtz, C. & Zlokovic, B. V. Establishment and Dysfunction of the Blood-Brain Barrier. *Cell* **163**, 1064–1078 (2015).
2. Sweeney, M. D., Kisler, K., Montagne, A., Toga, A. W. & Zlokovic, B. V. The role of brain vasculature in neurodegenerative disorders. *Nat. Neurosci.* **21**, 1318–1331 (2018).
3. Storkebaum, E., Quaegebeur, A., Vikkula, M. & Carmeliet, P. Cerebrovascular disorders: Molecular insights and therapeutic opportunities. *Nat. Neurosci.* **14**, 1390–1397 (2011).
4. Daneman, R., Zhou, L., Kebede, A. A. & Barres, B. A. Pericytes are required for blood-brain barrier integrity during embryogenesis. *Nature* **468**, 562–566 (2010).
5. Stratman, A. N. *et al.* Interactions between mural cells and endothelial cells stabilize the developing zebrafish dorsal aorta. *Development* **144**, 115–127 (2017).
6. Sliwinska, P. N. *et al.* Consensus guidelines for the use and interpretation of angiogenesis assays. *Angiogenesis* doi:10.1007/s10456-018-9613-x
7. Simons, M. *et al.* State-of-the-art methods for evaluation of angiogenesis and tissue vascularization: A scientific statement from The American Heart Association. *Circulation Research* **116**, (2015).
8. Kim, S., Lee, H., Chung, M. & Jeon, N. L. Engineering of functional, perfusable 3D microvascular networks on a chip. *Lab Chip* **13**, 1489 (2013).
9. Baeyens, N. *et al.* Endothelial fluid shear stress sensing in vascular health and disease Find the latest version: Endothelial fluid shear stress sensing in vascular health and disease. **126**, 821–828 (2016).
10. Papaioannou, T. G. & Stefanadis, C. Vascular wall shear stress: basic principles and methods. *Hell. J. Cardiol.* **46**, 9–15 (2005).
11. Ingber, D. E. Reverse Engineering Human Pathophysiology with Organs-on-Chips. *Cell* **164**, 1105–1109 (2016).
12. José A. Jiménez-Torres, Stephen L. Peery, Kyung E. Sung, and D. J. B. LumeNEXT: A Practical Method to Pattern Luminal Structures in ECM Gels José. *Adv. Healthc. Mater.* **22**, 4311–4316 (2012).
13. Hasan, A., Paul, A., Memic, A. & Khademhosseini, A. A multilayered microfluidic blood vessel-like structure. *Biomed. Microdevices* **17**, 88 (2015).
14. Bischel, L. L., Lee, S.-H. & Beebe, D. J. A Practical Method for Patterning Lumens through ECM Hydrogels via Viscous Finger Patterning. *J lab Autom.* **17**, 96–103 (2012).
15. Lauren L. Bischel, Young, E. W. K., Mader, B. R. & Beebe, D. J. Tubeless Microfluidic Angiogenesis Assay With Three- Dimensional Endothelial-lined Microvessels. *Biomaterials* **25**, 1471–1477 (2013).
16. Herland, A. *et al.* Distinct contributions of astrocytes and pericytes to neuroinflammation identified in a 3D human blood-brain barrier on a chip. *PLoS One* **11**, 1–21 (2016).
17. P.G. Saffman & Taylor, G. I. The penetration of a fluid into a porous medium or Hele-Shaw cell containing a more viscous liquid. *Proc. Roy. Soc. A* **245**, 12–329, (1958).
18. Langaas, K. & Yeomans, J. M. Lattice Boltzmann simulation of a binary fluid with different phase viscosities and its application to fingering. *Eur. Phys. J. B* **141**, 133–141 (2000).
19. Kamm, R. D. *et al.* Perspective: The promise of multi-cellular engineered living systems. *APL Bioeng.* **2**, 040901 (2018).
20. Sinha, S. & Santoro, M. M. New models to study vascular mural cell embryonic origin: Implications in vascular diseases. *Cardiovasc. Res.* **114**, 481–491 (2018).
21. Lin, Y., Gil, C. H. & Yoder, M. C. Differentiation, evaluation, and application of human induced pluripotent stem cell-derived endothelial cells. *Arterioscler. Thromb. Vasc. Biol.* **37**, 2014–2025 (2017).
22. Takahashi, K. *et al.* Induction of Pluripotent Stem Cells from Adult Human Fibroblasts by Defined Factors. *Cell* **131**, 861–872 (2007).
23. Orlova, V. V. *et al.* Functionality of endothelial cells and pericytes from human pluripotent stem cells demonstrated in cultured vascular plexus and zebrafish xenografts. *Arterioscler. Thromb. Vasc. Biol.* **34**, 177–186 (2014).
24. Halaidych, O. V. *et al.* Inflammatory Responses and Barrier Function of Endothelial Cells Derived from Human Induced Pluripotent Stem Cells. *Stem Cell Reports* **10**, 1642–1656 (2018).
25. Raab, S., Klingenstein, M., Liebau, S. & Linta, L. A Comparative View on Human Somatic Cell Sources for iPSC Generation. *Stem Cells Int* **2014**, 768391 (2014).
26. Shinnawi, R. *et al.* Monitoring human-induced pluripotent stem cell-derived cardiomyocytes with genetically encoded calcium and voltage fluorescent reporters. *Stem Cell Reports* **5**, 582–596 (2015).
27. Walker, G. M. & Beebe, D. J. A passive pumping method for microfluidic devices. **V**, 131–134 (2002).

28. Orlova, V. V *et al.* Generation, expansion and functional analysis of endothelial cells and pericytes derived from human pluripotent stem cells. *Nat. Protoc.* **9**, 1514–1531 (2014).
29. Polacheck WJ, Kutys ML, Tefft JB, C. C. Microfabricated blood vessels for modeling the vascular transport barrier. *Nat. Protoc.* 1–32 (2019).
30. Polacheck WJ, Kutys ML, Yang J, Eyckmans J, Wu Y, Vasavada H, Hirschi KK, C. C. A non-canonical Notch complex regulates adherens junctions and vascular barrier function. *Nature* **552**, 258–262 (2017).
31. Ingram PN, Hind LE, Jiminez-Torres JA, Huttenlocher A, B. D. An Accessible Organotypic Microvessel Model Using iPSC-Derived Endothelium. *Adv Healthc. Mater* **7**, 1700497–10 (2017).
32. Wong AD, S. P. Live-cell imaging of invasion and intravasation in an artificial microvessel platform. *Cancer Res.* **74**, 4937–4945 (2014).
33. Baratchi, S. *et al.* Molecular Sensors of Blood Flow in Endothelial Cells. *Trends Mol. Med.* **23**, 850–868 (2017).
34. Besseling, T. H., Jose, J. & Blaaderen, A. Van. Methods to calibrate and scale axial distances in confocal microscopy as a function of refractive index. *J. Microsc.* **257**, 142–150 (2015).
35. Buchanan, C. F. *et al.* Three-dimensional microfluidic collagen hydrogels for investigating flow-mediated tumor-endothelial signaling and vascular organization. *Tissue Eng. Part C. Methods* **20**, 64–75 (2014).
36. Wang, X., Milner, T. E., Chang, M. C. & Nelson, J. S. Group refractive index measurement of dry and hydrated type I collagen films using optical low-coherence reflectometry. *J. Biomed. Opt.* **1**, 212–216 (1996).
37. Leonard, D. W. & Meek, K. M. Refractive indices of the collagen fibrils and extrafibrillar material of the corneal stroma. *Biophys. J.* **72**, 1382–1387 (1997).
38. Shayegan, M. & Forde, N. R. Microrheological Characterization of Collagen Systems: From Molecular Solutions to Fibrillar Gels. *PLoS One* **8**, 23–28 (2013).
39. Bodas, D. & Khan-malek, C. Hydrophilization and hydrophobic recovery of PDMS by oxygen plasma and chemical treatment — An SEM investigation. **123**, 368–373 (2007).
40. Rostovskaya, M. *et al.* Transposon-mediated BAC transgenesis in human ES cells. *Nucleic Acids Res.* **40**, (2012).
41. Raub, C. B. *et al.* Image correlation spectroscopy of multiphoton images correlates with collagen mechanical properties. *Biophys. J.* **94**, 2361–2373 (2008).

Chapter two: Supplementary Materials

Scalable microphysiological system to model three-dimensional blood

Electronic supplementary information and supplementary videos available at:

<https://aip.scitation.org/doi/10.1063/1.5090986>



Supplementary Methods

Refraction index mismatch analysis

To correctly reconstruct confocal images in 3D it is important to match the refraction index of the immersion medium with the sample. To investigate how this mismatch affects for our diameter analyses we analysed 3 different immersion media

A 3D co-culture was cultured, fixed and stained as described in methods. One lumen was subsequently imaged with a dry, water immersion and oil immersion objective (20x magnification NA 0.75, Figure S6a-c).

Pathway length optimization

Protocol 3 was modified to test different pathway lengths. Pipette tips were first cut to 7 mm as previously described. These tips were further reduced to approximately 2 to 3 mm. PDMS was cast on the master moulds 2.5 mm thick and the shortened tips were inserted in such way that the inlet was respectively 3 mm and 5 mm from the coverslip. From here all steps are described in the manuscript methods section, see "Patterning of lumens using Viscous Finger Patterning" and Figure S5.

Supplementary Figures and Table

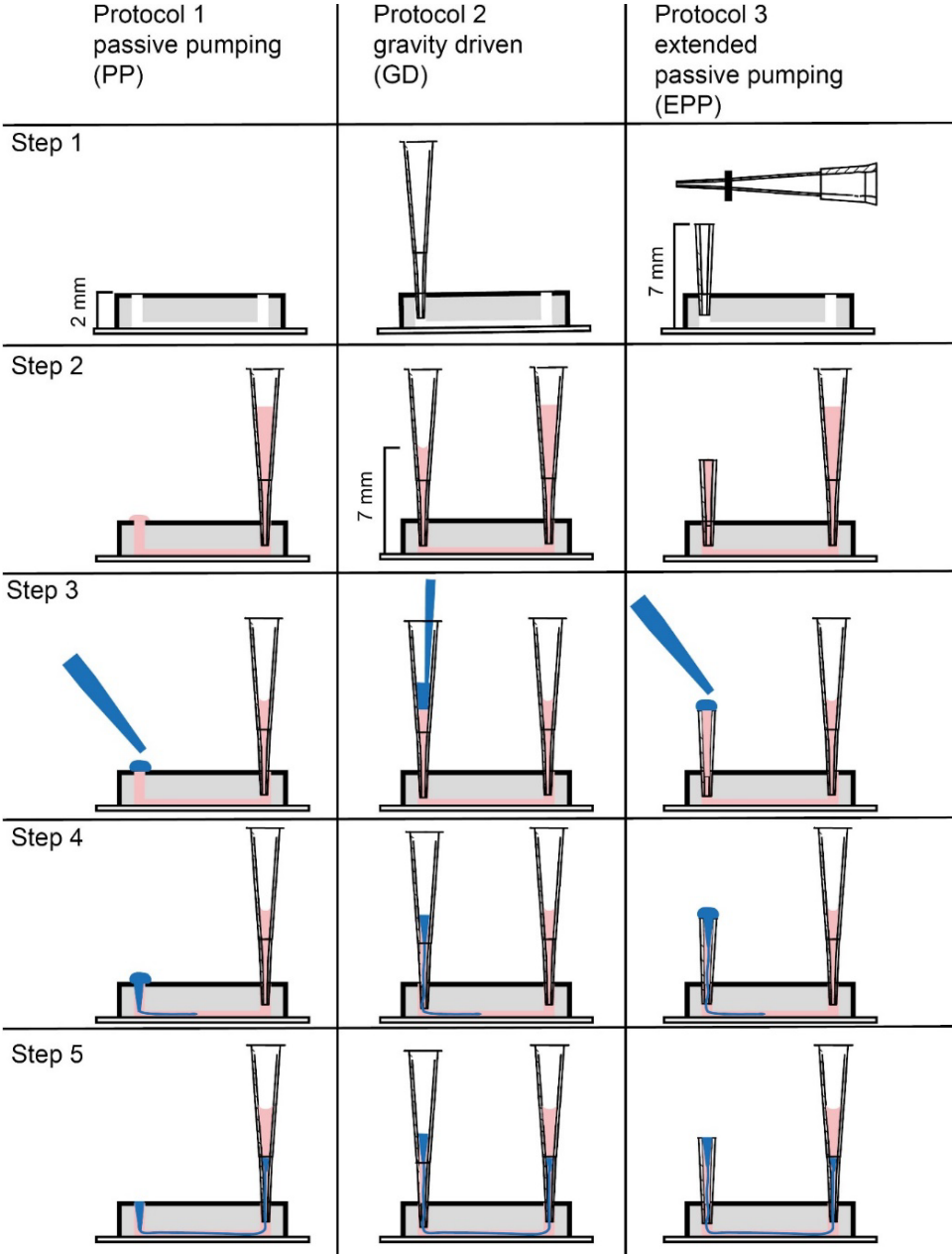


Figure S1: Schematic representation of the VFP protocols

Figure legend on next page

Protocol 1 passive pumping (PP) step 1 preparation, PDMS was cast on the master moulds 2 mm thick and inlet holes were punched with a Uni-core 1.2 mm biopsy puncher (Harris), resulting in an 800 μm inlet/outlet hole; **step 2** collagen injection, a 5 mg/ml collagen I solution was mixed as described by Bischel et al. and carefully injected into the microfluidic channel until a meniscus formed on top of the outlet, then the pipette tip was carefully ejected, leaving the pipette tip and remaining collagen behind; **step 3** initiation, 2 μl of PBS was carefully placed on top of the collagen meniscus; **step 4** viscous finger patterning starts immediately after placement of droplet; **step 5** gelation, after the finger completely traversed the channel the microfluidic device is placed in a humid incubator at 37°C to allow the collagen to gelate completely.

Protocol 2 Gravity driven (GD) step 1 preparation, PDMS was cast on the master moulds 3-5 mm thick and inlet holes were punched with a Uni-core 1.2 mm biopsy puncher (Harris), resulting in an 800 μm inlet/outlet hole. An empty Greiner Bio-One p10 pipette tip is placed in the outlet; **step 2** collagen injection, a 5 mg/ml collagen I solution was mixed as described in material and methods and carefully injected into the microfluidic channel until the meniscus reaches approximately 7 mm inside the pipette tip (first mark) on top of the outlet, then the pipette tip was carefully ejected from the pipette, leaving the pipette tip and remaining collagen behind; **step 3** initiation, 10 μl of PBS was carefully placed on top of the collagen meniscus; **step 4** viscous finger patterning starts immediately after placement of droplet; **step 5** gelation, after the finger completely traversed the channel the microfluidic device is placed in a humid incubator at 37°C to allow the collagen to gelate completely.

Protocol 3 Extended passive pumping (EPP) step 1 preparation, PDMS was cast on the master moulds 3-5 mm thick and inlet holes were punched with a Uni-core 1.2 mm biopsy puncher (Harris), resulting in an 800 μm inlet/outlet hole. A Greiner Bio-One p10 pipette-tip is cut to approximately 7 mm from the tip using a cutting guide and inserted in the outlet; **step 2** collagen injection, a 5 mg/ml collagen I solution was mixed as described in material and methods and carefully injected into the microfluidic channel until a meniscus formed on top pipette tip of the outlet, then the pipette tip was carefully ejected from the pipette, leaving the pipette tip and remaining collagen behind; **step 3** initiation, 3.5 μl of PBS was carefully placed on top of the collagen meniscus; **step 4** viscous finger patterning starts immediately after placement of droplet; **step 5** gelation, after the finger completely traversed the channel the microfluidic device is placed in a humid incubator at 37°C.

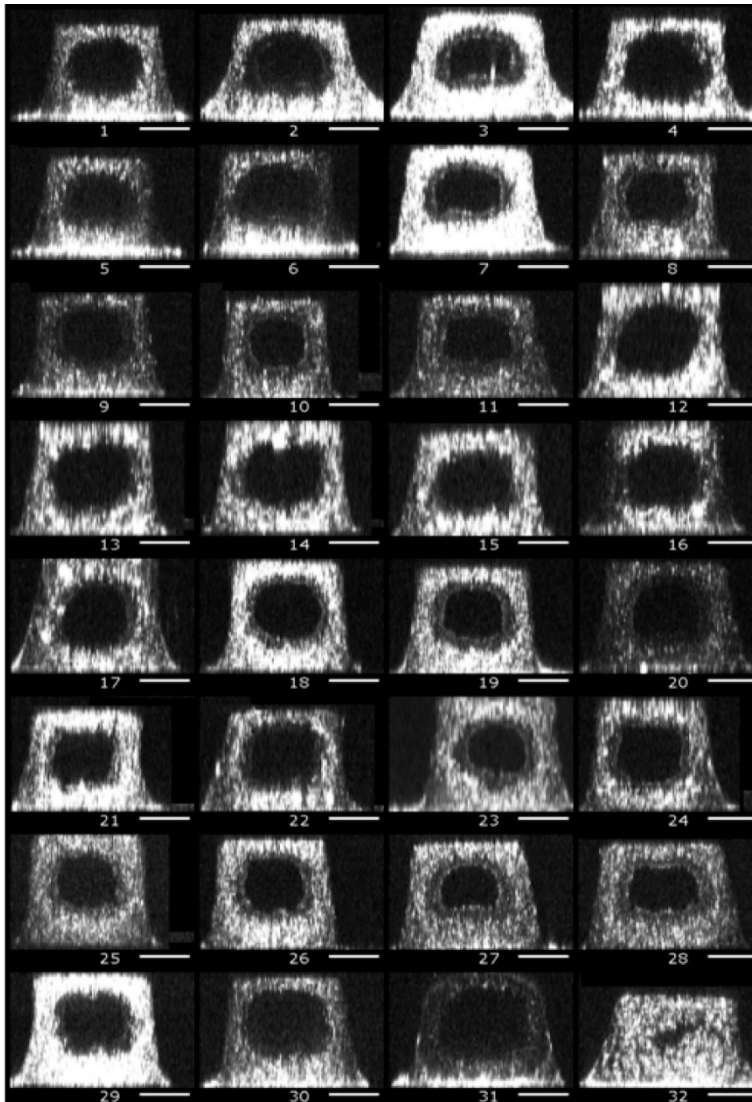


Figure S2: Cross sections of the PP lumens. A cross-sectional view of the centre of all measured lumens patterned with protocol 1. Lumens were imaged using a 10x water objective. High variation in collagen structure, lumen shape and lumen diameter can be observed. The diameter was determined by the width of a fitted ellipse. All scale bars 200 μm .

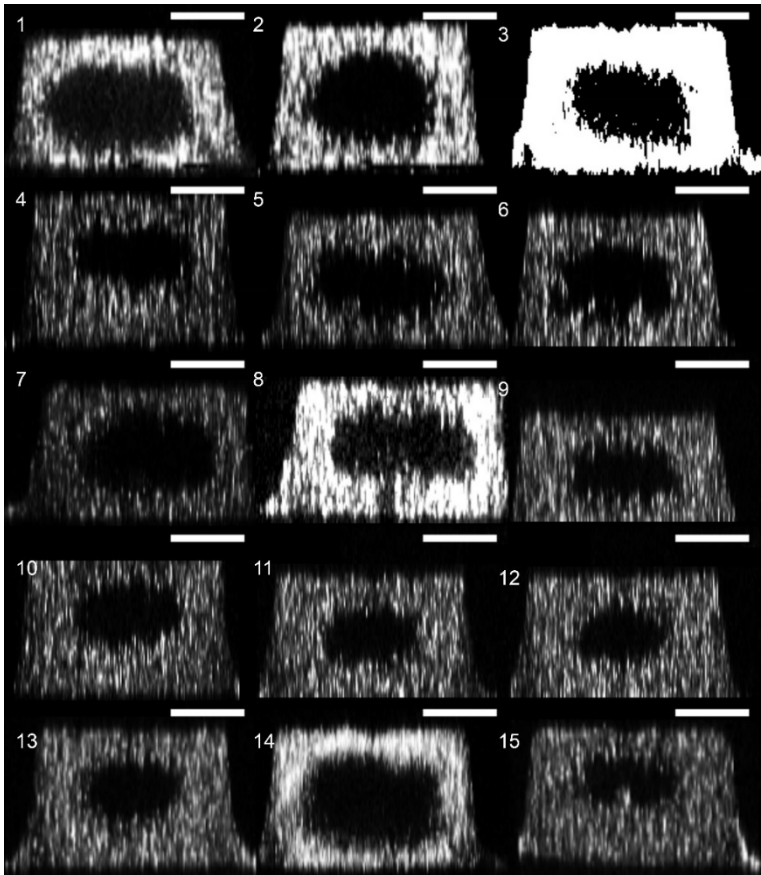


Figure S3: Cross sections of the GD lumens. A cross-sectional view of the centre of all measured lumens patterned with protocol 2. Lumens were imaged with a 10x dry objective. collagen showed more uniform structures and shape was much more consistent. Still, high variation of lumen diameter was observed. The diameter was determined by the width of a fitted ellipse. All scale bars 200 μm .

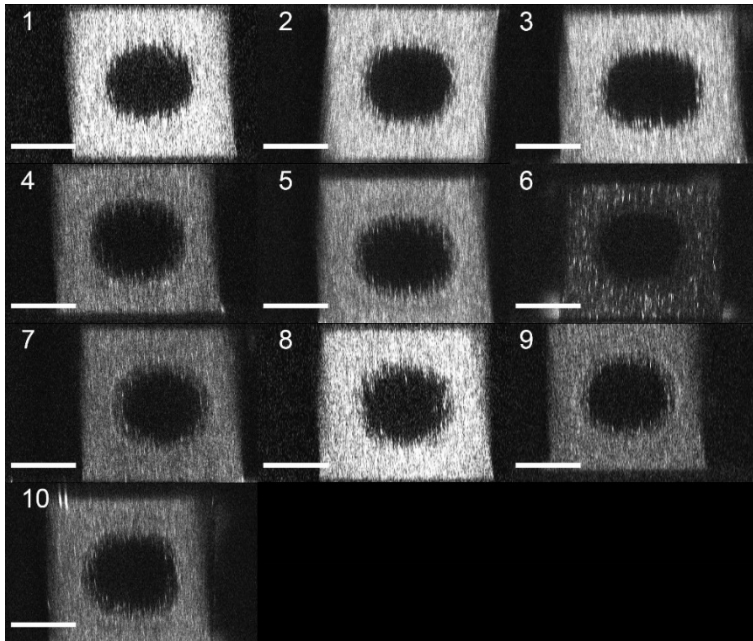


Figure S4: Cross sections of the EPP lumens. A cross-sectional view of the centre of all measured lumens patterned with protocol 3. Lumens were imaged with a 20x water objective. Lumens show much more consistent collagen structure lumen shape and diameter. The diameter was determined by the width of a fitted ellipse. All scale bars 200 μm .

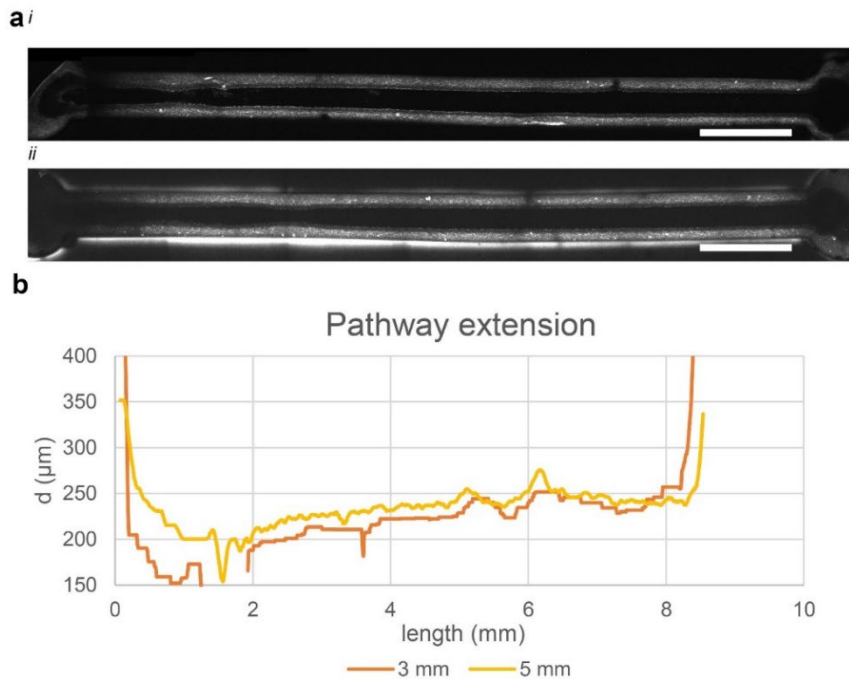


Figure S5 Path length optimization (a) A representative example of a lumen patterned with an extension of (i) 3 mm and (ii) 5 mm. (b) Diameter profile of a lumen patterned with an extension of 3 mm (orange) and 5 mm (yellow) show a significant entry effect as a sudden narrowing at the beginning of the channel.

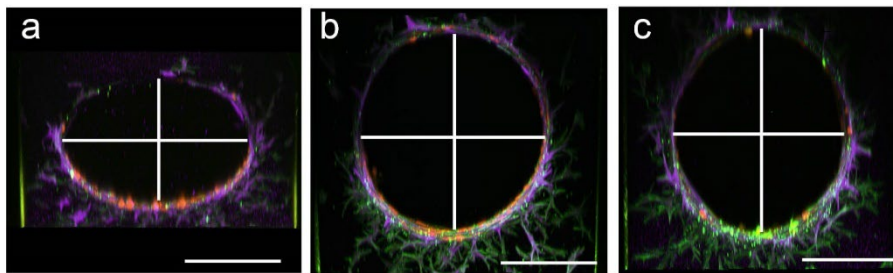


Figure S6: Analysis of the effect of refractive index mismatch. The same lumen was imaged to investigate the height with three different 20x objectives: (a) dry objective, the reconstruction resulted in an elliptical flow area with a height of 236 μm (aspect ratio W/H, (AR:0.71); (b) water objective, the reconstruction resulted in a near circular flow area with a height of approximately 355 μm (AR:1.06); (c) oil objective resulted in an oval shape with a height of 378 μm (AR:1.12). Notably, the maximum widths of the lumens were all similar and therefore can be used for consequent and consistent diameter quantification regardless of used immersion media.

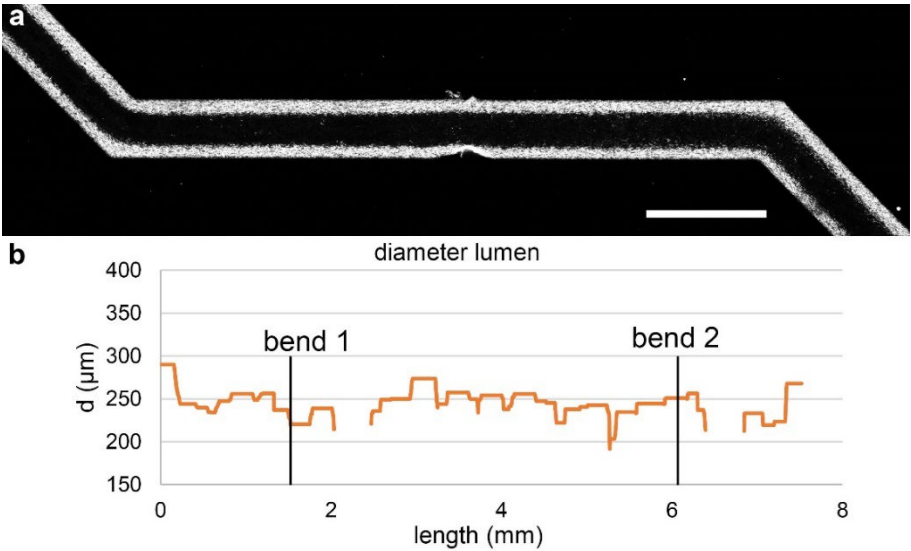


Figure S7: Example of a curved lumen.(a) 2P-SHG image of a double curved lumen in a 500 μm width channel; (b) Diameter profile of a double curved lumen showing that the lumen follows the channel with a minimal variation in diameter.

Table S1: Dimension analysis refractive index mismatch.

20x objective Immersion medium	Width (μm)	Height (μm)	Aspect ratio
Dry	343	236	0.69
Water	340	355	1.06
Oil	339	378	1.12

Chapter three:

Pressure-Driven Perfusion System to Control, Multiplex and Recirculate Cell Culture Medium for Organs-on-Chips

Mees N. S. de Graaf ¹, Aisen Vivas ^{2,3}, Andries D. van der Meer ², Christine L. Mummery ^{1,2} and Valeria V. Orlova ¹,

¹ Department of Anatomy and Embryology, Leiden University Medical Center

² Applied Stem Cell Technologies, University of Twente,

³ BIOS Lab on a Chip Group, MESA+ Institute for Nanotechnology, Technical Medical Centre, Max Planck Institute for Complex Fluid Dynamics, University of Twente

Published in Micromachines, 13(8), 1359, 2022;
<https://doi.org/10.3390/mi13081359>



Abstract:

Organ-on-chip (OoC) devices are increasingly used to mimic the tissue microenvironment of cells in intact organs. This includes microchannels to mimic, for example, fluidic flow through blood vessels. Present methods for controlling microfluidic flow in these systems rely on gravity, rocker systems or external pressure pumps. For many purposes, pressure pumps give the most consistent flow profiles, but they are not well-suited for high throughput as might be required for testing drug responses. Here, we describe a method which allows for multiplexing of microfluidic channels in OoC devices plus the accompanying custom software necessary to run the system. Moreover, we show the approach is also suitable for recirculation of culture medium, an essential cost consideration when expensive culture reagents are used and are not “spent” through uptake by the cells during transient unidirectional flow.

3.1 Introduction

Microphysiological systems or “organ-on-chip” devices (OoCs) are an emerging class of pre-clinical models intended for modelling the physiology of healthy and diseased tissue and accelerating drug discovery¹. OoCs are designed to mimic tissue microenvironments by combining different cell types in heterotypic cultures with (3D) extracellular matrix or synthetic polymer scaffolds, local chemical gradients and biomechanical stimuli that promote cellular responses in vitro to resemble those in vivo ^{2,3}. These complex cell culture devices are often intended for use with (micro)fluidic flow to mimic specific microenvironmental conditions. However, the throughput of experiments with controlled fluid perfusion in OoCs is still limited due to their technical complexity ^{4,5}.

There are several reasons that fluidic flow is needed in OoCs ⁶. First and foremost is the need for continual refreshment of the cell culture medium. Due to the small chamber and channel volumes in OoCs and often the high metabolic activity of cells under study, it is important that nutrients are replenished locally and metabolic waste products from cells are removed.

Secondly, fluidic flow can be used to introduce important mechanical stimuli. For instance, wall shear stress (WSS) is an important factor in determining how blood vessels react to stimuli in vivo and it is therefore important to include ways to measure and modulate WSS where biologically relevant ⁷.

Fluidic requirements depend on the type of OoC and the physiological condition of interest. Vessels-on-chip (VoC) generally require a large range in flow rates to induce both physiological and pathophysiological WSS depending on the model used ^{7,8}. In addition, complex cell culture medium formulations used for OoCs contain expensive components (e.g., growth factors). Recirculation of culture medium reduces the costs of experiments without compromising cell quality since culture medium supplements are in excess and are not “spent” in just one passage of the medium over the cells. Long-term perfusion would require excessive large volumes of cell culture medium. Furthermore, high medium volumes may dilute signaling molecules secreted by cells in complex culture systems to the extent that they may be beyond cellular or analytical detection.

Different methods have been used to control perfusion in OoCs ⁹. Each has its own advantages and disadvantages with varying degrees of required expertise before the technology can be implemented for OoC cell culture. When refreshing of the culture medium is the only requirement, gravity-driven flow is simple and effective. By applying a pressure head (P_{head}) to the samples, the culture medium can be replaced without the use of external pumping systems. Alternatively, by placing the OoCs on a tilting rocker platform, bidirectional flow can be induced, and thus continuous refreshment achieved, again without the need for external pumping systems ^{10,11}.

Unidirectional flow can be achieved using gravity driven flow by designing more complex fluidic circuits; however, continuous and controlled flow is not realizable using gravity alone ¹⁴. However, this approach is not suitable for all purposes as the flow rate is uncontrolled, “stop-and-go” and bidirectionality are of limited physiological relevance but can nevertheless influence the responses of the cells lining the channel ^{12,13}. When it comes to controlled unidirectional flow, syringe pumps are the first choice as these are readily available and easily set up ¹⁵. However, when used with compliant devices and flexible tubing, flow rate control in short-term experiments becomes less accurate than generally required due to long flow-settling times¹⁶. More importantly, the limited volume of syringes hinders their application in WSS experiments in long-term experiments due to the required high flow rates. Peristaltic or solenoid pumps are a better solution for long-term WSS experiments since they enable recirculation by continuously pumping fluids from and towards the same reservoir. However, the induced flow has a pulsatile character, especially at lower flow rates. This can be useful when modelling, e.g., pulsating blood vessels. Nonetheless, erratic and unintended mechanical (wall) stress can derive from such flow pattern^{9,17,18}. Furthermore, the pulsating frequency is directly coupled to the flow rate, which limits flexibility and chip design when used for OoC-models.

To increase the number of samples per fluidic pump, OoCs can be placed in series or in parallel fluidic circuits. A caveat of these setups, however, is that cell debris and clumps can occur during experiments and (depending on channel dimensions) these can block the microfluidic channels or change flow distribution. When placed in series, for example, these blocks increase the internal pressure, which may be detrimental to cells and lead to experimental failure. In parallel circuits, the cell blocks can affect the mechanical stress of other samples in the circuit: the overall flow rate remains constant, but the flow rates for all other samples increase, resulting in differences in mechanical stress in each channel.

A major limitation of the positive displacement pumps described so far is their inability to run multiple compliant samples simultaneously. These systems can only control the overall flow rate in a system and lack control of mechanical and fluidic stress exerted on the individual OoC. Due to mechanical slack and system compliance reaching steady state flow, internal pressure may take up to minutes at the OoC ^{16,19,20}. As a result, positive displacement pumps lack control of flow distribution in compliant multiplexed fluidic circuits.

To control perfusion of complex fluidic circuits containing OoCs, pressure driven pumps are a better solution as the mechanical stress and perfusion parameters can be directly controlled. In the event of microfluidic blockades, perfusion conditions of the remaining samples do not change, protecting the

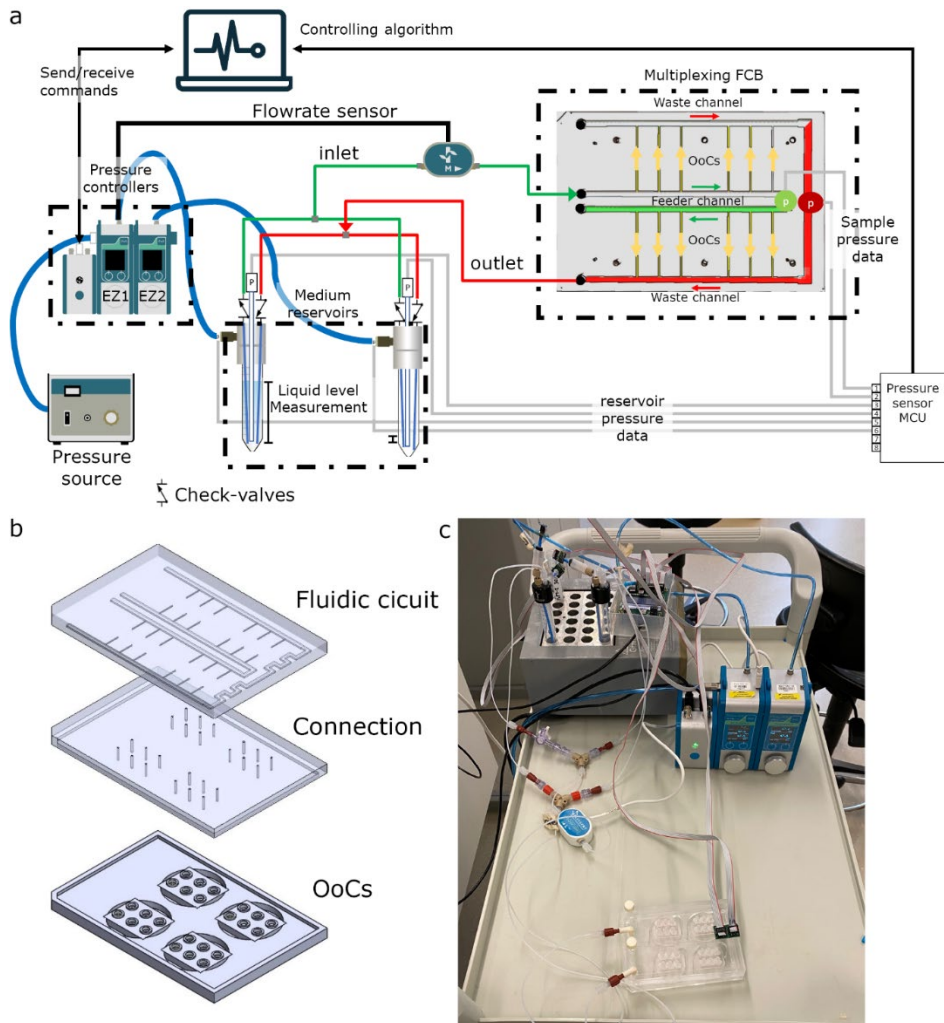


Figure 1: Overview of the perfusion system (a) Schematic of the microfluidic circuit consisting of 2 pressure controllers connected to a pressure source, additional pressure sensors (p), a passively controlled recirculation circuit and a custom-made fluidic circuit board to multiplex the perfusion to multiple samples. (b) Exploded view of the FCB shows the fluidic circuit, connection layer and 4 OoC-devices. (c) Photograph of the system tested.

remaining samples. Furthermore, compliance is better controlled as the internal pressure can be directly controlled and is not a result of all parameters being modified.

Here we developed a Python-based proportional-integral-derivative (PID) software controller able to integrate constant pressure differences into a fluidic circuit board (FCB), allowing accurate multiplexing of perfusion experiments. We demonstrate that the system can precisely control pressure

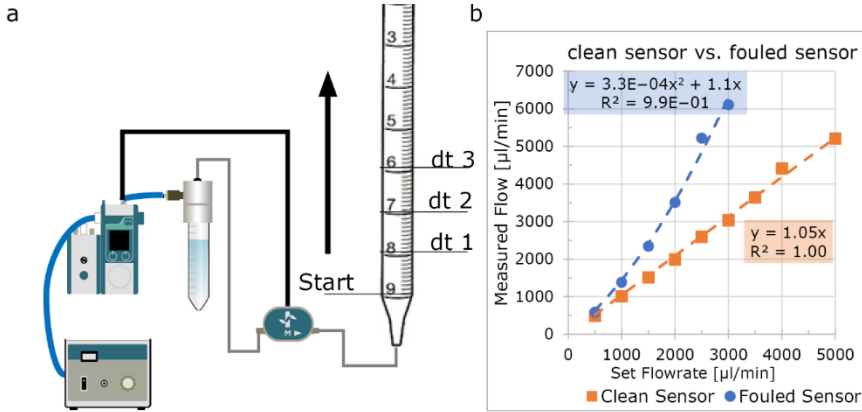


Figure 2: Validating flow rate sensor accuracy. (a) Schematic of the fluidic circuit used to validate sensor accuracy. A 10 mL serologic pipette was attached to the outlet of the circuit, and the pressure controller was set to a fixed flow rate using the internal PID-loop. At multiple intervals, time was noted and the flow rate was calculated (b) A clean sensor accurately measures the flow rate of cell culture medium (orange plot); after two days of continuous perfusion, the sensor becomes inaccurate (blue plot).

driven flow rates in various microfluidic devices and recirculate culture medium without the need for more complex systems. The perfusion system is primarily designed for 3D VoC. As it can control both the flow rate and the internal pressure precisely, it protects sensitive cell cultures. At the same time, the system is useful and can be easily implemented other OoC systems that require accurate control of the flow rate and the internal pressure.

3.2 Theoretical Model

The fluidic perfusion system was designed to apply a constant fluidic pressure difference (dP) on OoCs using a single input/output configuration (Figure 1a). The system design is composed of two pneumatic pressure controllers, a flow rate sensor and a micro-control unit (MCU) that enabled data streaming via serial communication. The pressure readouts are used to control the pressure controllers via custom-written software.

The system was able to control flow by controlling the air pressure difference of the reservoirs. The cell culture medium is then forced through the microfluidic circuit and collected in the opposite reservoir. By using the readouts from the pressure sensors, individual flow rates can be estimated using electrical circuit analogy according to Hagen–Poiseuille’s law as described by Oh et al.²¹ Hagen–Poiseuille’s law describes the volumetric flow rate for a steady-state pressure-driven fluid flow:

$$\Delta P = Q R_h \quad (1)$$

where ΔP is the required pressure difference [Pa], Q is the volumetric flow rate [$\text{m}^3 \text{s}^{-1}$] and R_h is the hydraulic resistance [$\text{Pa m}^3 \text{s}^{-1}$]

The hydraulic resistance of a microfluidic channel can be calculated with the following formulas.

For a rectangular channel:

$$R_h^{rec} \approx 12\mu \frac{L}{wh^3(1 - 0.63\frac{w}{h})} \quad (2)$$

where μ is the dynamic viscosity [Pa s], L is the channel length [m], w is the channel width [m] and h is the channel height [m]. For a circular tube:

$$R_h^{cir} = 128\mu \frac{L}{\pi d^4} \quad (3)$$

where μ is the dynamic viscosity [Pa s], L is the channel length [m] and d is the diameter [m].

Using these general equations and electrical circuit analogy, the flow distribution towards individual channels can be predicted for complex fluidic circuits using parallel and series circuits.

Total resistance for serial connected resistance:

$$R_{serie}^{total} = R_{serie}^1 + R_{serie}^2 + R_{serie}^3 + \dots + R_{serie}^n \quad (4)$$

where R_{serie} are the individual fluidic components such as tubing, flow rate-sensors, microfluidic channels and OoC.

Total resistance for parallel connected resistance:

$$R_{parallel}^{total} = \left(\frac{1}{R_{parallel}^1} + \frac{1}{R_{parallel}^2} + \dots + \frac{1}{R_{parallel}^n} \right)^{-1} \quad (5)$$

where $R_{parallel}$ are the individual branches. Flow rate of individual samples using an FCB can then be calculated using:

$$Q_n = \frac{\Delta P_{OoC}}{R_h^n} \quad (6)$$

where Q_n is the individual flow rate, R_h^n is the individual hydraulic resistances and ΔP_{OoC} is the controlled pressure difference across the samples. All calculations were performed, assuming cell culture medium containing 2% serum at 37°C with a dynamic viscosity of 0.00079 [Pa s]²².

Fluidic Circuit Board

To multiplex perfusion of the OoC devices, we used a fluidic circuit board (FCB) where multiple OoCs can be connected simultaneously (Figure 1b). Briefly, the fluidic circuit consists of a main feeder channel (Figure 1a, FCB green channel) that has individual branches towards the OoCs (yellow arrows). The fluidic flow is then collected in a central waste channel (red

channel) that directs the flow towards the opposite, medium reservoir. In the central feeder and waste channels, two pressure sensors are inserted that act as the process variable for the PID controller run by the software. The FCB used can connect up to four OoC devices, each containing three microfluidic channels (Figure 1b).

Controlled Perfusion and Recirculation

Custom PID-controller software was written in Python to maintain constant pressure difference (dP) and internal sample pressure (P_{OoC}) (Figure S1, Table S1). The software measures two pressure sensors located at the inlet and outlet and corrects the pressure commands of the pressure controllers connected to the medium reservoirs. To increase the P_{OoC} , the back pressure of the receiving reservoir can be increased. By increasing the dP between the inlet and outlet, the flow rate can be expected to change in a linear fashion (Equation (6)). The software can control two different recirculating circuits: (1) an actively controlled valve-recirculation (Figure S2a) or (2) a passively controlled microfluidic Graetz-recirculation circuit (Figure 1). The actively controlled recirculation requires the addition of two 3 port/2 position (3/2)-valves and a switchboard (Fluigent). By changing both the pressure commands and the position of these valves, the fluidic flow remains unidirectional in the OoCs²³. The Graetz-recirculation circuit is a direct analogue of an AC/DC converter used in electrical engineering and requires 4 check valves in a similar orientation (Figure 1). This allows maintenance of unidirectional flow with only switching of the pressure commands, in contrast to method 1, where the actively controlled valves need accurate synchronization of both the pressure switch and valve positions to prevent backflow and pressure surges.

3.3 Results and Discussion

Design Perfusion Platform

To overcome current limitations of OoC-perfusion, we developed a perfusion system that controls all fluidic parameters exerted on the sample. This developed system controls the perfusion rate and mechanical stress on the cells of multiple OoCs, achieves recirculation without the use of actively controlled valves and measures liquid levels to eliminate the risk of emptying medium reservoirs.

The system consists of two pressure controllers, additional pressure sensors and custom written controlling software (Figures 1 and S2). The system is designed to control multiplexing flow in using an FCB by maintaining a constant pressure difference (dP). However, the system can also be used for the perfusion of a single OoC (Figure S2b) or to multiplex the perfusion using manifold splitters (Figure S2c).

The custom-written software is a Python-based, PID controller that integrates pressure sensors placed at the OoCs to stabilize fluidic flow (Figure S1a,b).

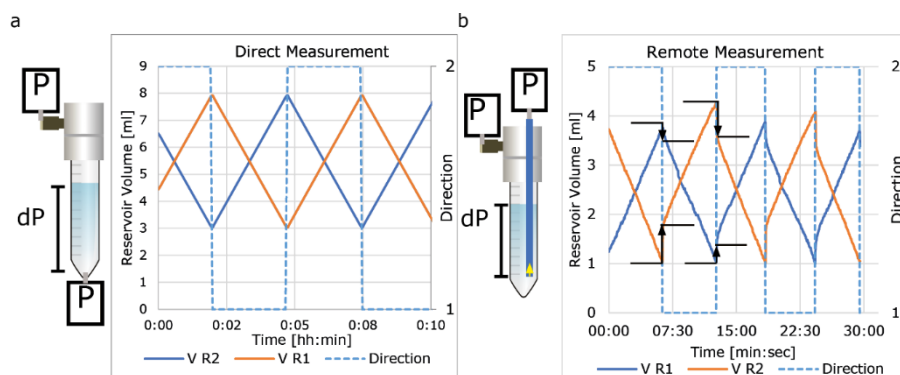


Figure 3: Measuring liquid level using pressure sensors. (a) Measurement of liquid level using direct measurement. (b) Remote measurement using tubes with 2 different diameters. Remote measurement is accurate; however, there is an offset when reservoirs are pressurized. This offset is diameter-dependent and larger with a small diameter (800 μm , orange) than with a larger diameter (3 mm, blue plot).

Furthermore, the custom software controls the recirculation by switching commands to prevent the medium reservoirs from running empty. The software registers all sensor data for post experiment analyses. After each direction switch, the software summarizes all data for that sequence and sends the data to a desired email account for online monitoring of the experiment.

Characterization of Pressure Controllers and Flow rate Sensors

To control the perfusion of the OoCs, two Flow-EZ™ (Fluigent) were used. Flow-EZ™ is a pressure controller that is used to accurately control the air pressure of a medium reservoir to drive fluids through the microfluidic circuits. These pressure controllers have two controlling modes: a constant pressure mode and a constant flow rate mode. The constant flow rate mode can be used as alternative to a positive displacement pump; however, the maximum applied pressure can be limited. The constant pressure mode can be used to apply a constant force. Both modes use an internal PID controller to transmit the process variable from either the internal pressure sensor or an external flow rate sensor integrated in the fluidic circuit.

The Fluigent-compatible flow rate sensor is thermal mass-based and commonly used for high accuracy lab-on-a-chip purposes. These sensors apply and measure a temperature gradient to calculate the mass flow. To investigate the suitability of these sensors for OoCs in long-term experiments, we examined the accuracy of a clean sensor using cell culture medium and re-measured the same sensor 2 days after continuous perfusion (Figure 2). This showed that for short-term experiments, this sensor is accurate in measuring flow rates in cell culture medium (EGM-2) but that its accuracy is highly sensitive to fouling by culture medium when used over longer periods. When a flow rate sensor becomes fouled, it significantly underestimates the

true flow rate (Figure 2b). This inaccuracy resulting from fouling has important implications when fixed flow rate PID-mode is used for long-term experiments. The PID-loop enforces higher pressures than required and the real flow rate can quadruple (Figure 2b, blue plot) at the higher ranges of the sensor. This leads to exposure of the OoCs to higher mechanical stress than anticipated and possible misinterpretation of the perfusion experiments.

We further investigated the functionality of the constant pressure mode as we opted to perfuse parallel circuits using constant pressure. We found that the flow rate decreases when a constant pressure is applied to the reservoir liquid level (Figure 5). Conversely, when using the constant flow rate mode, the required pressure is increased. This observed effect is due to the P_{head} difference when the fluid is being transferred from one reservoir (decreasing positive contribution) to another (increasing resistance) (Figure 5a). Approximately 1.2 to 1.5 mbar per displaced ml of fluid was observed depending on fluidic density and used reservoir (Figure S3a,b). Depending on the total resistance of the circuit, this can lead to a significant decrease in flow rate (Figure 5a). This effect can be minimized by applying higher hydraulic resistance in front the OoCs; however, this solution may lead to undesired increased residence time or shear rates inside the tubing.

Liquid Level Measurement

The inaccuracy of the flow sensor following long-term exposure to cell culture medium also affects experiments in recirculation systems. To determine the correct timing for switching, the output of the flow sensor is used to calculate the total displaced volume. When this measured value is lower than the actual flow rate, medium reservoirs eventually empty and experiments fail ²³. To control the flow rate and recirculation without relying on these flow rate sensors, we integrated additional pressure sensors at the OoC and medium reservoirs.

Because of the P_{head} of the liquid, the medium level can be determined by measuring the pressure difference between the bottom of the reservoir and the air pressure above the liquid level. This can be achieved by inserting pressure sensors at the bottom of the reservoir (Figure 3a). This method is highly accurate, but due to direct exposure of the sensor to cell culture medium, the sensor may become fouled, less accurate and a source of (bacterial) contamination. Therefore, we investigated if we can accurately measure it remotely via a tube (Figure 3b). Although indeed accurate, we observed that when a reservoir is pressurized, the liquid is forced into the measurement tube and an abrupt increase in pressure is measured. When the pressure is reduced, the measured fluid decreases again. We tested two tube-diameters (0.8 mm and 3 mm) and found that by using a large tube diameter this measured effect is minimized.

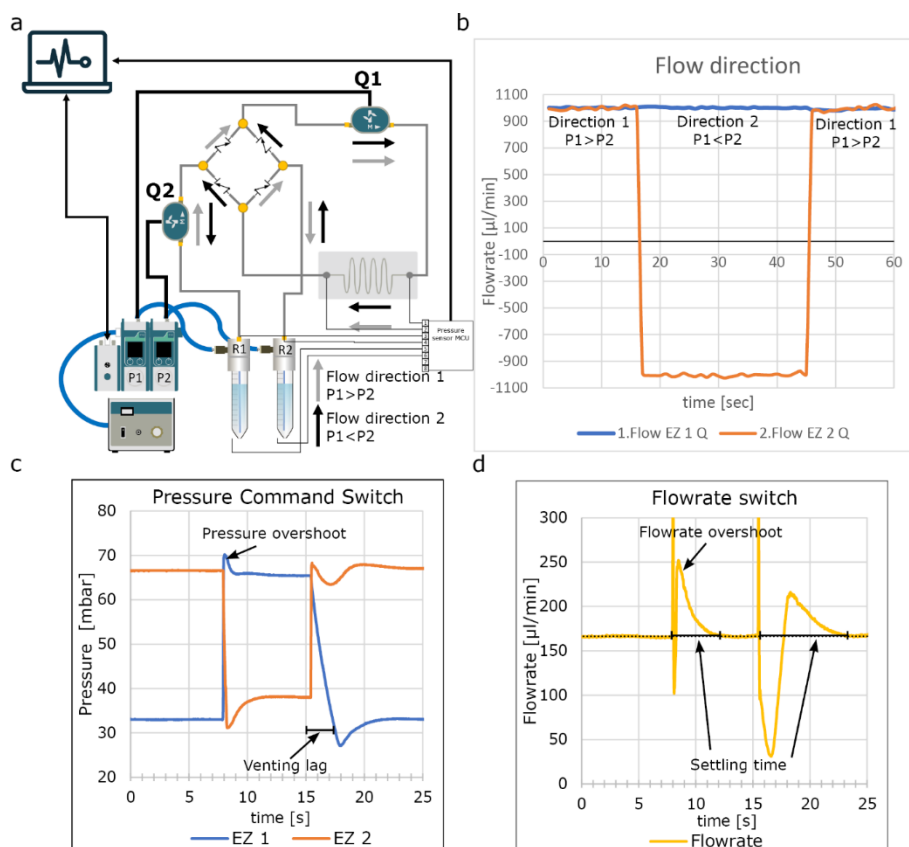


Figure 4: Graetz recirculation circuit. (a) Schematic of the fluidic circuit used shows the microfluidic analogy of the Graetz bridge used in an AC/DC converter using check valves; if the pressure in R1 is higher than R2, fluidic flow follows the gray arrows. When the pressure is reversed, fluidic flow follows the black arrows, remaining unidirectional at Q1 and bidirectional at Q2. (b) Direct measurement of the recirculation. When pressure commands are reversed, the flow is reversed at flow rate sensor Q2, however, remains unidirectional at flow rate sensor Q1. (c) High resolution recording of the pressure switch at the fluidic reservoirs shows small overshoot and undershoot in pressure resulting in spike in flow rate. Interestingly EZ1 vents slower than EZ2 affecting the algorithm. (d) Measured flow rate shows the overshoot due to the pressure overshoot and settling time of approximately 4 s, due to the venting lag of EZ1 settling time is approximately 8 s. See video S1 to see perfusion of suspended micro beads during switching.

Recirculation Using the Graetz-Recirculation Circuit

OoCs require relatively high flow rates to mimic many physiologically relevant conditions. However, if there are relatively few cells in the OoC, important signaling molecules may be diluted beyond detection by (other) cells or sensors. As experiments may take several weeks, it is important to be able to recirculate cell culture medium for cost effectiveness. Pressure driven fluidic circuits require actively controlled valves that need to be synchronized with the pressure commands²³. These valves are often bulky, challenging to implement and a potential source of bacterial contamination. Here we developed passive recirculation circuit based on an AC/DC converter circuit.

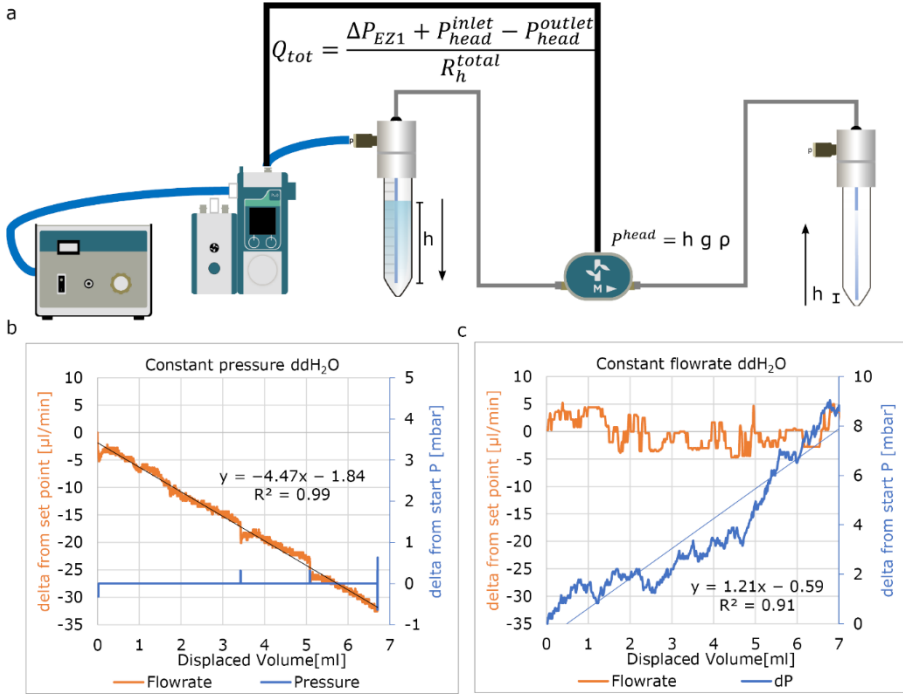


Figure 5: Controlling flow rate with fixed parameters. (a) Used fluidic circuit. **(b)** Applying a fixed pressure difference results in a constant decrease of the flow rate per displaced volume due to effect of P_{head} . **(c)** Fixed flow rate shows a steady increase in applied pressure due to the changing P_{head} using fixed flow rate.

It required four check valves oriented in a similar fashion as the diodes in a Graetz bridge (Figure 4a). This circuit is a cost effective, small footprint method to achieve unidirectional recirculation by simply switching the pressure of the pressure controllers (Figure 4b). To minimize disruption, it is essential to match the PID parameters to the fluidic circuit which can be easily done within the software we developed (Figure 4a,b).

We also observed the importance of quickly venting overpressure as this affects the settling time (Figure 4b,c). To validate the flow rate in the OoCs, we added fluorescent beads to the medium and recorded bead displacement during each directional switch (Video S1). This showed minimal disruption in the flow rate. The check valves we used are disposable, which reduces the risk of bacterial contamination by inadequate cleaning or rinsing. Furthermore, the passive fluidic circuit is less complex to implement and easier to scale as it requires no electronic wires or software. Microfabrication techniques have been described that further miniaturize the check valves in the microfluidic chips, minimizing swept and dead volumes ²⁴. For practical reasons, the inlet and outlet bridges are separated for long-term experiments as this allows the separation of inflow and outflow (Figure 1a).

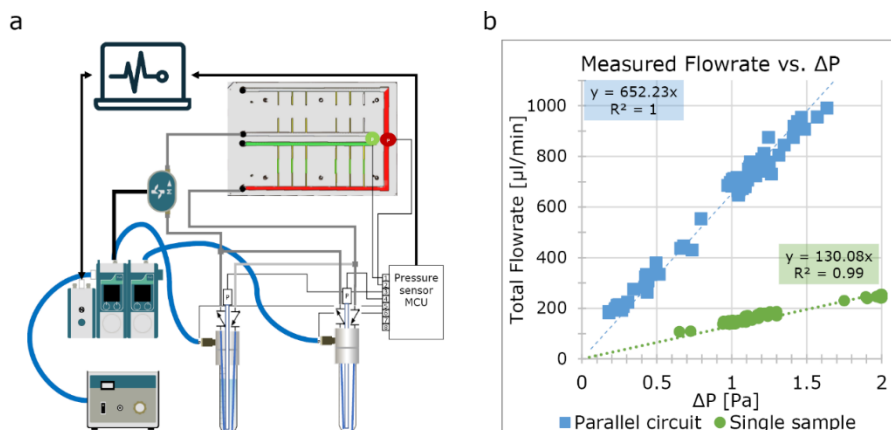


Figure 6: Flow rate vs. pressure difference. (a) Schematic of the used fluidic circuit shows the FCB with 6 channels connected. The free channels were blocked using a dummy chip. (b) Pressure difference relationship for a single channel (green plot) and six channels in parallel (blue plot). The measurements show correlation with the predicted values (Figure S4); however, the six channels in parallel show a 5-fold increase in flow rate dependence but this can be attributed to the tolerances of the fabricated FCB.

To control the flow rate of the OoCs, we applied a constant dP across the samples using the custom software. To validate this approach, we set up an FCB with six samples and an FCB with one sample (Figure 6). We compared these with the predicted values (Figure s4). Both plots showed the linear relation between the dP and flow rate, and the single sample correlated with the predicted flow rates. However, the multiplexed sample showed deviation from the model. These differences could be attributable to fabrication variation of the microfluidic devices used and the FCB.

To test the final system for long-term perfusion, we set up a single chip and perfused it for 48 h at a target pressure difference of 29 mbar to reach flow rate of approximately 200 $\mu\text{L}/\text{min}$ with ddH₂O to validate how the algorithm maintains an equal flow rate for over 48 h (Figure 7c). These results were as expected, validating this system for further use.

3.4 Current Limitations of the Presented System

Despite the advance the system we describe represents, there are some limitations that remain. The controlling software takes input from the 2 separate gauge pressure sensors connected to the fluidic board. Preferably this would be done using a differential sensor but at present, wet/wet differential sensors with the desired resolution were not available in a miniaturized format that would fit this concept design. The used MicroPressure sensors (MPR, Honeywell) have a small footprint, are low cost and can be used in both wet and dry conditions. By dampening the signal of

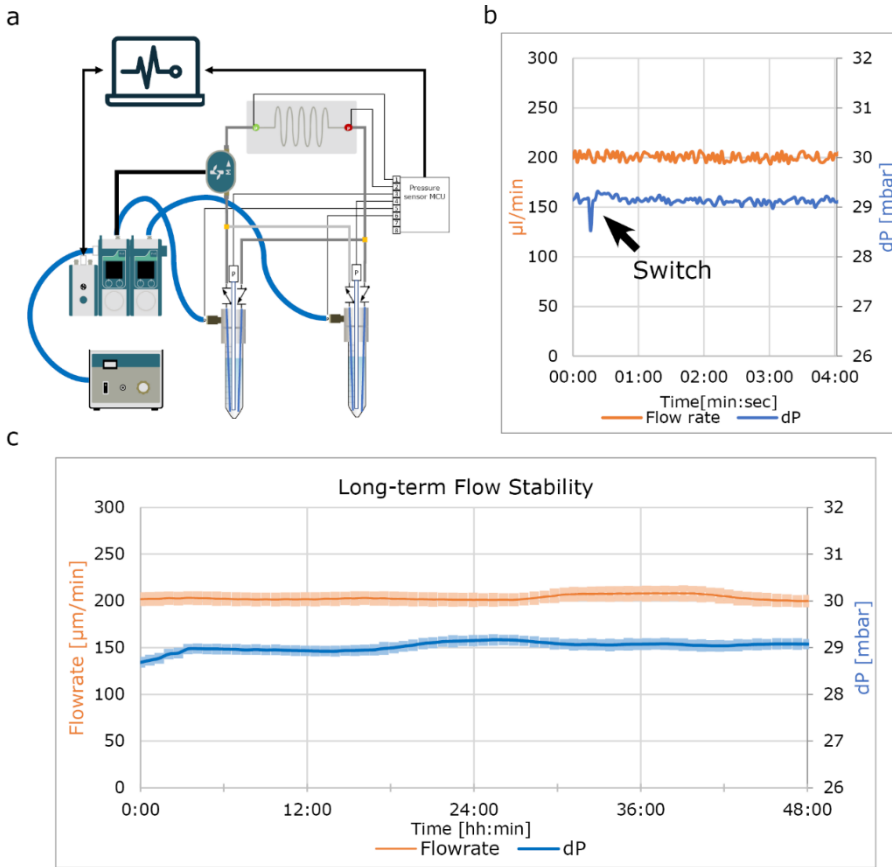


Figure 7: Long-term flow rate stability. (a) Schematic of the used fluidic circuit shows a single sample. For this experiment ddH₂O was used to demonstrate the functionality of the software in maintaining constant flow rate without the effect of sensor fouling. (b) Flow rate and pressure difference for 4 min during a flow reversal shows little variation. (c) Two day perfusion using ddH₂O shows minimal variation. Error band shows the interquartile range of that time segment.

2 separate gauge pressure sensors, the output could be used to calculate the dP. This approach resulted in stable and repeatable flow control despite the limitations of using two separate gauge pressure sensors for differential measurements as shown in this work, although this does affect the response time of the system.

3.5 Conclusions

In this work we investigated and optimized the use of pressure-driven flow circuits for OoC perfusion. We demonstrated that thermal flow rate sensors are not suitable for long-term cell cultures as these would affect flow rates and recirculation algorithms. We therefore optimized the OoC systems by stabilizing the flow rate using pressure sensors as they can control the flow rate in a more stable way and protect cells from unwanted mechanical stress. By measuring the liquid levels using pressure sensors, a reliable and flexible

recirculation algorithm was developed to perfuse for extended periods of time. We fabricated a passively controlled recirculation circuit from off-the-shelf components, which is an economical and less complex solution to other (commercially available) solutions. The software controlling the perfusion system is intuitive and can be used for different microfluidic devices at different flow rates without modification.

Author Contributions:

Conceptualization, M.N.S.d.G.; methodology, M.N.S.d.G. and A.V.; investigation, M.N.S.d.G.; resources, M.N.S.d.G and V.V.O.; writing—original draft preparation, M.N.S.d.G.; writing—review and editing, all authors; visualization, M.N.S.d.G.; supervision, V.V.O.; funding acquisition, A.D.v.d.M, C.L.M., and V.V.O. All authors have read and agreed to the published version of the manuscript.

Acknowledgements:

The authors would like to thank Sander van Berloo of the department of Medical Technology LUMC for the design and fabrication of the PCBs and MCU used for this work. This work was supported by the Netherlands Organ-on-Chip Initiative (NOCI), an NWO Gravitation project (024.003.001) funded by the Ministry of Education, Culture and Science of the government of the Netherlands.

3.6 Materials and Methods

Fabrication of the Fluidic Circuit Board

The FCB was fabricated as described previously²³. Briefly, it was composed of two cast 10 mm and one 15 mm polymethylmethacrylate Poly (methyl methacrylate) (PMMA) plates (Altuglass, Saint-Avoid, France), where all connecting channels and fittings for Luer-slip connectors were milled with a CNC micro mill (Datron Neo, Datron AG Mühlthal, Germany). The dimensions of fluidic circuit are shown in Table s2. After milling, the FCB was assembled as follows: both layers of the FCB were thoroughly cleaned using industrial cleaning wipes (Adolf Würth GmbH & Co, Duisburg, Germany), deionized water, absolute ethanol (Sigma-Aldrich, St. Louis, USA) and propanol (Sigma-Aldrich). A solution of acetone (Sigma-Aldrich) in absolute ethanol at a volume ratio of 1:10 was added on top of the connection layer slab and the complementary channel layer slab was then pressed onto the connection layer slab and aligned using alignment pins (DIN 7-ISO 2338). The assembled FCB was then pressed at 1 kN at 55 °C using a hydraulic press (model 3889, Carver Inc., Miami ,USA).

Fabrication of Microfluidic Devices

The microfluidic OoC devices were fabricated from polydimethylsiloxane (PDMS, Sylgard 184, Dow Corning, Midland, USA) using injection moulding as previously described²³. The dimensions of the flow channels were as described previously (1.1 cm × 500 µm × 500 µm; l × w × h). Briefly, PDMS

Table 1: Materials used for assembly of various fluidic circuits.

Material	Qty.	Manufacturer	Supplier	Product SKU:
FCB or single microfluidic device	-	Custom	-	-
Pressure cap for 15 mL Falcon -S (4 port)	2	ELVEFLOW	Darwin-microfluidics	LVF-KPT-S-4
15 mL reservoirs	2	Falcon		
Check valves	4	Master flex	Darwin-microfluidics	MF-30505-92
Flow sensor L or XL *	1 or 2	Fluigent	Fluigent	FLU_L_D_FDG
Flow EZ-line Up 345 mbar *	2	Fluigent	Fluigent	LU-FEZ-345
Link-up	1	Fluigent	Fluigent	LU-LNK-0002
Pressure sensors *	4-6	Honeywell	Farnell	MPRLS0300YG0001 B
Luer to 1/16 barb	24	IDEX	Darwin-microfluidics	CIL-P-854
¼-28-Female-to-male Luer adapter	2	IDEX	Darwin-microfluidics	CIL-P-655-01
3-way valve	2	IDEX		

Perfusion system to control multiplex and recirculate OoCs

¼-28-Female-to-Female Luer Lock adapter	2in	IDEX	Darwin- microfluidics	CIL-P-678
Y-connectors	2	IDEX	Darwin- microfluidics	CIL-P-512
PTFE tubing-1/16" OD X 1/32" ID*		ELVEFLOW	Darwin- microfluidics	LVF-KTU-15
Printed circuit board (PCB) for pressure sensor	1	custom		
Arduino or other MCU	1	Arduino		
Ribbon wires	4-6			
optional:				
Microfluidic Manifold 9 Port	2	ELVEFLOW	Darwin- microfluidics	LVF-KMM-02
2-Switches	2	Fluigent	Fluigent	2SW002
Pressure source 1.2 bar	1	Fluigent	Fluigent	FLPG005
* Pressure and flow-rate range are setup depended				

and base agent (Sylgard 184, Dow Corning) was mixed 10:1 (w:w) with curing agent and degassed. The degassed PDMS was transferred to a syringe and further degassed. The injection mould was assembled using six neodymium block magnets (N42, 1.3T, approximately 60 N per magnet, Webcraft GmbH, Gottmadingen, Germany) and the PDMS was slowly injected. The filled injection-mould was set vertically at room temperature (19-22 °C) overnight. Afterwards, the PDMS was further cured at 75°C for 60 min. The PDMS was carefully peeled off and excess PDMS was removed using a surgical knife. PDMS devices and round cover glasses (#1.5, ø30 mm Thermo Scientific, Waltham, USA) were surface-activated using air plasma (45 s, 50 Watt at 60 Pa, CUTE-Femto Science Gyeonggi-do, Republic of Korea) and contact-bonded using light pressure.

Assembly of the Perfusion System

Fluidic and electronic components were obtained from commercial sources. The complete list of components used for the fluidic circuits described is shown in Table 1. Various fluidic circuits were used to demonstrate the different aspects of the setup and software and are shown at the relevant figure.

Pressure Controllers

Two EZ-LineUP (Fluigent, 345 mbar) pressure controllers were used to control the air pressure of the medium reservoirs. To connect the controllers to the laptop, the link-up module (Fluigent) was used. The left-most EZ- LineUP controller was designated as EZ1 and the right-controller as EZ2.

Flow Sensors

A thermal flow sensor (Fluigent) was connected to EZ1-LineUP. Two different ranges were used: size L (–1100 to +1000 µL/min) and size XL (–5500 to +5500 µL/min). The flow rate sensor of EZ1 measures the total flow rate of the circuit to validate perfusion. When experiments required a second flow sensor, this was connected to EZ2 and recorded using All-in-one software (A-i-O, Fluigent).

Pressure Sensors

Pressure sensors (MPRLS0300Y, Honeywell, Charlotte, USA) were obtained and soldered onto a custom PCB which allowed the connection of ribbon wires according to the manufacturer's instructions. These ribbon wires were connected to an MCU. The MCU was then connected to the controlling laptop via a USB. The MCU emits at 100 Hz 24-bit pressure output of 8 sensors. Alternatively, an Arduino MCU can be used (Baudrate:250000) To be able to read the MCU using the software, the serial port needs to be set to COM3.

Flow Rate Sensor Validation

A flow rate sensor (Fluigent, XL) was thoroughly cleaned by rinsing with 70%/30% ethanol/ddH₂O, followed by incubation with hypochlorite (Glorix,

Unilever, London) for 20 min. After incubation the sensor was subsequently rinsed with 10 mL ddH₂O, 10 mL propanol and dried with nitrogen. The flow sensor was used in a fluidic circuit connected to a 10 mL pipette (Figure 2). Endothelial Cell Growth Medium _2 (EGM-2) containing 2% serum (in anticipation of future of use for endothelial cells in vessel-on-chip models) was used as fluid and the Flow-EZ was set to fixed flow rate using the manufacturer's PID-loop at room temperature. At every millilitre mark, the time-delta was noted for at least 3 mL. Using this time-delta, the flow rate was calculated and compared to the set flow rate. The setup was allowed to recirculate for 48 h and the experiment then repeated.

Liquid Level Measurement

Standard 15 mL Falcon tubes combined with 4-port pressure caps (Elveflow) were used as medium reservoirs. Two different methods were used to insert the required pressure sensors.

To directly measure the liquid level, a hole was punched using a 2 mm biopsy puncher in the bottom of the 15 mL Falcon tube to create a leak-tight seal with the long-port of the sensor (Figure 3a). Care was taken to remove any air pockets between the sensor and the liquid.

To remotely measure the liquid level, a tube was placed at the low liquid level through one of the ports of the pressure cap and the reference sensor was inserted (Figure 3b).

Graetz Recirculation Circuit Validation.

Two flow sensors (size L) were first calibrated against each other and placed in the fluidic-circuit as shown in Figure 4. Using the software, the "recirculation algorithm" was executed and measured using the A-i-O Fluigent at 20 Hz.

Validation of Flow Rate Control Using Applied dP

Two microfluidic devices with a total of 6 channels were connected to the FCB. The other ports were blocked using dummy chips (no perfusable channels). The circuit was primed using equilibrated EGM-2 at 37 °C. The medium was equilibrated by placing a culture flask of medium inside an incubator (37 °C, 5% CO₂) for at least 2 h. Fluidic reservoirs were placed into a heat block set at 37°C. A flow rate sensor with a maximum of 1100 µL/min was used (Fluigent, size L). The system was completely bled from air and pressure sensors were correctly calibrated. The dP was allowed to increase slowly until the maximum of the flow sensor was reached; the flow rate was then plotted against the measured pressure difference. Measurements were performed on a single channel, while all other channels were blocked using dummy chips, and the experiment was repeated with 6 channels connected to the FCB.

Long-Term Perfusion

An 8 cm length of tubing (diameter: 250 μm) was placed between two T-junctions. The pressure sensors were inserted into the available port and the system was primed with ddH₂O. All sensors were correctly calibrated, and the system was allowed to recirculate for 48 h with a dP of 29 mbar.

Code Availability

The Python code can be found at the GitHub repository ²⁵.

Supplementary Materials

See supplementary material for a detailed overview of the software functionality, FCB dimensions and supplementary figures.

References

- 1 Ingber, D. E. Human organs-on-chips for disease modelling, drug development and personalized medicine. *Nat Rev Genet* **23**, 467-491, doi:10.1038/s41576-022-00466-9 (2022).
- 2 Bhatia, S. N. & Ingber, D. E. Microfluidic organs-on-chips. *Nat Biotechnol* **32**, 760-772, doi:10.1038/nbt.2989 (2014).
- 3 Wu, Q. *et al.* Organ-on-a-chip: recent breakthroughs and future prospects. *Biomed Eng Online* **19**, 9, doi:10.1186/s12938-020-0752-0 (2020).
- 4 Junaid, A., Mashaghi, A., Hankemeier, T. & Vulto, P. An end-user perspective on Organ-on-a-Chip: Assays and usability aspects. *Curr Opin Biomed Eng* **1**, 15-22, doi:10.1016/j.cobme.2017.02.002 (2017).
- 5 Busek, M., Aizenshtadt, A., Amirola-Martinez, M., Delon, L. & Krauss, S. Academic User View: Organ-on-a-Chip Technology. *Biosensors (Basel)* **12**, doi:10.3390/bios12020126 (2022).
- 6 Thompson, C. L., Fu, S., Heywood, H. K., Knight, M. M. & Thorpe, S. D. Corrigendum: Mechanical Stimulation: A Crucial Element of Organ-on-Chip Models. *Front Bioeng Biotechnol* **9**, 658873, doi:10.3389/fbioe.2021.658873 (2021).
- 7 Pradhan, S. *et al.* Biofabrication Strategies and Engineered In Vitro Systems for Vascular Mechanobiology. *Adv Healthc Mater* **9**, e1901255, doi:10.1002/adhm.201901255 (2020).
- 8 Dessalles, C. A., Leclech, C., Castagnino, A. & Barakat, A. I. Integration of substrate- and flow-derived stresses in endothelial cell mechanobiology. *Commun Biol* **4**, 764, doi:10.1038/s42003-021-02285-w (2021).
- 9 Byun, C. K., Abi-Samra, K., Cho, Y. K. & Takayama, S. Pumps for microfluidic cell culture. *Electrophoresis* **35**, 245-257, doi:10.1002/elps.201300205 (2014).
- 10 van Duinen, V. *et al.* 96 perfusable blood vessels to study vascular permeability in vitro. *Sci Rep* **7**, 18071, doi:10.1038/s41598-017-14716-y (2017).
- 11 Wang, Y. I., Abaci, H. E. & Shuler, M. L. Microfluidic blood-brain barrier model provides in vivo-like barrier properties for drug permeability screening. *Biotechnol Bioeng* **114**, 184-194, doi:10.1002/bit.26045 (2017).
- 12 Ni, C. W., Qiu, H. & Jo, H. MicroRNA-663 upregulated by oscillatory shear stress plays a role in inflammatory response of endothelial cells. *Am J Physiol Heart Circ Physiol* **300**, H1762-1769, doi:10.1152/ajpheart.00829.2010 (2011).
- 13 Wang, C., Baker, B. M., Chen, C. S. & Schwartz, M. A. Endothelial cell sensing of flow direction. *Arterioscler Thromb Vasc Biol* **33**, 2130-2136, doi:10.1161/ATVBAHA.113.301826 (2013).
- 14 Wang, Y. I. & Shuler, M. L. UniChip enables long-term recirculating unidirectional perfusion with gravity-driven flow for microphysiological systems. *Lab Chip* **18**, 2563-2574, doi:10.1039/c8lc00394g (2018).
- 15 Kaarj, K. & Yoon, J. Y. Methods of Delivering Mechanical Stimuli to Organ-on-a-Chip. *Micromachines (Basel)* **10**, doi:10.3390/mi10100700 (2019).
- 16 Weiss, M., Neff, T., Gerber, A. & Fischer, J. Impact of infusion line compliance on syringe pump performance. *Paediatr Anaesth* **10**, 595-599, doi:10.1111/j.1460-9592.2000.566ab.x (2000).
- 17 Klespitz, J. & Kovács, L. in *2014 IEEE 12th International Symposium on Applied Machine Intelligence and Informatics (SAMII)*. 191-194.
- 18 Behrens, M. R. *et al.* Open-source, 3D-printed Peristaltic Pumps for Small Volume Point-of-Care Liquid Handling. *Sci Rep* **10**, 1543, doi:10.1038/s41598-020-58246-6 (2020).
- 19 Martin, M., Blu, G., Eon, C. & Guiochon, G. The use of syringe-type pumps in liquid chromatography in order to achieve a constant flow-rate. *Journal of Chromatography A* **112**, 399-414, doi:10.1016/s0021-9673(00)99972-2 (1975).
- 20 Stone, H. A., Stroock, A. D. & Ajdari, A. Engineering flows in small devices: Microfluidics toward a lab-on-a-chip. *Annu Rev Fluid Mech* **36**, 381-411, doi:10.1146/annurev.fluid.36.050802.122124 (2004).
- 21 Oh, K. W., Lee, K., Ahn, B. & Furlani, E. P. Design of pressure-driven microfluidic networks using electric circuit analogy. *Lab Chip* **12**, 515-545, doi:10.1039/c2lc20799k (2012).
- 22 Poon, C. Measuring the density and viscosity of culture media for optimized computational fluid dynamics analysis of in vitro devices. *J Mech Behav Biomed Mater* **126**, 105024, doi:10.1016/j.jmbbm.2021.105024 (2022).
- 23 Vivas, A., van den Berg, A., Passier, R., Odijk, M. & van der Meer, A. D. Fluidic circuit board with modular sensor and valves enables stand-alone, tubeless microfluidic flow control in organs-on-chips. *Lab Chip* **22**, 1231-1243, doi:10.1039/d1lc00999k (2022).
- 24 Nguyen, N. T., Truong, T. Q., Wong, K. K., Ho, S. S. & Low, C. L. N. Micro check valves for integration into polymeric microfluidic devices. *J Micromech Microeng* **14**, 69-75, doi: 10.1088/0960-1317/14/1/309 (2004).

Chapter three

- 25 de Graaf, M. N. S. *PID-controller for microfluidic flow*,
<<https://github.com/mnsdegraaf/mfcb>> (2022).

Chapter three: Supplementary materials

Pressure-driven perfusion system to control, multiplex and recirculate cell culture medium for Organs-on-Chips

Electronic supplementary information and supplementary videos available at:

<https://doi.org/10.3390/mi13081359>



Code available at:

<https://github.com/mnsdegraaf/mfcb>



Supplementary Figures

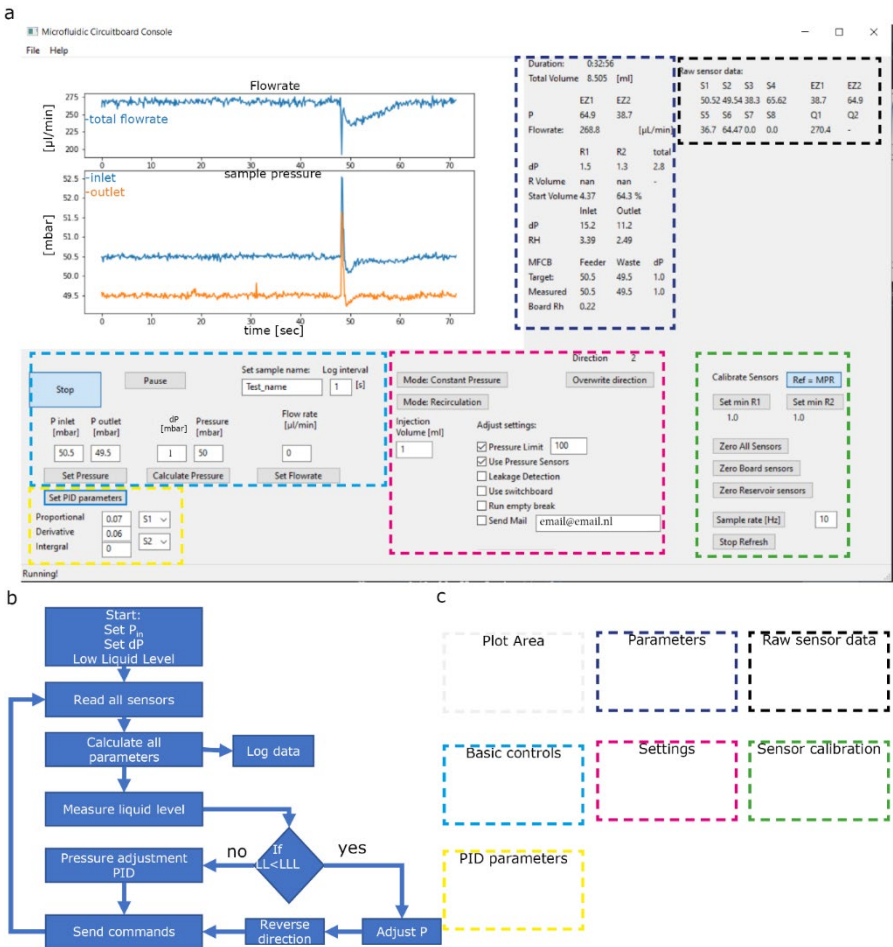


Figure S1 Software overview. (a) screen shot of the custom software showing controlling buttons and parameters plots (b) Feedback loop of the software. It starts with reading all sensors and calculate the pressure difference between the inlet and outlet, internal pressure and liquid levels. The PID-controller will adjust the commands to reach the setpoints. (c) Overview of all functions and parameters, explanation in table s1.

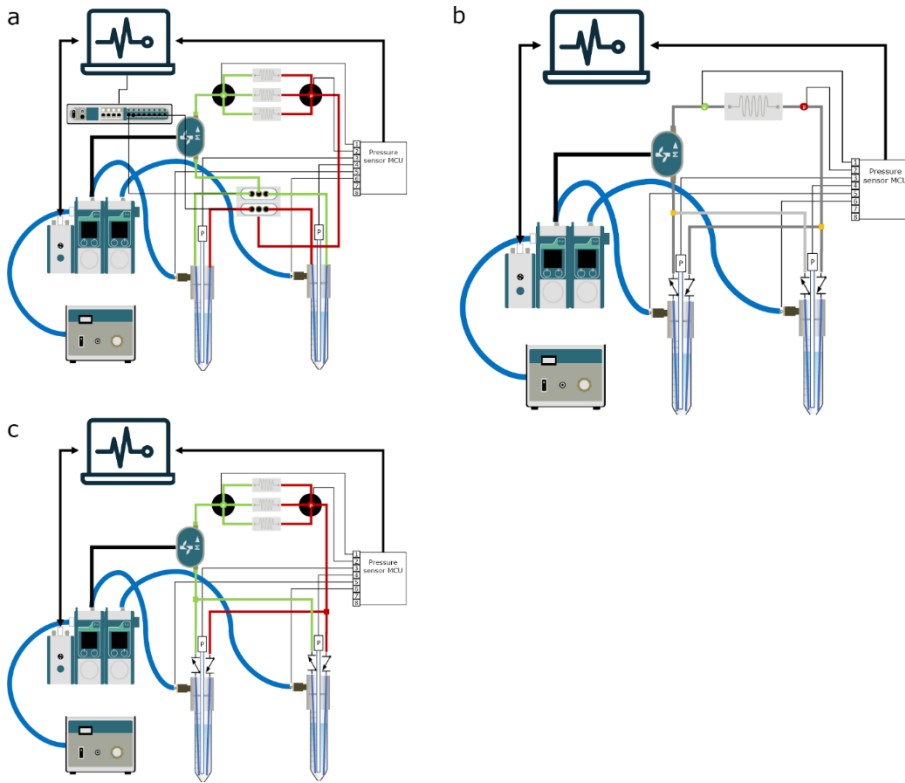


Figure S2. Examples of alternative fluidic circuits. (a) recirculation using actively controlled 3/2 valves (Fluigent) **(b)** Single OoC perfusion, **(c)** multiplexing using of the shelf manifold splitters.

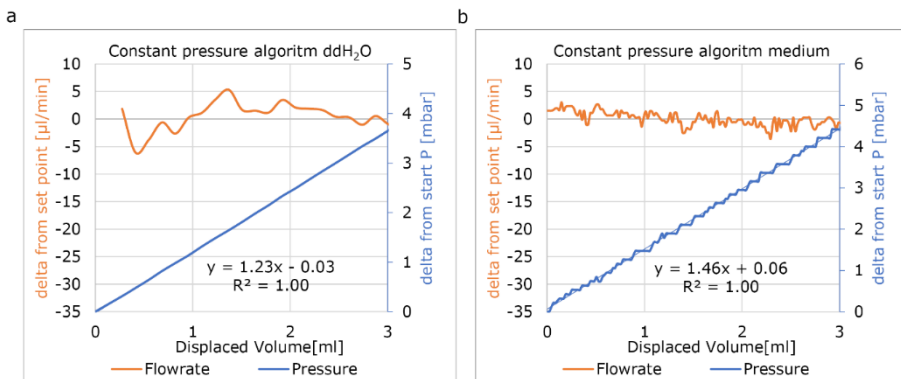


Figure s3 Typical total pressure increase using the custom PID-controller (a) Pressure increase per displaced ml of ddH₂O. **(b)** Pressure increase per displaced ml of medium

Chapter three

Table S1: Software functionality.

Parameters	Info:
Duration	Total experimental time
Total Volume	Total displaced volume
P	Pressure at controller (filtered)
Flowrate	Total flowrate (filtered)
dP R1 R2	Measured P-head (filtered)
R volume	Calculate Volume
Start volume	Start volume, % measured at present
inlet dP	dP inlet Reservoir to Feeder channel
outlet dP	dP Waste-channel to outlet Reservoir
MFCB	Sample parameters
Target Pressure	target difference pressure
Measured Pressure	Measured pressure (difference)(filtered)
Board Rh	Sample resistance(filtered)
Raw sensor data	Unfiltered sensor output
Basic control	
start/stop	Start / stop experiments
Pause	Sends no commands, keeps logfile alive
P inlet/P outlet	Set target inlet/outlet
Set pressure	Sends input to controller
Shear/dp/Pressure	set target pressure difference and internal pressure
calculate pressure	Sends input to controller
Set flowrate	Set flowrate
Set sample name	Logfile name
log interval	sets log frequency in seconds
PID parameters	
Set PID parameters	Adjust parameters
Proportional	P-parameter
Derivative	D-parameter
Integral	I-parameter
Settings	
Mode: Constant Pressure /	Change process variable
Constant flowrate	Continuous recirculation,
Mode: Recirculation /	Injection target volume with recirculation
Injection	Target injection
injection volume	force direction switch
overwrite direction	Limits pressure to protect sample
Pressure limit	Use manufactures PID loop
Use pressure sensors	Switch off when volume is below 85% of start volume
Leakage detection	sends 3/2 switch commands
Use switchboard	

Run empty break	If flow>0 break
send mail	Sends emails with Situation Reports or leakage/empty break
Sensor calibration	
Ref MPR/EZ	Calculate reservoir dP with EZ command or pressure sensor
Set min R1/R2	set low liquid level
Zero all sensors	auto zero all sensors
Zero board sensors	auto zero board sensors
Zero reservoir sensors	auto zero reservoir sensors
Sample rate	Change frequency of algorithm
Stop refresh	Pauses algorithm

Table S2: Channel dimensions FCB.

Dynamic Viscosity	Cell culture medium @ 37 °C, 2% serum ¹			7.90E-04 [Pa S]
	Length [m]	Width [m]	Height [m]	R _h [Pa s m ⁻³]
Feeder channel	0.2	0.0025	0.002	1.90E+08
Feeder loop	0.01	0.0012	0.002	4.40E+07
			Total	2.34E+08
Waste channel	0.2	0.0025	0.002	1.90E+08
waste loop	0.082	0.0035	0.002	4.33E+07
			Total	2.34E+08
Resistor calculated	0.010	5.00E-04	2.50E-04	1.77E+10
Total Chip connection				4.39E+10
Empty microfluidic channel	0.011	5.00E-04	5.00E-04	4.48E+09

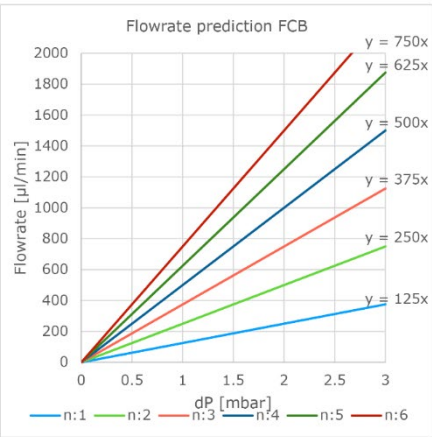


Figure S4: Prediction of flowrates Prediction of multiplexed microfluidic channels. (1 to 6) using pressure controlled perfusion. Dimensions listed in table s2 and EQ 5 and 6 were used to calculate this prediction.

References

1 Poon, C. Measuring the density and viscosity of culture media for optimized computational fluid dynamics analysis of in vitro devices. *J Mech Behav Biomed Mater* **126**, 105024, doi:10.1016/j.jmbbm.2021.105024 (2022).

Chapter four:

Multiplexed fluidic circuit board for controlled perfusion of 3D blood Vessels-on-a-Chip

Mees N. S. de Graaf¹, Aisen Vivas^{2,3}, Dhanesh G. Kasi^{1,4,5},
Francijna E. van den Hil¹, Albert van den Berg³, Andries D. van der Meer²,
Christine L. Mummery^{1,2}, Valeria V. Orlova^{1*}

¹ Department of Anatomy and Embryology, Leiden University Medical Center

² Applied Stem Cell Technologies, University of Twente

³ BIOS Lab on a Chip Group, MESA+ Institute for Nanotechnology, Technical Medical Centre, Max Planck Institute for Complex Fluid Dynamics, University of Twente

⁴ Department of Human Genetics, Leiden University Medical Center

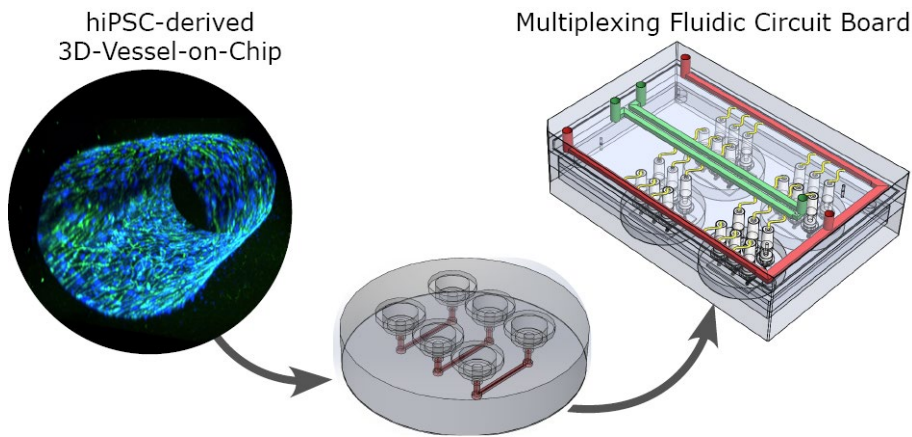
⁵ Department of Neurology, Leiden University Medical Center

Published in Lab Chip, 2023, 23, 168-181

<https://doi.org/10.1039/D2LC00686C>



Abstract



Three-dimensional (3D) blood vessels-on-a-chip (VoC) models integrate the biological complexity of vessel walls with dynamic microenvironmental cues, such as wall shear stress (WSS) and circumferential strain (CS). However, these parameters are difficult to control and are often poorly reproducible due to the high intrinsic diameter variation of individual 3D-VoCs. As a result, the throughput of current 3D systems is one-channel-at-a-time. Here, we developed a fluidic circuit board (FCB) for simultaneous perfusion of up to twelve 3D-VoCs using a single set of control parameters. By designing the internal hydraulic resistances in the FCB appropriately, it was possible to provide a pre-set WSS to all connected 3D-VoCs, despite significant variation in lumen diameters. Using this FCB, we found that variation of CS or WSS induce morphological changes to human induced pluripotent stem cell (hiPSC)-derived endothelial cells (ECs) and conclude that control of these parameters using a FCB is necessary to study 3D-VOCs.

4.1 Introduction

Blood vessels are crucial for distributing vital nutrients and removing metabolic waste products from the human body and are crucial for proper organ function^{1, 2}. Diseased vasculature can lead to a wide variety of diseases including arteriosclerosis³, aneurysms⁴ and sepsis⁵. One way to recapitulate the functionality of vasculature accurately, is to reconstruct the complex microenvironment of blood vessels *in vitro* using microfluidic technology to generate 'vessel-on-chip' (VoC) models^{6, 7}.

Blood vessels are lined with endothelial cells (ECs) surrounded by pericytes or smooth muscle cells that are collectively called mural cells. Mural-EC interaction is vital for blood vessel function and is an important factor in the onset of complex multicellular diseases^{8, 9}. Furthermore, mural cells mechanically support ECs and enable efficient distribution of blood flow by contraction or dilation of the vessel. Inside organs, ECs form a tissue-specific-barrier and control the nutrient flux from the blood to tissue¹⁰. Additionally, ECs are important in mediating the inflammatory response via regulating leukocyte trafficking^{11, 12}.

The EC phenotype is highly plastic and is continuously influenced by many biological cues that include the surrounding tissue cells, extracellular matrix (ECM), and drugs^{13, 14}. In addition, haemodynamic forces, like the wall shear stress (WSS) and circumferential strain (CS), are important modulators of EC phenotype and function^{15, 16}. Haemodynamic forces vary across blood vessels of different diameters and depend on the location of the vessel in the vascular "tree".

WSS is the force parallel to the blood flow, exerted on the vessel wall due to viscous forces. WSS depends on the flow rate, luminal diameter and the viscosity of blood¹⁷. In healthy blood vessels, ECs are exposed to unidirectional laminar flow with mean WSS ranging from 0.1 Pa to 5 Pa *in vivo*, depending on the blood vessel location in the vascular bed, while, in larger arteries flow can also be turbulent because of increased diameters or bifurcations. ECs have multiple molecular mechanisms that can sense and react to changes in WSS by modulating the cellular response¹⁸.

CS is the deformation of the blood vessels due to pressure differences between the lumen and surrounding tissue and results in the stretching of ECs¹⁹. Due to the cardiac cycle and location in the vascular tree, CS can be either cyclic (aorta and arteriole) or constant (capillaries)²⁰. CS is defined as $\Delta L/L$ where L is the perimeter length of the vessel wall. CS is known to modulate many endothelial processes like, actin reorganization and focal adhesions²¹, matrix remodelling²² and apoptosis^{23, 24}. Typical physiological values can be up to 15 % and higher values are considered pathological²⁵.

Microfluidic technology allows engineering of three-dimensional (3D) blood-vessels-on-a-chip (VoC) that combine not only various cell types, but also ECM and haemodynamic forces. Different methods to engineer 3D-VoCs have been developed for various purposes and include, but are not limited to, 3D-bioprinting^{26, 27}, template casting^{28, 29} and cellular self-assembly^{30, 31}.

The top-down engineering of 3D-VoCs is preferred over self-assembly methods when controlled haemodynamic forces are required. The resulting 3D-VoCs are versatile and can support a range of different ECM and cell types and can be used to investigate the endothelial barrier function²⁹, tissue-specific and mural-cell interaction^{32, 33} and leukocyte migration³⁴.

To introduce haemodynamic forces in VoCs, controlled flow is applied using microfluidic pumps^{29, 35, 36}. The programmed flow rate depends on the luminal diameters and is set to match the *in vivo* situation of interest. Using controlled microfluidic pumps, WSS of the capillary, for instance, can be mimicked in a larger, more tractable 3D model.

Nevertheless, increasing the throughput of perfusion systems remains a challenge. To do this, methods are being developed to increase the throughput of perfusion systems by multiplexing fluidic circuits. The fluidic Circuit Board (FCB) offers a practical solution and various FCBs are being developed to multiplex OoCs. FCBs are microfluidic analogues of printed circuit boards (PCBs) and are designed to simplify the perfusion of organ-on-chip devices by combining multiple microfluidic components on a microplate footprint³⁷. We previously described different FCBs to multiplex perfusion in OoCs from highly complex controlled circuits, to simple fluidic “distributing” circuits³⁸⁻⁴⁰. Haemodynamic parameters in 2D-OoCs can be controlled precisely when the dimensions of the culture chambers are known. Therefore, in 2D-OoCs, a single set of perfusion parameters is sufficient for the accurate flow control. On the other hand, controlling hemodynamic parameters is challenging in 3D-OoCs when the exact dimensions are not known due to a high intrinsic variability.

Template removal²⁰, cell-seeding^{33, 36}, hydrogel structure⁴¹, incubation times²⁸ and biological response³⁴ can contribute to diameter variance which results in complexity of the multiplexed perfusion. The compliance of the patterned ECM further increases diameter variation when perfused, as fluidic pressure will also deform soft materials from which the channels are made³⁶. To account for these significant luminal diameter differences, individual control parameters need to be corrected to ensure equal WSS among the different replicates to maintain equal experimental conditions.

In this study, we demonstrated a simple solution to circumvent intrinsic diameter variation of 3D-VoCs to induce equal haemodynamics forces using a single set of control parameters. We optimized our previously developed

FCB⁴⁰ to perfuse up to twelve 3D-VoCs with variable luminal diameter while maintaining comparable WSS. The FCB described here has several advantages: (1) it maintains stable WSS and CS in 3D-VoCs using a single pressure difference, even if their diameters vary; (2) it allows simultaneous perfusion of up to twelve 3D-VoCs; (3) the FCB allows “plug-and-play” connection of 3D-VoCs and (4) it is fully compatible with standard microscope-stages, allowing automated imaging while being fully functional.

4.2 Experimental

To multiplex the perfusion of the 3D-VoC devices, we designed a FCB where multiple VoCs can be connected simultaneously in a parallel fluidic circuit (Fig. 1). This resolves the complexity commonly experienced when connecting multiple VoCs to a microfluidic set-up and, in addition, reduces the tedious task of cutting individual pieces of tubing with varying lengths to connect the different system components.

The fluidic circuit consists of a main feeder channel (Fig 1a, FCB green channel) that has individual branches towards the VoCs (yellow channels). The fluidic flow is then collected in a central waste channel (red channel) that directs the flow towards the opposite medium reservoir. In the central feeder and waste channels, two pressure sensors are inserted that act as the process variable for a proportional-integral-derivative (PID) controller run by custom software³⁵. The FCB used can connect up to four VoC devices, each containing three microfluidic channels (Fig 1 b).

To circumvent the 3D-VoC diameter variation, samples are connected in parallel from a central feeder channel via branching channels that have specific dimensions, referred to as equilibrating shear-, or τ EQ-Resistors (Fig. 1c, yellow). These τ EQ-resistors are fluidic resistors that are optimized to ensure that WSS is stable for a specific range of diameters of 3D-VoCs using Eq. s8. The design principle is flexible, as it can be optimized for all different diameter ranges. Their functionality can be explained using an electrical circuit analogy⁴². When a constant ΔP is applied between the feeder and waste channel, two hydraulic resistances (R_h) are present in each individual VoC channel: (1) the 3D-VoCs and (2) the respective τ EQ-resistor. The flow rate can then be predicted using Eq. s2 where the flow rate is determined by the sum of both R_h . When a 3D-VoC has a diameter in the lower range of the expected variation, the summed R_h will be high, leading to a lower flow rate. When the diameter is in the higher range, the R_h of the 3D-VoCs is lower and therefore the summed R_h will be lower, thereby increasing the flow rate through this VoC. The result is that, at a constant ΔP , 3D-VoCs with a small diameter will receive less fluid flow than 3D-VoCs with a large diameters, thereby maintaining the WSS within a narrow window of variation for all 3D-VoCs.

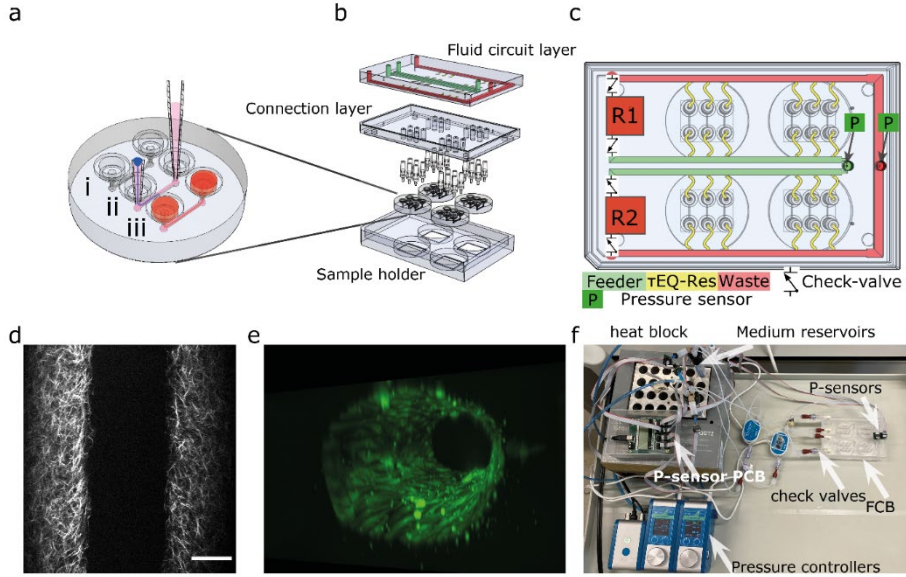


Figure 1: Design of the microfluidic system. (a) The round microfluidic devices contain 3 microfluidic channels: (i) microfluidic channels are 1.1 cm long and 500x500 μm (wxh); (ii) VFP consists of injection of a viscous collagen mixture (pink) into the channel followed by a droplet of PBS; (iii) Pipette-tips are removed and cells can be seeded. (b) Expanded view of the Fluidic Circuit Board, which consists of a fluidic circuit top-layer, a connection layer housing the luer-to-1/16" barb connectors to four individual devices. (c) The fluidic circuit contains two medium reservoirs (R1,R2) connected to pressure controllers (not shown), a feeder channel (green), τEQ -resistors (yellow) and a waste channel (red) Check valves are located at the medium reservoirs so recirculation can be achieved by switching high- and low pressure between the reservoirs. (d) 2p-SHG image shows the collagen fibrillar structure that reveals the lumen. (e) 3D reconstruction of TUBA1B-eGFP-ECs used for this study. (f) Photograph of the tested Fluidic circuit board, connected to the external medium reservoirs in a heat block. Scalebar 100 μm .

The required ΔP for a desired WSS can be calculated using the following equation assuming uniform lumen diameters:

$$\Delta P = \tau \left(4 \frac{L_v}{d} + \frac{3\pi d^3 L_{res}}{8wh^3(1-0.63\frac{h}{w})} \right) \quad \text{Eq. 1}$$

where ΔP is the required pressure setting [Pa], τ is the intended WSS [Pa], L_v the 3D-VoC length [m], d the 3D-VoC diameter [m], L_{res} length of the τEQ -resistor [m], w width and h height of the τEQ -resistor [m]. The CS is controlled by controlling the back pressure of the receiving fluidic reservoir until the P_{FCB} achieves the desired internal pressure, while maintaining the same ΔP .

The microfluidic circuit is designed to recirculate cell culture medium using a passively controlled fluidic circuit analogue to a Graetz-bridge (Fig 1c). A more detailed description of the functionality is provided elsewhere⁴⁰. In short, unidirectional flow is achieved by placing 4 microfluidic check valves in a fluidic circuit similar to that of a Graetz-rectifier bridge. When the pressure

commands are inversed as the reservoir empties, flow remains unidirectional at the samples without the use of actively synchronized electronic valves.

4.3 Results and Discussion

Design of the fluidic circuit board (FCB) for multiplexed and controlled perfusion of 3D vessels on chip (3D-VoCs)

The FCB developed for multiplexing up to twelve 3D-VoCs in parallel is shown in Fig 1a-c. The fluid circuit consists of two fluidic reservoirs (R1,R2), a feeder-channel (green, inner loop), a waste channel (red, outer loop) and parallel branching channels that distribute the medium towards the individual samples, referred to as τ EQ resistors (yellow). The dimensions of these τ EQ-resistors can be optimized for any expected sample diameter range using Eq. s9 or Eq. s10 to minimize WSS for that specific diameter range. The proposed design for this FCB is flexible, with only the length or height of the τ EQ-resistors needing adjustment when a different range is required; this can be directly milled in the PMMA. For this prototype, medium reservoirs, check valves and flow sensors were placed off the FCB to reduce the number of fabrication steps, using off-the-shelf components listed in Table 1 and connected using standard microfluidic tubing following the same circuit scheme (Fig. 1f). This fluidic circuit was designed to perfuse four microfluidic chips sharing the same medium. This single fluidic circuit is a simple platform that allows conditioning of as many as twelve 3D-VoCs simultaneously for higher throughput. Furthermore, the fluidic circuit could be adapted for additions in the future, such as combining different tissue-specific 3D-VoCs and other OoCs with shared medium as in the "Body-on-Chip" concept⁴³. Alternatively, microfluidic circuits may be separated by designing a complex pneumatic system³⁸, to be able to apply different chemical conditions on one plate

Pressure was controlled using two 345 mbar (34.5 kPa, 260 mmHg) pneumatic pressure controllers connected to the medium reservoirs to mimic the full range of the human physiological blood pressure. A custom-written PID-controller was programmed to maintain a constant ΔP between feeder and waste channel⁴⁰. The desired luminal pressure (P_{lumen}) was controlled by raising the back-pressure of the receiving reservoir. Depending on the tubing and check-valves used, a minimum P_{lumen} of 20 mbar is required at 1 Pa of WSS, with a P_{lumen} that can range up to 325 mbar. Importantly, the pressure head of the reservoir liquid level influences the minimum pressure up to 8 mbar. Higher WSS up to 5 Pa is possible at the cost of higher minimum P_{lumen} and a lower maximum P_{lumen} .

The microfluidic devices are connected using 1/16" barb connectors. To be able to connect the microfluidic devices we used injection moulding to fabricate a direct, leak-tight connection between the devices and the barb-connectors (Fig. s2a). The injection-moulds used for this work contained

some defects at the inlet of some channels resulting in the formation of small PDMS membranes (Fig. s2c). Complete removal of these defects was not always successful. In some cases, this membrane remained in place after punching, or the inlet was damaged in such way that leakage occurred when pressure was applied. These defects significantly increased the R_h of the flow path, influencing the WSS. Samples where these defects were present were excluded from flow rate analysis as their dimensions were not fabricated as designed, reducing the total number of samples that could be presented in this study simultaneously.

To determine the range of sample diameters for which the FCB should be optimized, 3D-VoC lumens were patterned with a minimal amount of driving fluid to reach the minimal diameter for the given microfluidic channel. Lumen diameters can be further controlled by varying important parameters like collagen concentration or driving pressure^{32, 44}. The scaffold consists of a 5 mg/ml collagen I hydrogel and was imaged using two-photon-second harmonic generation (2P-SHG) (Fig. 1d). The diameter of collagen scaffolds was measured $202 \mu\text{m} \pm 10 \mu\text{m}$ (mean \pm standard deviation, $n=13$) (Fig. s3) which was expected based on the geometries of the microfluidic channels used ($500 \times 500 \mu\text{m}$) and earlier results^{32, 33}. The diameter ranged between $185\text{--}220 \mu\text{m}$ with an outlier of $244 \mu\text{m}$ (Fig. s3). As observed earlier³³, lumens expanded during the cell seeding step with the diameter measured $240 \mu\text{m} \pm 20 \mu\text{m}$ ($n=16$). The origin of this initial expansion is the unintended injection of air-bubbles, which leads to compaction of the soft hydrogel scaffolds. The luminal diameters of seeded scaffolds ranged from 187 to $290 \mu\text{m}$. The diameters of the lumens produced remained constant over the period of 3 days upon static cell culture with medium being refreshed every 24 hours (Fig. s3). However, depending on the hydrogel scaffolds and cell types used, these luminal diameters might be variable over time^{28, 41}. Furthermore, vessel sprouting during the 3 day culture period under the conditions described was rare, at most occasional small sprouts being observed. Using this observed diameter range, we optimized the FCB for lumen diameters in the range of $180 \mu\text{m}$ to $300 \mu\text{m}$.

Computational modelling of the flow distribution in the FCB

The fluidic circuit of the FCB was designed to: (1) achieve equal pressure difference for all 3D-VoCs and (2) minimize the WSS variation of all samples across a wide range of sample diameters. The fluidic circuit channel dimensions are listed in table s1. To achieve an equal pressure distribution across all samples, the feeder and waste channels were designed to have a minimal R_h . To reduce effects of the length difference between feeder and waste loops, channels widths were adjusted to maintain equal R_h . The crude estimated pressure distribution of the 3D-CAD model was validated using the Computer Fluid Dynamics (CFD)- simulation module of SOLIDWORKS®. This

showed that an equal ΔP can be expected using the designed dimensions across the full length of the channels (Fig. 2a).

To investigate how the WSS of the 3D-VoCs varies within the target diameter range using different R_h of τEQ -resistors, the diameter dependence of WSS was modelled using electrical circuit analogy (Fig. 2b). A common practice in microfluidics is to use high resistance in branching channels to equalize volumetric flow rates^{45, 46}. However, WSS in 3D-VoCs is highly diameter-dependent; when volumetric flow rates are fixed (Eq. s3), a 5-fold difference in WSS can be expected between the minimum and the maximum WSS in the previously mentioned, targeted range (Fig. 2b, red plot).

When a constant ΔP is applied, with a negligible branch resistance, the flow rate is dictated by the R_h of the 3D-VoCs. A linear relationship between the WSS and the diameter is expected (Eq. s11)⁴⁷ which resulted in a 2-fold predicted difference between the minimum and maximum WSS (Fig 2b, green plot, Eq. s3). These plots suggested that there is an optimum R_h where the WSS of the minimum diameter is equal to the WSS of the maximum diameter with the same ΔP . This optimum R_h of the branching channels (sum of the R_h of 3D-VoC and τEQ) can be calculated using Eq. s9. Interestingly, using this optimum R_h the theoretical WSS-difference between the expected minimum and maximum values was reduced to less than 10% across this large diameter range (Fig.2b, blue plot, Eq. s12). The designed dimensions were modelled using 3D-CFD model to validate the WSS equalizing resistance (τEQ -resistance). The 3D-CFD model included the minimum (180 μm), middle (240 μm) and maximum (300 μm) diameters modelled on all fluidic devices, as these diameters would yield the most extreme WSS-values across the diameter range (Fig. 2c and d, video 1). The 3D-CFD simulation corresponded with Eq. s12 (Fig 2b, yellow squares) demonstrating that designed dimensions function as a τEQ -resistor.

Next, this τEQ -resistance functionality was tested to verify a measurable effect. Microfluidic tubing was cut and placed between the pressure sensors and the sample (Fig. s4). A total length of 52 cm was determined using Eq. s10 to match the R_h of the designed τEQ -resistance. Prior to cell seeding, half of the patterned scaffolds were intentionally widened by injecting air bubbles to generate lumens with smaller-(220-240 μm) and larger (280-300 μm) diameters. Samples were individually connected and 3.3 mbar ΔP was applied between the sample and the resistor tubing using the custom software. Flow rate was directly measured using a flow rate sensor, the WSS was calculated using Eq. s3 and compared with the computational model (Fig. 2e). An average WSS of 1 Pa was found ($N=6$), which was as predicted with the Eq. s11 (Fig. 2c, orange plot). A coefficient of variance (CV) of 9.4 % in WSS was observed across the measured 3D-VoCs. Differences between the model and

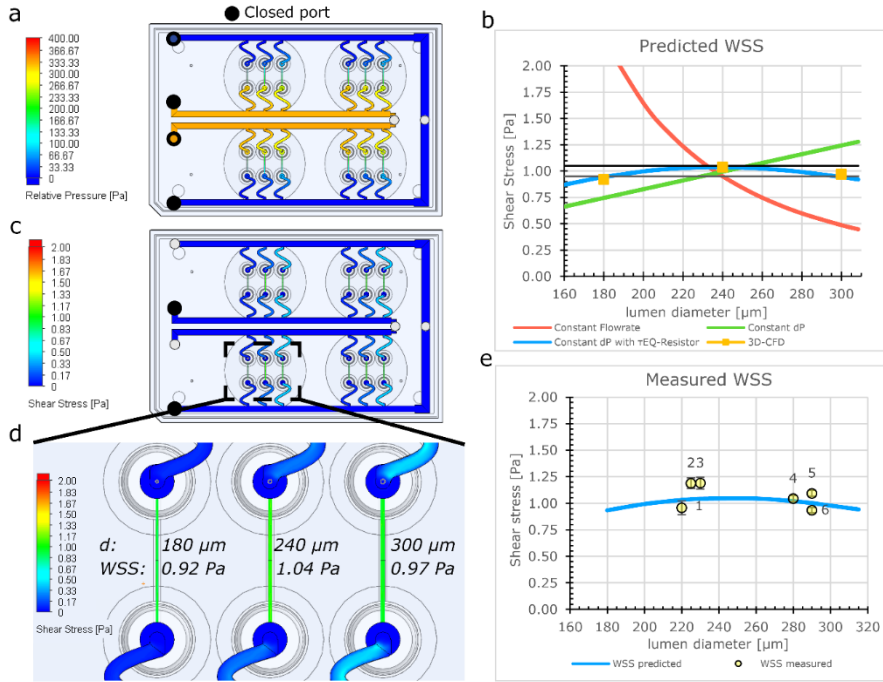


Figure 2: Numerical model of fluidic parameters on a FCB. (a) CFD- simulation of the pressure distribution indicates an equal pressure difference over the feeder channel and waste channel along the full length. (b) Modelling WSS using electrical circuit analogy shows high diameter dependence of WSS to flow rate (red plot), linear relationship with fixed pressure (green plot), parabolic relationship when using τEQ -resistance and a fixed pressure (blue plot). This parabolic behaviour narrows the variation over a wide diameter range to 10 % difference between the minimum and maximum values compared to a 4-fold or 60 % in the other situations. (c) 3D-CFD-simulation of WSS demonstrates that all 3D-VoCs on the fluidic board show similar WSS distribution. (d) Detailed CFD-model of the individual 3D-VoCs having 180 μm (left) 240 μm (middle) and 300 μm (right) shows similar values for WSS across the extremes of diameter. (e) Measured WSS using an optimum τEQ resistor and a ΔP of 3.3 mbar shows a comparable trend as the model value error bars show standard deviation of a 5 second average.

experimental data may be due to interstitial flow or small differences in vertical length of the measured lumen as shown in Fig. s2a. A discrepancy between set- and measured flow rates has been observed earlier³³; however, it was not significantly larger than the accuracy of the set flow rate and therefore we concluded that the interstitial flow cannot explain this difference entirely. The length variation stems from the manual insertion of the pipette tips which can introduce luminal length variation of approximately 1-2 mm (Fig. 1aii). 2 mm difference in length may result in up to 12 % difference in WSS which explains the observed discrepancy. Improving the microfluidic chip design to increase the accuracy of the pipette tip placement could help in reducing this luminal length variation.

Experimental validation of the flow distribution on the FCB

Particle image velocity (PIV) was performed to determine *in situ* the flow distribution of the individual samples connected to the FCB using the workflow

shown in Fig. 3. The luminal diameters were measured using the GFP signal from the beads and ranged from 187 μm to 236 μm (Fig. 3a and c). Perfusion was performed using a ΔP of 0.15 mbar (expected WSS \pm 0.052 Pa). 100 frames were captured at 286 frames per second and analysed using a custom Python script using the OPENPIV library (Fig. 3 b, Fig. s5). Combined with the diameter, the local WSS was calculated using equation Eq. s3 with viscosity of medium containing 2 % serum at 37 °C being 0.79 [mPa s]⁴⁸.

The measured WSS of individual samples had an average of 0.061 Pa and a CV of 12 % (n=6), which was slightly higher than the predicted value (Fig. 3e). However, this could be attributed to the previously mentioned length variation between samples.

A limitation of the presented FCB is the inability to monitor the flow rate of individual 3D-VoCs in real time. PIV is not a practical method for normal experimental settings, as it would require the continuous imaging of 12 samples simultaneously to measure flow rate using highly specialized microscopic settings. By integrating multiple CMOS-chip based flow rate sensors in the branching channels, like the Sensirion LPG10 (Sensirion GmHb), individual flow rates can be logged in real time to improve the experimental quality control throughout long-term perfusion experiments at the expense of increasing the complexity of the system.

Assessment of endothelial cell responses to haemodynamic forces in 3D

To demonstrate the utility of the FCB for biological research we used the FCB to investigate the response of 3D-VoCs to haemodynamic forces in parallel. We first investigated EC-responses to CS induced by application of the intraluminal pressure without flow. Collagen scaffolds without cells were used as a control. First, the expansion of the lumen was investigated in 3D. Collagen scaffolds were imaged with an up-right intravital microscope using 2P-SHG. 3D-VoCs seeded with TUBA1B-mEGFP-hiPSC-ECs cells were imaged using a spinning disk confocal microscope. A gradual increase in the luminal pressure, without application of flow (i.e. same pressure at the inlet and outlet), was used. At different luminal pressure points from P=0 to P=345 mbar with 25 mbar increments 3D stacks were imaged (Fig. s6a and s6b respectively, table s2, video 2 and 3). Manual diameter measurements showed that both the bare scaffolds and seeded scaffolds expanded symmetrically and therefore the total strain caused by the luminal pressure change could be analysed by measuring the diameter-change using a widefield microscope (Fig. 4a,b).

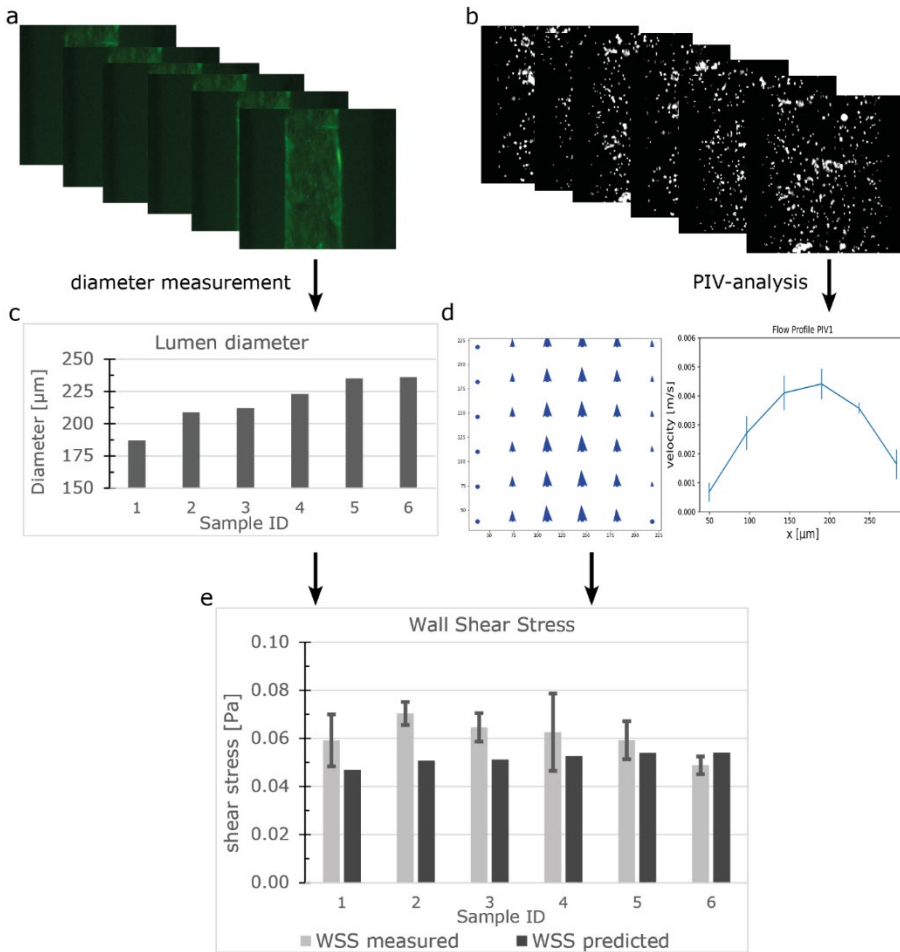


Figure 3: Measuring the Flow distribution and WSS using μPIV . (a) GFP signal from hiPSC-ECs in the lumens was captured using widefield microscopy. (b) Fluorescent beads were perfused and beads displacement was captured with 286 fps. (c) Luminal diameter was measured. (d) Vector fields were constructed using the beads displacements and the maximum velocity was determined at the centre of the lumen. (e) WSS was calculated using the diameter and velocity profile. Error bars show 99 % confidence interval of a vector field.

For this, 3D-VoCs were simultaneously connected to the FCB and imaged using a widefield fluorescent microscope at different luminal pressure points from $P=0$ to $P=345$ mbar with 25 mbar increments. For the collagen scaffolds the middle slice of a 2p-SHG 3D stack was used, as the widefield image of collagen did not have enough contrast to determine the collagen border accurately (Fig s6c). VasoTracker software was used to generate a strain curve of lumens without cells (collagen scaffold, $n=3$) and with cells (3D-VoCs, $n=6$) (Fig. 4c). The strain curve shows that the presence of the EC-monolayer significantly reduced the observed strain compared to the scaffolds without cells. At a pressure of 345 mbar 3D-VoCs exhibited a $5.5 \% \pm 0.8$

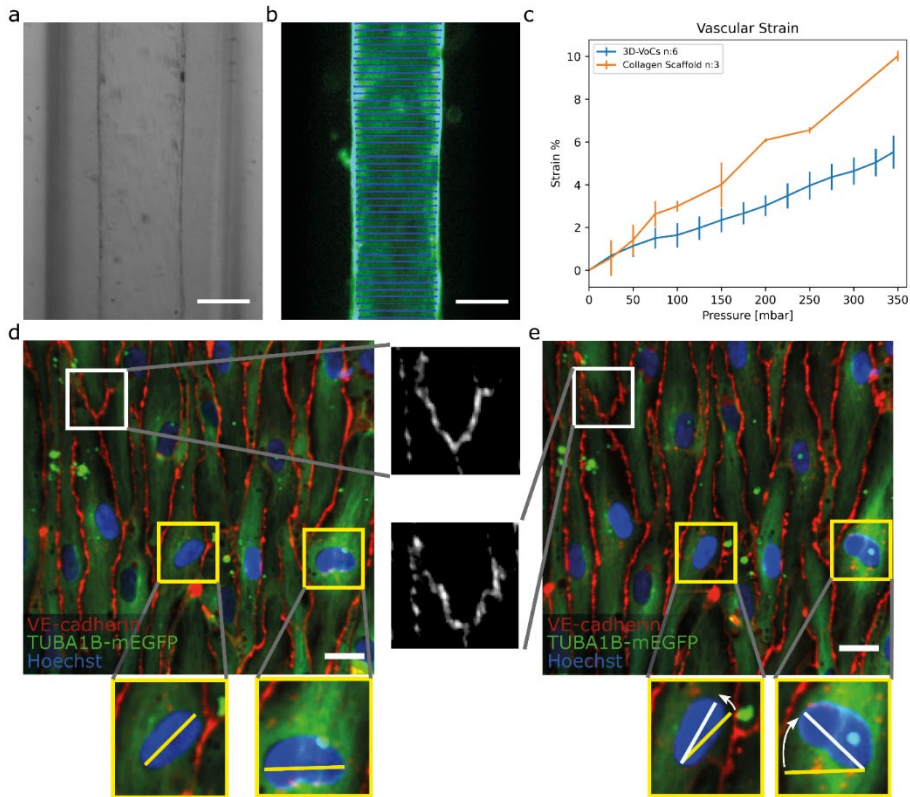


Figure 4: TUBA1B-hiPSC-ECs under circumferential strain. (a) Brightfield image of a 3D-VoCs in a 500 µm wide fluidic channel. (b) GFP-fluorescent signal of a lumen measured using the VasoTracker software (blue lines). (c) Strain curve of the 2p-SHG scaffold only and seeded scaffolds using the widefield fluorescent signal shows a significant effect of the endothelial monolayer, bars are 99% ci. (d) Confocal reconstruction of live TUBA1B-eGFP-ECs (green) co-stained for adherens junctional marker (VE-cadherin, in red) and nuclei (Hoechst, in blue) at pressure=0 mbar, white zoomed panel show continuous adherens junctions and yellow zoomed panels show non-aligned nuclei. (e) Confocal reconstruction of the same region at pressure = 345 mbar shows rapid alignment of unaligned cell nuclei, adherens junctions show the formation of a zig-zag pattern, implying overstretching of the cellular monolayer without rupturing. Scalebar: a,b,150 µm; d, e 20 µm (see also videos 5-8 for the animated videos).

strain while for scaffold-only conditions, this was 11 % \pm 1.3. It is important to note that walls of the PDMS-channel under both conditions also expand in the measured pressure range, contributing to the total measured compliance (Fig s6c, video 4-6).

The hiPSC-EC monolayers under CS were investigated in greater detail using spinning-disk confocal microscopy. Cells were cultured for 72 hours under static conditions and live TUBA1B-mGFP-ECs were co-stained for VE-cadherin to visualize the cell junctions and Hoechst to visualize the nuclei. The 3D-VoCs were connected to the FCB and imaged while the pressure of the inlet and outlets was simultaneously increased in a stepwise manner up to 345 mbar, avoiding net fluid flow. Due to photobleaching of the VE-cadherin

conjugated fluorophore, it was not possible to image more than 4 frames per region. These sequences showed that VE-cadherin junctions retained their orientation up to 100 mbar of internal pressure (Video s7). At 150 mbar of luminal pressure (strain of approximately 2%), adherens junctions adopted a zig-zag pattern, indicating overstretching of the EC-monolayer and partial opening of the cell-cell junctions (Fig. 4d and e white inserts, video s8). Nevertheless, the hiPSC-EC monolayer remained intact up to the maximum measured internal pressure of 345 mbar. Interestingly, non-aligned cell nuclei quickly aligned with the longitudinal axis of the lumen despite the lack of continuous flow (Fig. 4d and e yellow inserts). The tortuosity index of cell junctions was next calculated by dividing the length of the cell borders (L_b) by the Euclidean distance (L_e) length⁴⁹. We found that the tortuosity index of adherens junctions was significantly higher under pressure of 345 mbar when compared to 0 mbar pressure (tortuosity index: 1.06 ± 0.021 vs 1.09 ± 0.048 , $P < 0.001$) (Fig. s7). When the pressure is released, most junctions return to a more straight morphology, however some dislocated junctions remained present (Fig. s9). These findings suggested that the EC monolayer cannot stretch to the same extent as in vivo²⁵. However, it has been shown that pre-conditioning of cells to strain for longer periods can result in higher compliance of EC-monolayers⁵⁰. These zig-zag patterns could influence the permeability of the endothelium; however it has been shown that continuous exposure to circumferential strain decreases the permeability^{51, 52}. Further detailed investigation on how this circumferential stress influences the endothelial monolayer now be carried out using this FCB.

To investigate the cellular response to WSS, cells were exposed to a ΔP of 100 Pa (generating a predicted WSS of 0.3 Pa) with an internal pressure of 50 mbar (approximately 1% of strain) for 24 hours. A well-characterized response of ECs to WSS is the reorganization of the actin cytoskeleton^{53, 54}. A venous-like WSS of 0.3 Pa (3 dyne/cm²) has been shown to alter actin morphology of primary venous-ECs significantly^{29, 55, 56}. By forming actin stress fibres, the ECs can react to haemodynamic forces. We used 3D-CFD simulation to confirm the ability of the FCB design to generate equal WSS for the given samples under the applied conditions (P_{lumen} : 50 mbar, ΔP : 1 mbar) (Fig. s10a and d blue plot). We also examined the samples under higher pressure to confirm that the resulting WSS is constant regardless of applied pressure (Fig. s10b and d, gray plot). We found that, given the luminal dimension and perfusion parameters measured, the hiPSC-ECs experienced 0.32 Pa with a CV of 4%. If all sample had been perfused using a single flowrate, the CV would have been 23% between samples (Eq. s3).

The lumens were kept for 48 hours in static conditions to promote cell attachment and were then perfused for 24 hours. The 48 hours static- and 24 hours perfusion experiments were compared with 72 hours static. The cells were fixed, permeabilized and stained for F-actin using a phalloidin-

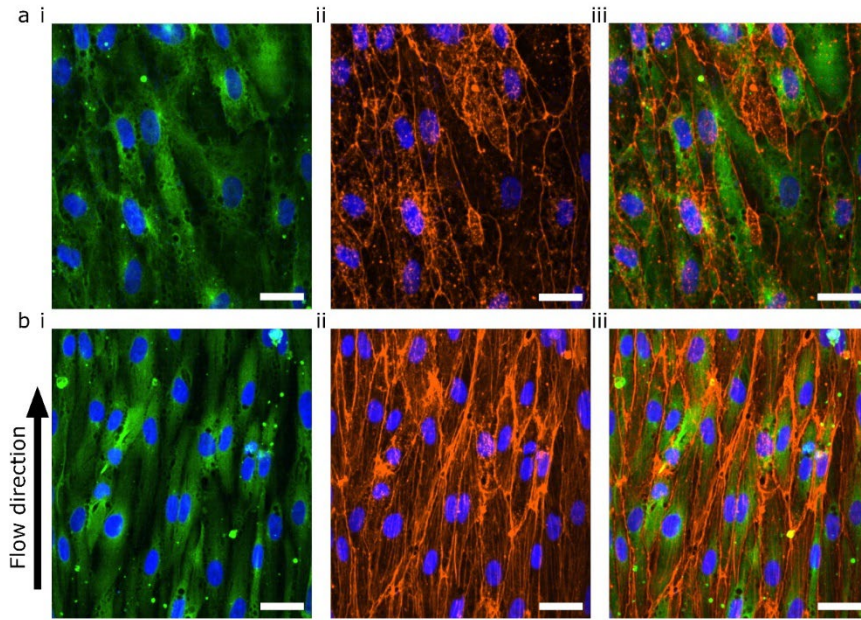


Figure 5: Confocal microscopy of TUBA1B-hiPSC-ECs under WSS. (a) hiPSC-ECs cultured in static conditions for 72 hours. (b) hiPSC-ECs cultured in static conditions for 48 hours and 24 hours under 0.3 Pa WSS. Representative images of 7 individual lumens are shown with (i) TUBA1B-eGFP-ECs (green) co-stained for (ii) F-actin (orange) and (iii) merged image. Nuclei are visualized with DAPI (blue) in all images. Scale bars 30 μm .

conjugated fluorophore (Fig. 5). Both flow and no flow conditions were imaged using the same microscope settings and displayed using the same LUT. In the absence of flow, the F-actin was mainly located at the cortical rim and the overall intensity was low (Fig. 5a). As previously shown, hiPSC-ECs cultured under static conditions in 3D-VoCs showed alignment with the longitudinal axis of the lumen³³. On the other hand, 3D-VoCs connected to the FCB without constrictions ($n=7$) showed both the formation of the actin stress fibres and increased overall intensity, demonstrating that the hiPSC-ECs were able to react to the applied flow much like primary ECs (Fig. 5b)^{55, 56}. We chose to use F-actin as a proof-of-principle in this study. Additional characterization of morphological changes to WSS, such as investigation of EC polarity would be an alternative to quantify adaptation to WSS in this model⁵⁷.

During perfusion experiments, we often observed delamination of the collagen scaffolds from the PDMS channel walls when using the PDMS surface-coating protocol previously reported³³. We hypothesised that this could be due to the sub-optimal coating procedure, as white residue was often observed after coating. We therefore altered the APTES coating procedure by using a low concentration of APTES in methanol⁵⁸. This optimized protocol resulted in higher bonding of the ECM to the PDMS, so that it could withstand pressures of over 1000 mbar without delamination (Fig s5c, Video s2).

4.4 Conclusion

Overall, the results presented here demonstrate the ability of the perfusion platform we designed to exert bi-modal mechanical stimulation of up to twelve 3D-VoCs with WSS combined with CS. Due to the fluidic circuit design, the variation in WSS resulting from different 3D-VoCs diameters is minimized, eliminating the need for individual sample control and increasing throughput. To our knowledge, this is the first multiplexed, controlled perfusion system for 3D-VoCs. Combination with a scalable method for generating 3D-VoCs allowed the number of 3D-VoC replicates in a single perfusion experiment to be increased. The FCB we designed is capable of individually controlling WSS and internal pressure using two pressure controllers, while being able to recirculate cell culture medium.

Using this FCB, we demonstrated morphological changes in hiPSC-ECs to both WSS and CS separately, illustrating the need to include and control both stimuli in *in vitro* experiments. Future studies could include a thorough structural and functional analysis the response hiPSC-ECs to both WSS, CS and a combination in physiological and pathophysiological conditions.

We expect that the flexibility of FCBs will help the development of advanced *organ-on-chip* technology with more predictive capabilities³⁷⁻³⁹. The concept of the FCB presented here allows the number of technical replicates under perfusion to be increased which is important for the development of more complex models. This simple design can be further combined with more advanced concepts to fabricate better and easier to use perfusion platforms.

Author contributions

Conceptualization: MNSdG, VVO; Data curation: MNSdG; Formal Analysis: MNSdG, AV; Funding acquisition: AvdB, ADvdM, CLM, VVO; Investigation: MNSdG; Methodology: MNSdG, AV, DGK, FEvdH; Project administration: VVO; Resources: ADvdM, VVO; Software: MNSdG; Supervision: CLM, VVO; Validation: MNSdG; Visualization: MNSdG, AV; Writing – original draft: MNSdG, VVO; Writing – review & editing: All Authors.

Conflict of interest

The authors declare no conflict of interest.

Acknowledgements

The authors would like to thank Sander van Berloo of the department from Medical Technology LUMC for the design and fabrication of the PCBs and MCU used for this work; the Allen Cell Collection, available from Coriell Institute for Medical Research, for providing materials. This work was supported by the Netherlands Organ-on-Chip Initiative (NOCI), an NWO Gravitation project (024.003.001) funded by the Ministry of Education, Culture and Science of the government of the Netherlands and the European Research Council (ERC) under the Advanced Grant 'VESCEL' Program (grant no. 669768).

4.5 Materials and Methods

Fabrication of the Fluidic Circuit Board

The FCB was designed in SolidWorks® and composed of two cast 10 mm and one 15 mm polymethylmethacrylate (PMMA) plates (Altuglass). All connecting channels and fittings for Luer-slip connectors were milled with a CNC micro mill (Datron Neo, Datron AG). After milling, The FCB was assembled as previously described³⁹. Briefly, both layers of the FCB were thoroughly cleaned using industrial cleaning wipes (Adolf Würth GmbH & Co), deionized water, absolute ethanol (Sigma-Aldrich), and Propanol (Sigma-Aldrich). A solution of acetone (Sigma-Aldrich) in absolute ethanol at a volume ratio of 1:10 was added on top of the connection layer slab and the complementary channel layer slab was then pressed onto the connection layer slab and aligned using pins (DIN 7 - ISO 2338). The assembled FCB was subsequently pressed at 1 kN at 55 °C using a hydraulic press (model 3889, Carver Inc.). Connection between the microfluidic devices and FCB was achieved by inserting barb connectors (male luer-to-barb 1/16", IDEX) at the appropriate location (Fig. 1b).

The FCB was tested with off-board medium reservoirs, check-valves and flow sensors to reduce fabrication steps (Fig. 1f). A full list of components required is shown in table 1. Two 15 mL falcon tubes were used as reservoirs, using 4-port pressure caps (Elveflow). Four check-valves with low cracking pressure (12 mbar, Masterflex) were connected to the FCB. Low-resistance polytetrafluoroethylene-tubing (PTFE, ID 800 µm) was used to connect all external fluidic components. For long-term cell culture, an alternative circuit is used with the same principle using a single flow sensor (Fig. s1). Gauge pressure sensors (Honeywell, MPR-0300YG) were used to measure the pressure difference at the FCB and the reservoir liquid level. Sensors were directly inserted on the FCB at the designated locations (Fig. 1c). Pressure sensors were inserted remotely in the Falcon tubes using a piece of tubing. All pressure sensors were connected using ribbon wires to a Micro control unit and connected to the controlling computer using USB. A custom Python-based PID-controller was developed to control two 345 mbar LineUp EZ-flow (Fluigent) pneumatic pressure controllers³⁵.

3D Computer Fluidic Dynamics (CFD) simulation

The WSS characterization was run in SolidWorks Flow Simulation module (Dassault Systèmes, France), using a viscosity of 0.79 [mPa s], with no gravity and with no slip condition. For this simulation we assumed no interstitial flow. Two simulations were run to characterize the WSS and pressure distribution. First, a simulation including the entire domain of the FCB was carried out. From this simulation, the relative pressure at the inlets of the 3D-VoCs were determined. These pressures were used as input for the second simulation where only the lumens of the 3D-VoC were considered.

Chapter four

Table 1: List of components

Electronic Component	Qty.	Manufacturer	Product SKU:
Flow EZ-line Up 345 mbar	2	Fluigent	LU-FEZ-345
Link-up module	1	Fluigent	LU-LNK-0002
Flow sensor L	1 or 2	Fluigent	FLU-L-D-FDG
Pressure sensors	4 or 6	Honeywell	MPRLS0300YG0001B
Pressure sensor printed circuit board (PCB)	1	Custom	
MCU	1	Custom	
Optional:			
Pressure source 1.2 bar	1	Fluigent	FLPG005
Fluidic Component			
Microfluidic Reservoir for 15 mL Falcon Tube-S (4 port)	2	ELVEFLOW	LVF-KPT-S-4
15 ml reservoirs	2	Greiner-Bio one	
Check valves	4	Master flex	MF-30505-92
Luer-male to 1/16 barb	24	IDEX	CIL-P-854
¼-28-Female to Male Luer Adapter	4	IDEX	CIL-P-655-01
¼-28-Female to Female Luer Lock Adapter	4	IDEX	CIL-P-678
PTFE Tubing – 1/16" OD X 1/32" ID*		ELVEFLOW	LVF-KTU-15
Female luer Bulkhead 1/4-28 Thread, to 1/16" Hose Barb	2	Cole-Parmer	45508-30
Optional:			
3-port valve	2	Masterflex	HV-30600-41
Y-connectors	2	IDEX	CIL-P-512

This strategy enabled an increased mesh density for the simulation and determination of an expected WSS among the different lumen diameters considered.

Fabrication of microfluidic devices

Microfluidic devices were fabricated from polydimethylsiloxane (PDMS, Sylgard 184, Dow Corning) using injection moulding, as opposed to conventional soft lithography methods^{59, 60}. Injection moulding allows the imprinting of media reservoirs, which act as leak-tight connections to the FCB using standardized barb connectors (Fig. s2a). The microfluidic devices have the same dimensions as standard 35 mm Petri dishes, allowing easy handling and connecting to the FCB. Injection-moulds for the microfluidic devices were designed in SolidWorks and fabricated in PMMA using micro milling. Dimensions of flow channels were as previously described³³ (1.1 cm × 500 µm × 500 µm; l × w × h, Fig. s2a). The procedure is shown in Fig. s2b.

PDMS and base agent were mixed 10:1 (w:w) with curing agent and degassed at room temperature. The degassed PDMS was transferred to a syringe. Prepared syringes were kept at -20 °C until use for up to 3 months. The PDMS was allowed to warm to room temperature before injection. The injection mould was assembled using six neodymium block magnets (N42, 1.3T, approximately 60 N per magnet, Webcraft GmbH) and the PDMS was slowly injected (Fig. s2b (2)). The filled injection-mould was set vertically at room temperature (19-22 °C) overnight for the initial crosslinking to minimize shrinkage. Afterwards, the PDMS was further cured at 75 °C for 60 minutes. The PDMS was carefully peeled off and excess PDMS was cut off. Post-production examination of microfluidic devices showed a small number of devices with inlet defects and these devices were subsequently discarded or removed from analyses (Fig. s2c).

The assembly of the microfluidic devices was carried out as previously described with modifications³³. PDMS devices and round cover glasses (#1.5, ø 30 mm Thermo scientific) were surface-activated using air plasma (45 sec, 50 Watt at 60 Pa, CUTE-Femto Science) and contact bonded using light pressure. Immediately after contact bonding, microfluidic channels were functionalized to covalently bind collagen I. First, a 0.1 % (v/v) 3-Aminopropyl-triethoxysilane (APTES, Sigma-Aldrich), 0.005 % distilled water (Gibco®) was prepared in methanol (Technical grade, Sigma-Aldrich), injected in the channels and incubated for 30 minutes at RT⁵⁸. Channels were thoroughly rinsed with methanol and dried using a nitrogen-gas flow. Subsequently, the devices were incubated at 110 °C for 30 min on a hotplate. Next, channels were injected with 5 % (v/v) Glutaraldehyde (Sigma-Aldrich, in distilled water) and incubated at RT for 30 minutes. Channels were thoroughly rinsed with distilled water, dried under nitrogen gas flow and baked at 75 °C for at least 2 hours.

Lumen patterning using Viscous Finger Patterning

Collagen scaffolds were generated as previously described with a minor modification³³. Briefly, the 7 mm tip ends of P10 pipette tips (Greiner Bio-One #741015) were used as a driving tip and intact tips as “receiving” tips for patterning (Fig. 1a_{ii}). The collagen I hydrogel was prepared as follows: (1) reconstitution buffer was prepared using M199 medium 10X (Gibco®), 4-(2-hydroxyethyl)-1-piperazineethanesulfonic acid -buffer (HEPES, ThermoFisher, final concentration 10 %), Sodium bicarbonate (ThermoFisher, final concentration 2.2 g/L), distilled water and 1 M sodium hydroxide according to the manufacturer’s instructions; (2) Collagen I high concentration (Corning, cat# 354249, 11.0 mg/ml) was aliquoted and the quantity was verified using weight; (3) the reconstitution buffer was added to the collagen I stock to achieve the final concentration of 5 mg/ml; the solution was thoroughly mixed, centrifuged to remove air bubbles and transferred to a 1 ml syringe (BD Luer-Lok™). The collagen I mixture was sequentially injected via the receiving tip using a plastic blunt needle (Techcon, 20G) until the meniscus of the collagen I mixture reached the outlet of the driving tip. Subsequently, 3.5 µl of PBS was pipetted on top of the collagen in driving tip to initiate patterning using a multi-dispensing pipet. Immediately after lumen patterning, microfluidic devices were incubated for 30 minutes at 37 °C in a humidified incubator. After collagen gelation, Endothelial Growth Medium-2 (EGM-2, Promocell) supplemented with Penicillin-Streptomycin (PenStrep, Thermofisher, final concentration 25 Units/ml), was pipetted in the receiving tip and devices were further incubated overnight at 37 °C. Prior to cell seeding, the driving and receiving tips were removed in a smooth twisting motion.

Differentiation and expansion of hiPSC-ECs

Alpha-tubulin- monomeric Enhanced Green Fluorescent Protein-hiPSCs (TUBA1B-mEGFP, Cell Line ID: AICS-0012 cl.105, <https://hpscereg.eu/cell-line/UCSFi001-A-2>) were obtained from the Allen institute⁶¹. hiPSC-ECs were differentiated as previously described⁶². Briefly, TUBA1B-mEGFP-hiPSCs were maintained in TeSR™-E8™ medium on vitronectin-coated 6-well plates and seeded at day (-1). Twenty-four hours after seeding, E8 medium was replaced with B(P)EL medium supplemented with 8 µM CHIR. On day 3, the medium was replaced with B(P)EL medium supplemented with 50 ng/ml VEGF (R&D systems) and 10 µM SB431542 (Tocris Bioscience); cells were refreshed with the same medium on days 7 and 9. hiPSC-ECs were isolated on day 10 using CD31-Dynabeads™ (Invitrogen), expanded for 3 days and cryopreserved. hiPSC-ECs from cryo-preserved batches were used in all experiments. They were thawed and expanded in Endothelial Cell-Serum Free Medium (EC-SFM, Gibco, cat. No. 11111-044) supplemented with 1 % human platelet poor serum, FGF2 (20 ng/mL) and VEGF (30 ng/mL), on a 0.1 % gelatine-coated T-75 culture flask. hiPSC-ECs used in 3D cell cultures were at passage 2.

Seeding of collagen scaffolds with hiPSC-ECs

HiPSC-ECs were harvested using TrypLE™ (Thermo Fisher), and resuspended at a concentration of 15×10^6 cells/ml in EGM-2 supplemented with 50 ng/mL VEGF and PenStrep. 5 μ l of cell suspension was injected using a multi-dispensing pipette with a maximum flow rate of 100 μ l/min. After injection, microfluidic devices were placed on a slow rotator (1 RPM, channel longitudinal axis in line with rotating axis) and rotated for 1 to 2 hours at 37 °C until all cells were attached and completely covered the collagen scaffold. Medium was refreshed and samples were placed inside a humidifier-box to prevent medium evaporation and incubated at 37 °C, 5 % CO₂. Medium was refreshed every 24 hours with EGM-2.

Measurement of τ EQ-functionality

Samples were prepared as described above and individually connected to the fluidic pump using a total 52 cm of microfluidic tubing divided over two tubes (Fig. s4, ID 800 μ m). The pressure difference was controlled using the custom PID-software⁴⁰ and the flow rate measured using a flow rate sensor (Fluigent, size L). Flow rate was allowed to stabilize and a 5 second average was used as the measured value. The 3D-VoC diameter was determined using widefield microscope and the WSS was calculated using Eq. s3 and compared to the theoretical value (Eq. 1).

Particle image velocity (PIV)

Cell culture medium was supplemented with 25×10^6 fluorescent beads/ml (Thermo Fisher, 1 μ m). Bead displacement was captured using a Leica DMI6000 equipped with a Zyla 4.2 sCMOS and a 10x objective. Maximum framerate of 286 frames per second was achieved using binning of 3x3. PIV was performed using a custom script using the OPENPIV library⁶³. The following settings were used to analyse all frames: binary threshold: 100; interrogation window: 24 px; search window: 48 px; overlap: 12 px. All vector fields were combined and filtered based on median of the location to improve accuracy. Using the maximum velocity in the centre of the lumen the average velocity was calculated assuming Poiseuille flow to calculate the flowrate with Eq. s3.

Assessment of 3D scaffold and lumen expansion

Unseeded collagen scaffolds were individually connected to the fluidic perfusion system and placed upside down on an upright ZEIS LSM710 NLO microscope equipped with a multi-photon laser tuned at 810 nm. Two-photon second harmonic generation (2P-SHG) images were acquired using a non-descanned detector at 380-430 nm. Internal pressure was controlled using the pressure pumps with no flow (i.e. no pressure difference). Pressure was varied between 0 mbar and 345 mbar. At every pressure step, a 3D stack of images of the lumen was taken.

Scaffolds were seeded with TUBA1B-mEGFP-ECs, and imaged using a Leica DMI8 microscope equipped with a Dragonfly® spinning disk (pinhole:40 µm) (Andor). A HC PL APO 20x/0.75 IMM CORR CS2 objective was used with water as immersion medium. Pressure was varied between 0 mbar and 345 mbar. At every pressure step a 3D stack of images of the lumen was taken.

Measurement of collagen I scaffold compliance

Diameter expansion was determined in pixels at the widest slice of the 3D-2p-SHG stack using VasoTracker software using the average of 50 lines across the field of view⁶⁴. The strain was calculated using Eq. 2:

$$strain = \frac{pix_p - pix_0}{pix_0} * 100\% \quad \text{Eq. 2}$$

Where pix_p : measured pixel length at pressure P, pix_0 pixel length at P=0.

Measurement of 3D-VoC compliance

3D-VoCs were connected to the FCB and placed on an EVOS widefield microscope. The GFP signal of the TUBA1B-mEGFP was captured at every pressure step with the centre of the lumen in focus. Diameter expansion was determined in pixels using VasoTracker software using the average of 50 lines across the field of view. Vascular compliance was calculated using Eq. 2.

Live-cell imaging of 3D-VoCs

Prior to imaging, 10 µl of EGM-2 with anti-VE-cadherin (CD144-mouse anti-Human Alexa-647, BD Bioscience, diluted 1:200) and Hoechst—33342 (Thermo Scientific, 1 µg /ml) were injected into the lumen of 3D-VoCs and incubated for 30 min at 37 °C. Next, 3D-VoCs were connected to the FCB and flushed with fresh medium. Samples were imaged using Leica DMI8 microscope equipped with a Dragonfly® spinning disk (pinhole:40 µm) (Andor). A HC PL APO 20x/0.75 IMM CORR CS2 objective was used with water as immersion medium. This objective was combined with 2x camera magnification to enhance lateral resolution. An iXon CCD camera was used to record the signal.

Long-term recirculation

3D-VoCs were prepared as described above and cultured under static conditions for 48 hours. The FCB was primed with EGM-2 + PenStrep and the 3D-VoCs were connected. The air compressor was placed inside of a dry incubator (5 % CO₂) and the 3D-VoCs were perfused using a pressure difference of 1 mbar and 50 mbar of P_{FCB} for 24 hours using the custom PID-software⁴⁰.

Immunofluorescence staining of 3D-VoCs

4 % paraformaldehyde (PFA) solution was injected into the lumen of 3D-VoCs and incubated for 15 minutes at RT. Cells were subsequently permeabilised using 0.5 % (v/v) Triton-X 100 in PBS (without Ca²⁺ and Mg²⁺) for 10 minutes at RT. Samples were blocked with 2 % BSA in PBS (without Ca²⁺ and Mg²⁺)

(w/v) for 30 minutes at RT. Alexa Fluor™ 647 Phalloidin (Thermo fisher, final concentration 165 nM) was diluted in 1 % BSA in PBS and 10 μ l was injected into the channels. Channels were incubated at RT for 1 hour and washed three times with PBS (without Ca^{2+} and Mg^{2+}) for 10 minutes. Cell nuclei were stained using 4',6-diamidino-2-phenylindole (DAPI, 300 nM, Thermo fisher) for 10 minutes at RT. Samples were stored in the dark at 4 °C until imaging using a Dragonfly® spinning disk (pinhole size:40 μ m, Andor).

Quantification of cell junctions

The tortuosity index was calculated to quantify cell junctions^{49, 65}. First, the VE-cadherin images acquired at low pressure (0 mbar) and high pressure (345 mbar) were set at threshold and "skeletonized" to visualize cell-cell junctions. The resulting skeletonized images were analyzed using the AnalyzeSkeleton plugin⁶⁵. The length of cell borders (Lb) divided by the branch length (Euclidean distance) (Le) gives the tortuosity index. Cell border lengths greater than 10 μ m were included in analysis.

Statistics

Statistical analysis was performed using Microsoft office Excel Analysis-ToolPak.

For the scaffold compliance analysis, a Student's t-test assuming unequal variances was used. Results are presented as mean \pm 99% Confidence interval.

For the tortuosity index analysis, a Student's t-test assuming equal variances was used. Results are presented as mean \pm standard deviation.

A coefficient of variance (CV) was calculated with the following equation: standard deviation/mean to quantify the variation.

References

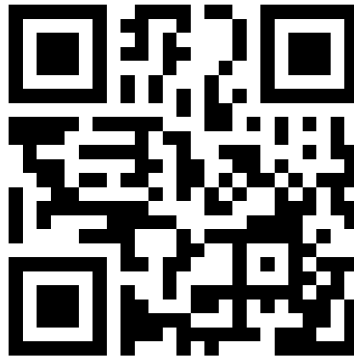
1. A. Jambusaria, Z. Hong, L. Zhang, S. Srivastava, A. Jana, P. T. Toth, Y. Dai, A. B. Malik and J. Rehman, *Elife*, 2020, **9**.
2. M. Reiterer and C. M. Branco, *Febs J*, 2020, **287**, 1088-1100.
3. K. C. Wang, Y. T. Yeh, P. Nguyen, E. Limqueco, J. Lopez, S. Thorossian, K. L. Guan, Y. J. Li and S. Chien, *Proc Natl Acad Sci U S A*, 2016, **113**, 11525-11530.
4. D. L. Sheinberg, D. J. McCarthy, O. Elwardany, J. P. Bryant, E. Luther, S. H. Chen, J. W. Thompson and R. M. Starke, *Neurosurg Focus*, 2019, **47**, E3.
5. J. Joffre, J. Hellman, C. Ince and H. Ait-Oufella, *Am J Respir Crit Care Med*, 2020, **202**, 361-370.
6. A. Cochrane, H. J. Albers, R. Passier, C. L. Mummery, A. van den Berg, V. V. Orlova and A. D. van der Meer, *Adv Drug Deliv Rev*, 2019, **140**, 68-77.
7. S. R. Moses, J. J. Adorno, A. F. Palmer and J. W. Song, *Am J Physiol Cell Physiol*, 2021, **320**, C92-C105.
8. M. Sweeney and G. Foldes, *Front Cardiovasc Med*, 2018, **5**, 154.
9. K. Gaengel, G. Genove, A. Armulik and C. Betsholtz, *Arterioscler Thromb Vasc Biol*, 2009, **29**, 630-638.
10. W. C. Aird, *Circ Res*, 2007, **100**, 174-190.
11. W. A. Muller, *Trends Immunol*, 2003, **24**, 327-334.
12. W. A. Muller, *Lab Invest*, 2002, **82**, 521-533.
13. W. C. Aird, *Cold Spring Harb Perspect Med*, 2012, **2**, a006429.
14. W. C. Aird, *J Thromb Haemost*, 2005, **3**, 1392-1406.
15. S. Pradhan, O. A. Banda, C. J. Farino, J. L. Sperduto, K. A. Keller, R. Taitano and J. H. Slater, *Adv Healthc Mater*, 2020, **9**, e1901255.
16. R. Amaya, A. Pierides and J. M. Tarbell, *Plos One*, 2015, **10**, e0129952.
17. E. Roux, P. Bougaran, P. Dufourcq and T. Couffignal, *Front Physiol*, 2020, **11**, 861.
18. S. Baratchi, K. Khoshmanesh, O. L. Woodman, S. Potocnik, K. Peter and P. McIntyre, *Trends Mol Med*, 2017, **23**, 850-868.
19. Y. Qiu and J. M. Tarbell, *J Vasc Res*, 2000, **37**, 147-157.
20. Y. B. Arik, W. Buijsman, J. Loessberg-Zahl, C. Cuartas-Velez, C. Veenstra, S. Logtenberg, A. M. Grobink, P. Bergveld, G. Gagliardi, A. I. den Hollander, N. Bosschaart, A. van den Berg, R. Passier and A. D. van der Meer, *Lab Chip*, 2021, **21**, 272-283.
21. S. Lehoux, B. Esposito, R. Merval and A. Tedgui, *Circulation*, 2005, **111**, 643-649.
22. M. Namba, T. Matsuo, F. Shiraga and H. Ohtsuki, *Ophthalmic Res*, 2001, **33**, 163-169.
23. M. Haga, A. Chen, D. Gortler, A. Dardik and B. E. Sumpio, *Endothelium-J Endoth*, 2003, **10**, 149-157.
24. X. M. Liu, D. Ensenat, H. Wang, A. I. Schafer and W. Durante, *Febs Lett*, 2003, **541**, 52-56.
25. P. M. Cummins, N. von Offenberger Sweeney, M. T. Killeen, Y. A. Birney, E. M. Redmond and P. A. Cahill, *Am J Physiol Heart Circ Physiol*, 2007, **292**, H28-42.
26. W. F. Hynes, M. Peponis, C. Robertson, J. Alvarado, K. Dubbin, M. Triplett, J. J. Adorno, A. Randles and M. L. Moya, *Sci Adv*, 2020, **6**, eabb3308.
27. D. B. Kolesky, R. L. Truby, A. S. Gladman, T. A. Busbee, K. A. Homan and J. A. Lewis, *Adv Mater*, 2014, **26**, 3124-3130.
28. J. A. Jimenez-Torres, S. L. Peery, K. E. Sung and D. J. Beebe, *Adv Healthc Mater*, 2016, **5**, 198-204.
29. W. J. Polacheck, M. L. Kutys, J. B. Tefft and C. S. Chen, *Nat Protoc*, 2019, **14**, 1425-1454.
30. G. Adriani, D. Ma, A. Pavesi, R. D. Kamm and E. L. Goh, *Lab Chip*, 2017, **17**, 448-459.
31. M. Vila Cuenca, A. Cochrane, F. E. van den Hil, A. A. F. de Vries, S. A. J. Lesnik Oberstein, C. L. Mummery and V. V. Orlova, *Stem Cell Rep*, 2021, **16**, 2159-2168.
32. A. Herland, A. D. van der Meer, E. A. Fitzgerald, T. E. Park, J. J. Sleeboom and D. E. Ingber, *Plos One*, 2016, **11**, e0150360.
33. M. N. S. de Graaf, A. Cochrane, F. E. van den Hil, W. Buijsman, A. D. van der Meer, A. van den Berg, C. L. Mummery and V. V. Orlova, *APL Bioeng*, 2019, **3**, 026105.
34. A. C. I. van Steen, L. Kempers, R. Schoppmeyer, M. Blokker, D. J. Beebe, M. A. Nolte and J. D. van Buul, *J Cell Sci*, 2021, **134**.
35. M. N. S. de Graaf, PID-controller for microfluidic flow, <https://github.com/mnsdegraaf/mfcb>, (accessed 08-08-2022, 2022).
36. C. A. Dessalles, C. Ramon-Lozano, A. Babataheri and A. I. Barakat, *Biofabrication*, 2021, **14**.
37. A. R. Vollertsen, A. Vivas, B. van Meer, A. van den Berg, M. Odijk and A. D. van der Meer, *Biomicrofluidics*, 2021, **15**, 051301.

38. A. R. Vollertsen, D. de Boer, S. Dekker, B. A. M. Wesselink, R. Haverkate, H. S. Rho, R. J. Boom, M. Skolimowski, M. Blom, R. Passier, A. van den Berg, A. D. van der Meer and M. Odijk, *Microsyst Nanoeng*, 2020, **6**, 107.
39. A. Vivas, A. van den Berg, R. Passier, M. Odijk and A. D. van der Meer, *Lab Chip*, 2022, **22**, 1231-1243.
40. M. N. S. de Graaf, A. Vivas, A. D. van der Meer, C. L. Mummery and V. V. Orlova, *Micromachines (Basel)*, 2022, **13**, 1359.
41. K. M. Chrobak, D. R. Potter and J. Tien, *Microvasc Res*, 2006, **71**, 185-196.
42. K. W. Oh, K. Lee, B. Ahn and E. P. Furlani, *Lab Chip*, 2012, **12**, 515-545.
43. J. H. Sung, Y. I. Wang, N. Narasimhan Sriram, M. Jackson, C. Long, J. J. Hickman and M. L. Shuler, *Anal Chem*, 2019, **91**, 330-351.
44. L. L. Bischel, S. H. Lee and D. J. Beebe, *J Lab Autom*, 2012, **17**, 96-103.
45. S. Kou, L. Pan, D. van Noort, G. Meng, X. Wu, H. Sun, J. Xu and I. Lee, *Biochem Biophys Res Commun*, 2011, **408**, 350-355.
46. S. Sugiura, K. Hattori and T. Kanamori, *Anal Chem*, 2010, **82**, 8278-8282.
47. Y. I. Cho and D. J. Cho, *Korean Circ J*, 2011, **41**, 287-295.
48. C. Poon, *J Mech Behav Biomed Mater*, 2022, **126**, 105024.
49. S. Tokuda, T. Higashi and M. Furuse, *Plos One*, 2014, **9**, e104994.
50. V. P. Shirinsky, A. S. Antonov, K. G. Birukov, A. V. Sobolevsky, Y. A. Romanov, N. V. Kabaeva, G. N. Antonova and V. N. Smirnov, *J Cell Biol*, 1989, **109**, 331-339.
51. S. Zeinali, E. K. Thompson, H. Gerhardt, T. Geiser and O. T. Guenat, *APL Bioeng*, 2021, **5**, 026102.
52. N. T. Collins, P. M. Cummins, O. C. Colgan, G. Ferguson, Y. A. Birney, R. P. Murphy, G. Meade and P. A. Cahill, *Arterioscler Thromb Vasc Biol*, 2006, **26**, 62-68.
53. S. Morel, S. Schilling, M. R. Diabougua, M. Delucchi, M. L. Bochaton-Piallat, S. Lemeille, S. Hirsch and B. R. Kwak, *Front Physiol*, 2021, **12**, 727338.
54. B. L. Langille, *Microcirculation*, 2001, **8**, 195-206.
55. D. van Geemen, M. W. Smeets, A. M. van Stalborch, L. A. Woerdeman, M. J. Daemen, P. L. Hordijk and S. Huveneers, *Arterioscler Thromb Vasc Biol*, 2014, **34**, 2059-2067.
56. S. Zhao, A. Suciu, T. Ziegler, J. E. Moore, Jr., E. Burki, J. J. Meister and H. R. Brunner, *Arterioscler Thromb Vasc Biol*, 1995, **15**, 1781-1786.
57. A. C. Vion, T. Perovic, C. Petit, I. Hollfanger, E. Bartels-Klein, E. Frampton, E. Gordon, L. Claesson-Welsh and H. Gerhardt, *Front Physiol*, 2020, **11**, 623769.
58. A. R. Yadav, R. Sriram, J. A. Carter and B. L. Miller, *Mater Sci Eng C Mater Biol Appl*, 2014, **35**, 283-290.
59. Y. B. Arik, A. de Sa Vivas, D. Laarveld, N. van Laar, J. Gemser, T. Visscher, A. van den Berg, R. Passier and A. D. van der Meer, *Acs Biomater Sci Eng*, 2021, **7**, 2998-3005.
60. A. Vivas, C. IJspeert, J. Y. Pan, K. Vermeul, A. den Berg, R. Passier, S. S. Keller and A. D. van der Meer, *Adv Mater Technol-Us*, 2022, **7**.
61. B. Roberts, A. Haupt, A. Tucker, T. Grancharova, J. Arakaki, M. A. Fuqua, A. Nelson, C. Hookway, S. A. Ludmann, I. A. Mueller, R. Yang, R. Horwitz, S. M. Rafelski and R. N. Gunawardane, *Mol Biol Cell*, 2017, **28**, 2854-2874.
62. V. V. Orlova, F. E. van den Hil, S. Petrus-Reurer, Y. Drabsch, P. Ten Dijke and C. L. Mummery, *Nat Protoc*, 2014, **9**, 1514-1531.
63. A. Liberzon, D. L. M. Aubert, P. Bachant, T. Käufer, Jakirkham, A. Bauer, B. V. C. Dallas, J. Borg and T. Ranleu, *OpenPIV/openpiv-python: OpenPIV - Python (v0.22.2)*, (accessed 26-04-2022, 2022).
64. P. F. Lawton, M. D. Lee, C. D. Saunter, J. M. Girkin, J. G. McCarron and C. Wilson, *Front Physiol*, 2019, **10**, 99.
65. I. Arganda-Carreras, R. Fernandez-Gonzalez, A. Munoz-Barrutia and C. Ortiz-De-Solorzano, *Microsc Res Tech*, 2010, **73**, 1019-1029.

Chapter four:
Supplementary Materials
Multiplexed fluidic circuit board for controlled perfusion of
3D blood vessels-on-a-chip

Electronic supplementary information and supplementary videos available
at:

<https://doi.org/10.1039/D2LC00686C>



Supplementary Figures

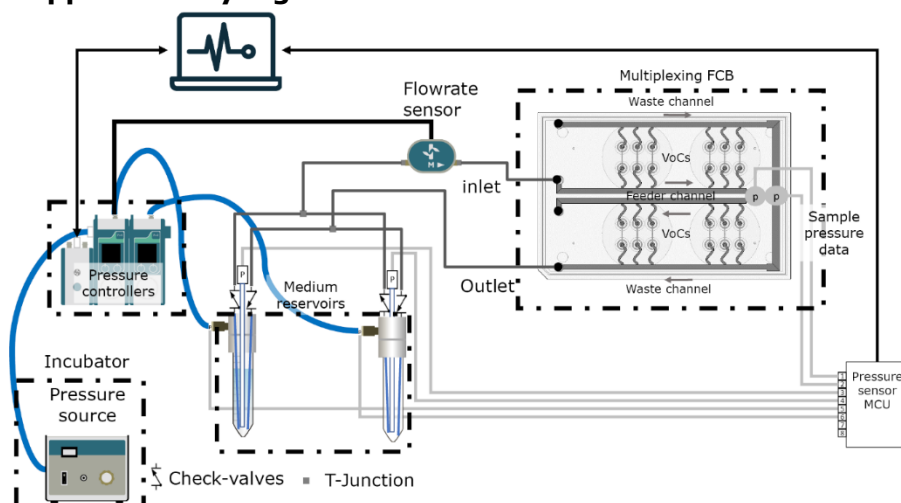


Figure S1: Fluidic circuit used for long-term perfusion. It requires the addition of two T or Y-connectors and results in a unidirectional flow.

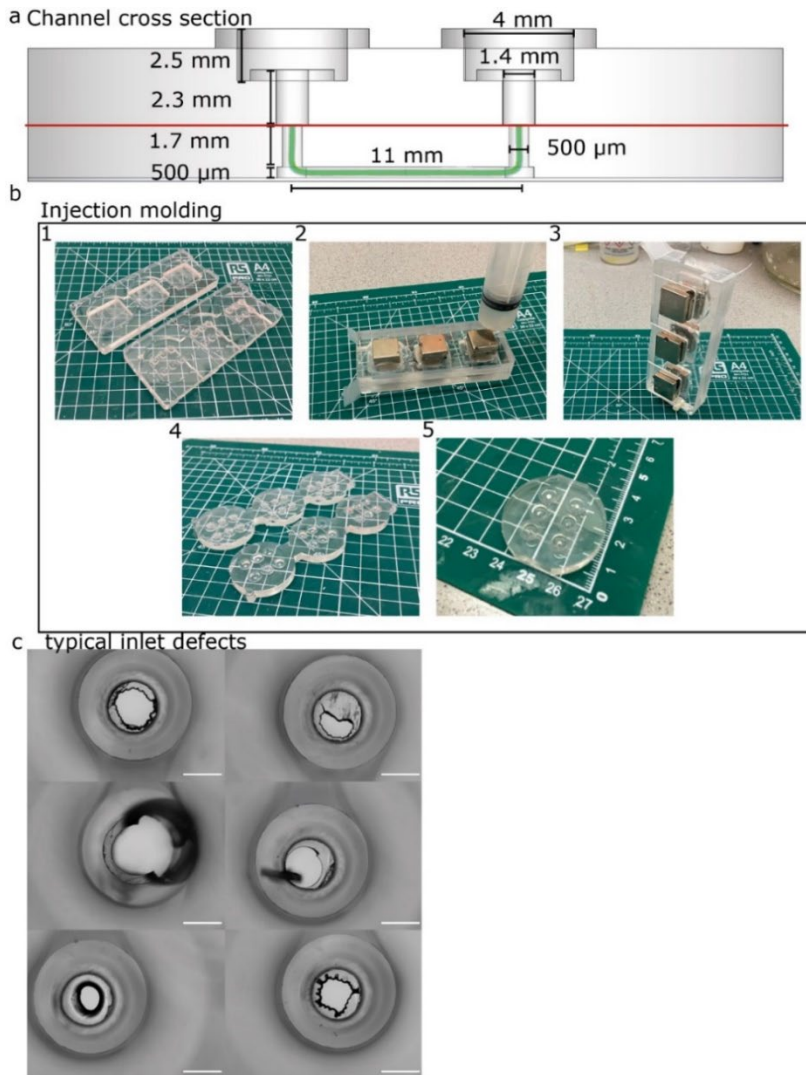


Figure S2: Chip design and Microfabrication using injection moulding. **(a)** Chip design and channel dimensions, green represents the modelled lumen, the red line indicates where the two mould halves have contact. **(b)** Injection moulding. Two separate mould halves show the fluidic channels and medium reservoirs (1). Injection moulds are assembled using strong magnets and PDMS is injected using a syringe (2). The injection mould is placed vertically and allowed to set at room temperature for at least 16 hours (3) followed by 1 hour at 75 °C. Magnets are removed and the PDMS is peeled off (4) excess PDMS is cut off (5) and the chip is assembled with air plasma treatment. **(c)** Defects at the contact points of the injection-moulds result in small membranes of various sizes.

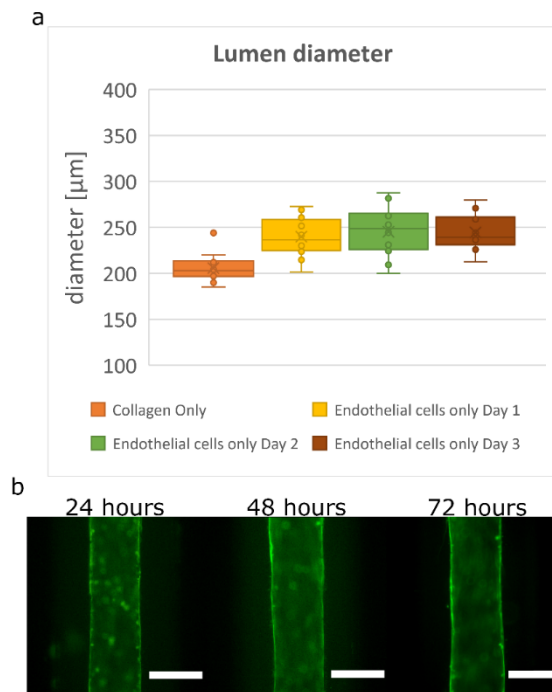


Figure S3: Luminal diameters (a) Boxplot of VFP luminal diameter. Typical luminal diameter ranges of the 3D-VoC in a single experiment shows a diameter expansion after cell seeding. The seeded lumens remain constant in diameter for at least 3 days. **(b)** representative images of lumen at day 1, day 2 and day 3. Scalebar 200 μm

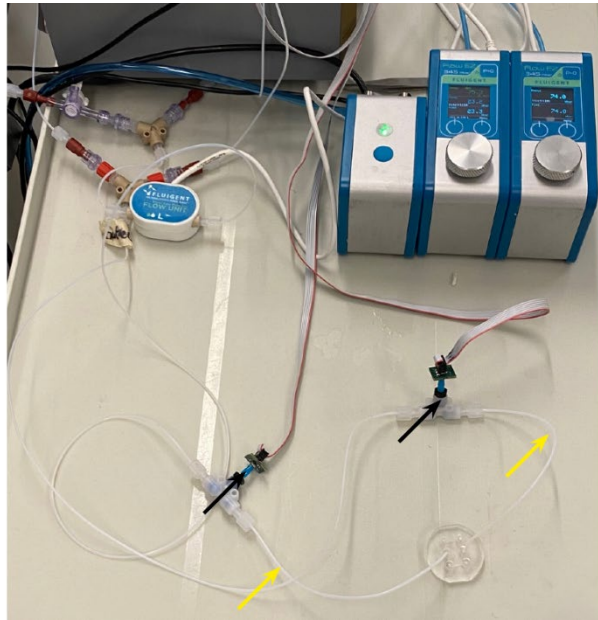


Figure S4: Set-up for measuring individual shear stress. A total of 52 cm of tubing (yellow arrows) was used and placed between the pressure sensors (black arrows) and the samples. The pressure difference was controlled by custom software.

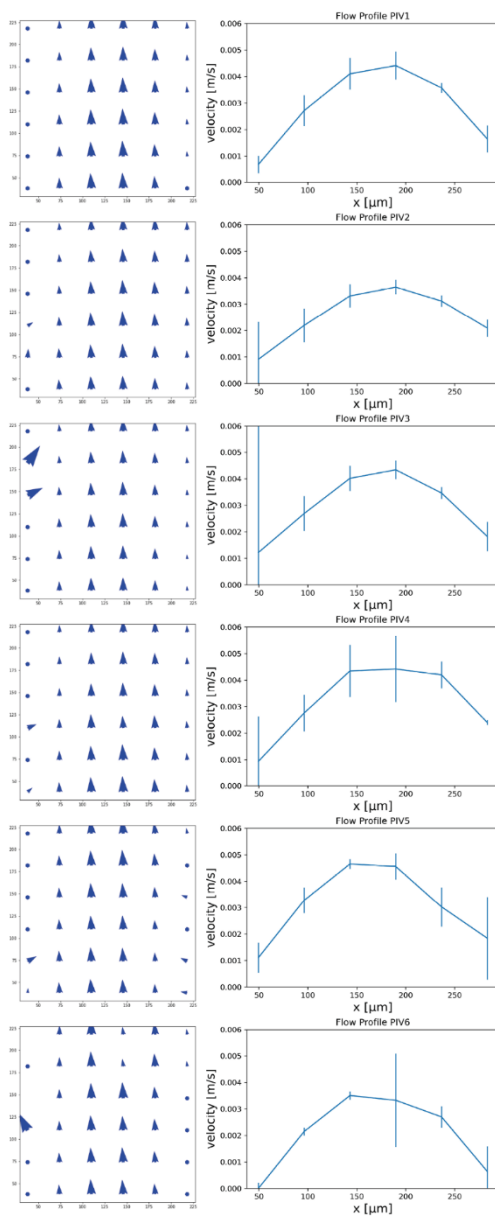


Figure S5: PIV Vector fields and flow profiles of all analysed samples.

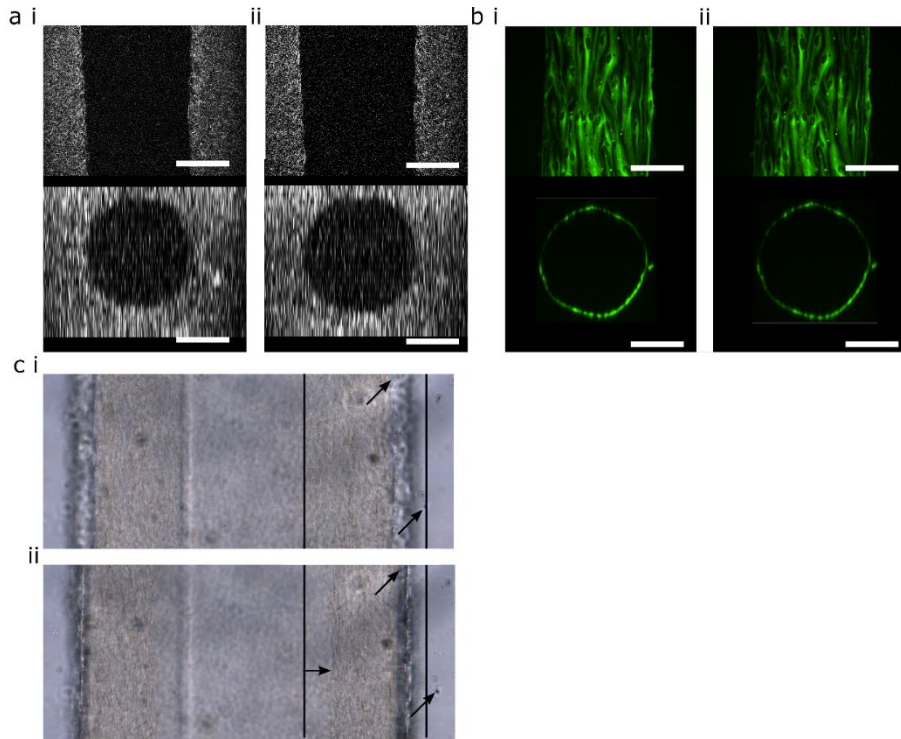


Figure S6: Imaging vascular compliance in 3D. (a) 2p-SHG image of the middle frame and a cross section of the lumen at $P = 0$ mbar (i) and $P = 345$ mbar (ii), see video 3 for the animated sequence. (b) Spinning disc confocal reconstruction bottom half of the lumen cross section of the lumen at $P = 0$ mbar (i) and $P = 345$ mbar (ii), see video 4 for the animated sequence. (c) Frames of video 2 to highlight deformation of the lumen and the PDMS showing $P = 0$ mbar (i) and $P = \pm 1000$ mbar (ii). Arrows and lines are visual references to aid comparison. Scale bars $100 \mu\text{m}$.

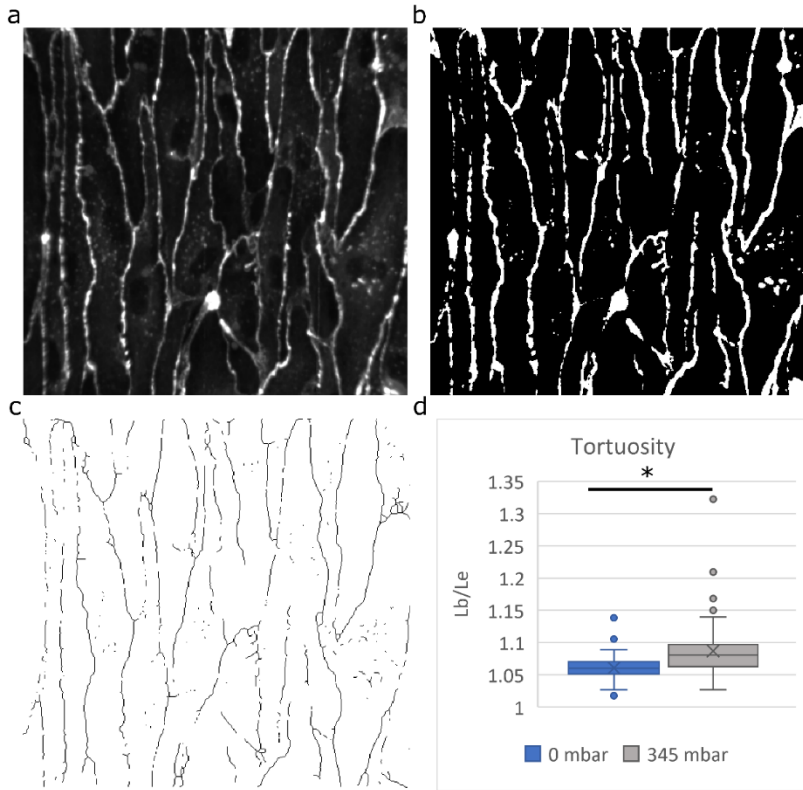


Figure S7: Quantification of the tortuosity index of adherens junctions. (a) Cell junctions visualized using VE-cadherin marker (b) Threshold image of VE-cadherin (c) Skeletonized image of VE-cadherin (d) tortuosity index is calculated by dividing the length of branch (Lb) by the Euclidean distance of that branch (Le). Quantification based on one sequence, one point is one cell junction* indicates $P < 0.001$

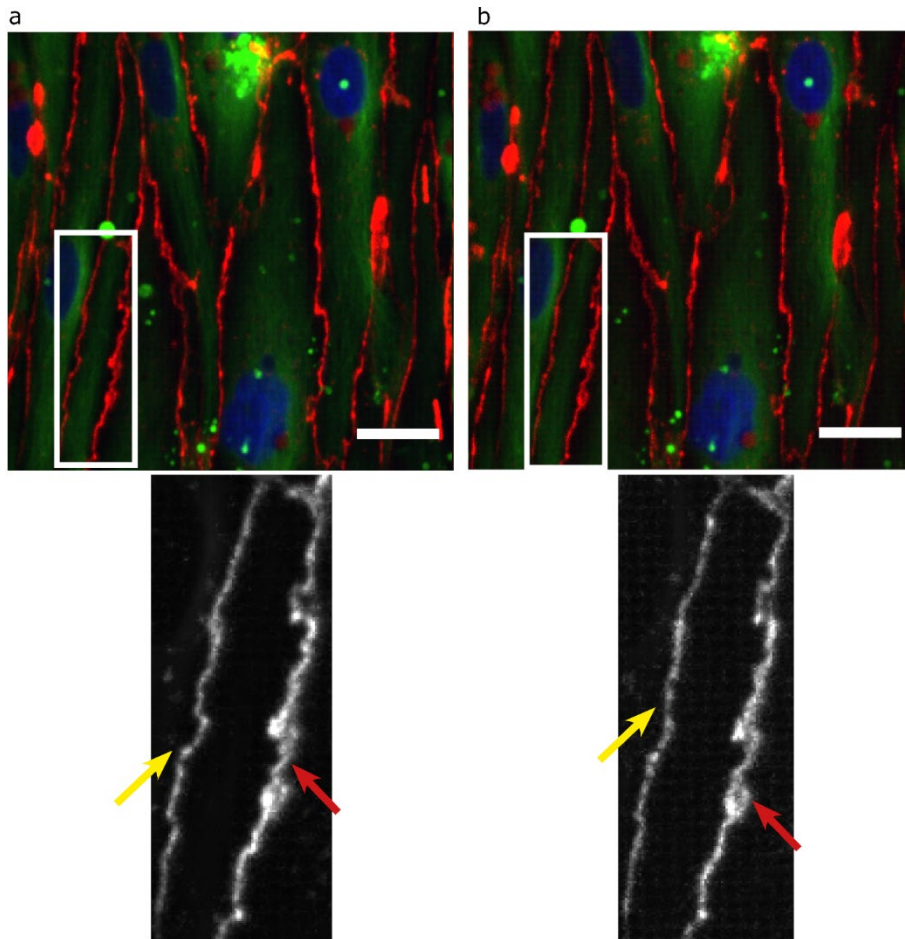


Figure S8: Confocal reconstruction of live TUBA1B-eGFP-ECs. (green) co-stained for adherens junctional marker (VE-cadherin, in red) and nuclei (Hoechst, in blue) at high pressure (345 mbar) (a) and at low pressure (0 mbar) (b). Inserts give example of morphological changes in VE-cadherin cell junctions at high and low pressure. Borders go back to a straight line (yellow arrows) dislocated junctions remain jagged (red arrows). Scale bar 20 μ m.

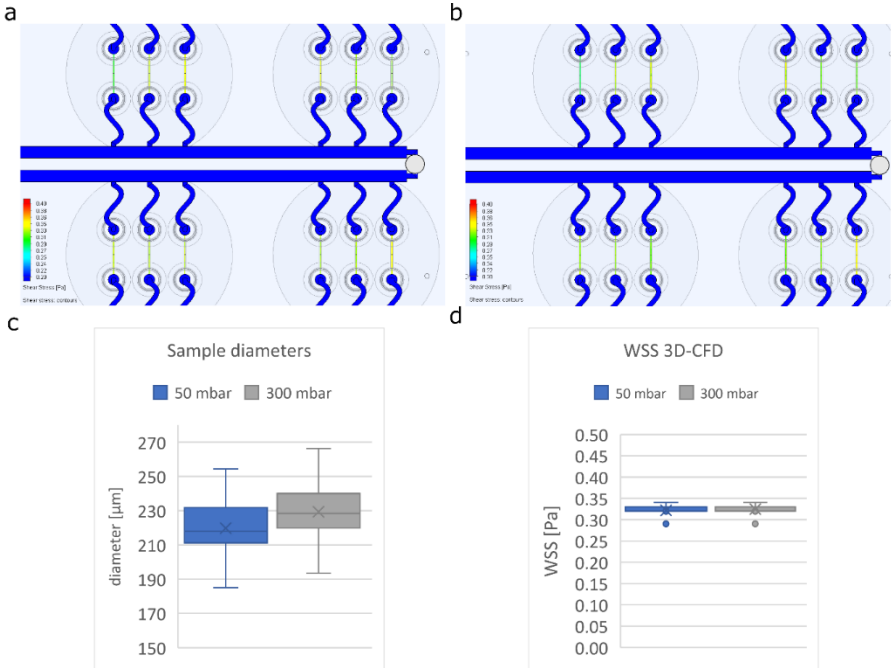


Figure S9: CFD model of perfusion experiment. (a) with an internal pressure of 50 mbar of internal pressure **(b)** with 300 mbar of internal pressure **(c)** Boxplot of all sample diameters at specified internal pressure **(d)** Boxplot of resulting WSS at specified internal pressure.

Supplementary Videos

Video 1 Animation of 3D-CFD model showing the velocity stream lines.

Video 2 Brightfield scaffold only. Pressure was manually applied using a syringe up to 1 bar.

Video 3 2p-SHG sequence of scaffold only of pressure ramp. Frame 1, P = 0 mbar; frame 2, P = 345 mbar.

Video 4 3D-Confocal sequence of the TUB1a-mGFP-hiPSC-ECs pressure ramp. Frame 1, P = 0 mbar; frame 2, P = 345 mbar.

Video 5 Brightfield pressure ramp of the TUB1a-mGFP-hiPSC-ECs monolayer. P = 0-345 mbar, 25 mbar pressure increment per frame, last frame returns to P = 0 mbar.

Video 6 Widefield fluorescent signal of the TUB1a-mGFP-hiPSC-ECs monolayer analysed using the VasoTracker software (blue lines).

Video 7 Confocal reconstruction of pressure ramp. P = 0-50-75-100 mbar. Green: TUB1a-mGFP-hiPSC-ECs, red: VE-Cadherin, blue: Hoechst. Histograms of the red channel were equalized per frame for the reconstruction. Note: last frame shows that the VE-cadherin signal is completely lost due to photobleaching of the fluorophore.

Video 8 Confocal reconstruction of pressure ramp. Frame 1, P = 0 mbar; frame 2, P = 150 mbar; frame 3, P = 345 mbar, frame 4, P = 325 mbar with 1 Pa of WSS. Green: TUB1a-mGFP-hiPSC-ECs, red: VE-Cadherin, blue: Hoechst.

Deriving the equation of optimum resistance of the branch channels to minimize wall shear stress

Hagen–Poiseuille’s law for pressure driven flow:

$$\Delta P = R_h Q \quad \text{Eq. s1}$$

Pressure difference for a serial connected resistance:

$$\Delta P = Q (R_h^{vessel} + R_h^{\tau EQ}) \quad \text{Eq. s2}$$

WSS for circular lumen with given diameter and flowrate

$$\tau = \frac{32 \mu Q}{\pi d^3} \quad \text{Eq. s3}$$

Rewrite to flowrate for given diameter and WSS

$$Q = \frac{\tau \pi d^3}{32 \mu} \quad \text{Eq. s4}$$

Combine Eq. s4 in Eq. s2 with R_h for a circular 3D-VoC assuming uniform diameter of the sample, negligible interstitial flow

$$\Delta P = \left(\frac{\tau \pi d^3}{32 \mu} \right) \left(128 \mu \frac{l_{vessel}}{\pi d^4} + R_h^{\tau EQ} \right) \quad \text{Eq. s5}$$

Set WSS d_{min} equal to WSS d_{max} given equal dP (Eq. s6)

$$\left(\frac{\tau \pi d_{min}^3}{32 \mu} \right) \left(128 \mu \frac{l_{min}}{\pi d_{min}^4} + R_h^{\tau EQ} \right) = \left(\frac{\tau \pi d_{max}^3}{32 \mu} \right) \left(128 \mu \frac{l_{max}}{\pi d_{max}^4} + R_h^{\tau EQ} \right)$$

Eq. s6 can be reduced to Eq. s7

$$\frac{4 l_{min}}{d_{min}} + \left(\frac{\pi d_{min}^3}{32 \mu} \right) R_h^{\tau EQ} = \frac{4 l_{max}}{d_{max}} + \left(\frac{\pi d_{max}^3}{32 \mu} \right) R_h^{\tau EQ}$$

Optimal τEQ resistance can then be expressed in terms of sample diameters

$$R_h^{\tau EQ} = \frac{128 \mu (\frac{l_{min}}{d_{min}} - \frac{l_{max}}{d_{max}})}{\pi (d_{max}^3 - d_{min}^3)}$$

Eq. s8

τEQ resistor dimensions of a rectangular channel:

$$\frac{l_{resistor}}{wh^3(1 - 0.63\frac{h}{w})} = \frac{32(\frac{l_{min}}{d_{min}} - \frac{l_{max}}{d_{max}})}{3\pi(d_{max}^3 - d_{min}^3)}$$

Eq.s9

τEQ resistor dimensions of a circular tube:

$$\frac{l_{res}}{d_{res}^4} = \frac{(\frac{l_{min}}{d_{min}} - \frac{l_{max}}{d_{max}})}{(d_{max}^3 - d_{min}^3)}$$

Eq.s10

Deriving equation: Required ΔP for given WSS

Series circuit of sample and τEQ resistor combined with Eq. s4

$$\Delta P = (\frac{\tau \pi d^3}{32\mu})(128 \mu \frac{L_{vessel}}{\pi d^4} + 12\mu \frac{L}{wh^3(1 - 0.63\frac{w}{h})})$$

Eq. s5

$$\Delta P = (\frac{\tau 4 L_{vessel}}{d} + \frac{\tau 12 \pi d^3 L}{32 wh^3(1 - 0.63\frac{w}{h})})$$

$$\Delta P = \tau (4 \frac{L_v}{d} + \frac{3 \pi d^3 L_{res}}{8 w h^3 (1 - 0.63 \frac{h}{w})})$$

Eq. 1

Equations wall shear stress used for Fig. 2c

Fixed Q red plot:

$$\tau = \frac{32 \mu Q}{\pi d^3} \quad \text{Eq.s3}$$

τ : WSS

Q: flowrate = 90 $\frac{\mu l}{min}$

μ : viscosity= 0.79 Pa s

Chapter four

d: diameter range= 180-300 μm

Fixed P (green plot):

$$\tau = \frac{\Delta P d}{4 l_{vessel}} \text{ Eq. s11}$$

ΔP : Fixed pressure difference= 237 [Pa]

d: Diameter range= 180-300 μm

l:length =1.43 cm

τ_{EQ} + Fixed ΔP blue plot:

$$\tau = \frac{\Delta P}{\left(4 \frac{l_{vessel}}{d} + \frac{3\pi d^3 L_{res}}{8wh^3(1-0.63\frac{h}{w})}\right)} \text{ Eq. s12}$$

Fixed ΔP : 333 [Pa]

d:diameter range= 180-300 μm

l=1.43 cm

L_{res}, w, h = dimensions of resistor listed in table s1 [m]

Table S1: channel dimensions FCB.

			Viscosity [Pa s]	7.90E-04
FCB dimensions	Length [m]	Width [m]	Height [m]	R_h [Pa s m ⁻³]
Feeder channel	0.2	0.0025	0.002	1.90E+08
Feeder loop	0.01	0.0012	0.002	4.40E+07
			Total	2.34E+08
Waste channel	0.2	0.0025	0.002	1.90E+08
Waste loop	0.082	0.0035	0.002	4.33E+07
			Total	2.34E+08
τ_{EQ} -Resistors	0.0171	0.001	0.0002	2.32E+10
3D-VoC	length [m]	d [μm]	R_h including chip resistance	
Small	0.0143	180	4.38E+11	
Medium	0.0143	240	1.39E+11	
Large	0.0143	300	5.68E+10	

Table S2: Dimensions lumen expansion.

	Scaffold-only		EC-monolayer	
	p0	p345	p0	p345
Pressure [mbar]				
Lumen width [μm]	200	220	196	206
Lumen height [μm]	195	215	197	208
Ratio (w/h)	1.03	1.02	0.99	0.99

Chapter five:

Perfusable Engineered capillary using on-Chip hydrogel guided self-assembly and human iPSC-derived vascular cells

Mees N. S. de Graaf^{1*}, Dhanesh G. Kasi^{1,2*}, Francijna E. van den Hil¹, Arn van Maagdenberg², Christine L. Mummery¹, Valeria V. Orlova¹

¹ Department of Anatomy and Embryology, Leiden University Medical Center,

² Department of Human Genetics, Leiden University Medical Center

*Authors contributed equally

In preparation

Abstract

Realistic models of the human vasculature would benefit understanding of normal physiology and disease pathology in the blood circulatory systems. Here we used a photo patterning system to form near vertical hydrogel walls inside a microfluidic device, generating a perfusable network. The hydrogels had realistic (tissue-like) viscoelastic properties and were permeable to large molecules like 70kD dextran. Endothelial cells from human pluripotent stem cells (hiPSC-ECs) cultured in the hydrogels could be guided to form complex networks. hiPSC-ECs inside channels less than 35 μm diameter adopted a tubular morphology much like capillaries in vivo and did not move up the hydrogel wall and ceiling. By contrast, hiPSC-ECs in 50 μm channels, flattened on the glass substrate and covered the complete hydrogel wall and ceiling. We were able to induce swelling in the engineered vessels, mimicking aspects of vascular pathology. In addition, the hydrogel could be designed to form any shape and a range of widths that encompass a range of vessel types in vivo. Using the methodology developed here, we expect to be able to engineer capillary-networks to investigate the complex interplay between peripheral blood cells, the endothelium and drugs under controlled physiological conditions.

5.1 Introduction

The vasculature is essential for proper organ function and is a key determinant of nutrient and drug distribution¹⁻³. Furthermore, blood vessels form the tissue barrier to circulating cells in blood and are thus important for proper inflammatory responses by controlling tissue-barrier permeability and immune cell trafficking⁴. Vessels-on-Chip technology (VoCs) is one way of combining vascular cells in 3D structures resembling blood vessels that support fluidic flow through the lumen. By combining VoCs with biochemical cues like growth factors, extracellular matrix proteins with integrin recognizing-sequences and mechanical stimulation like fluidic flow, synthetic blood vessels with realistic viscoelastic properties can be created⁵.

Different methods are being developed to engineer VoC models which include template casting⁶⁻⁸ and 3D- bioprinting⁹. However, most of these methods are limited in fabrication-resolution and the lumens of the vessels have typically larger diameters ($>100\text{ }\mu\text{m}$) than their *in vivo* equivalents ($5\text{-}20\text{ }\mu\text{m}$). For some aspects of vascular modelling, this difference does not limit their use. For example, wall shear stress (WSS) can be easily scaled according to the model diameter by adjusting the flowrate to achieve that required. However, haemodynamic forces at capillary diameters is more complex and not all characteristics can be appropriately recapitulated¹⁰. One reason is that the luminal diameter of capillary vessels is the same as the diameter of peripheral blood cells. These are then deformed when passing through these capillaries, resulting in haemodynamics that not only depend on continuous fluid flow^{11,12}. Due to the complex fluid dynamics, the exact force experienced by the ECs becomes not only dependent on diameter but also on position and haematocrit¹³. Of note, mural-cell interaction involves complete wrapping of the mural cells around the endothelial tube; this cannot be achieved with larger vessels.

Currently, to engineer complex capillary networks in extracellular matrix (ECM), cellular self-assembly is widely used¹⁴⁻¹⁷. However, these models lack spatial control so that vessels formed vary in diameter which results in haemodynamics that are difficult to control¹⁴. Furthermore, the majority of vessels thus formed have greater diameters than *in vivo*^{14,16}. New methods are therefore being developed to improve the spatial control of capillary network formation.

Scaffold-guided network formation is a potential solution to engineering complex microvascular networks with pre-defined parameters. By using 2-photon Laser ablation¹⁸ or Laser-Based Cavitation¹⁹, small "voids" can be carved inside a hydrogel which can be used to control the size of the model capillary structures. However, for generating complex vascular networks these advanced technologies are time consuming, limiting their scalability. Soft lithography-based approaches allow fabrication of complex capillary-

sized structures inside microfluidic devices²⁰⁻²². These microfluidic networks can be seeded with ECs and can be used for modelling complex haemodynamics. However, the PDMS-channel walls of the microfluidic devices have viscoelastic properties that differ by orders of magnitude from human tissues, affecting how cells experience haemodynamic stimulation nor allow diffusion of drugs or other compounds of interest²³⁻²⁵.

Guided self-assembly using hydrogel microgrooves (<50 μm) also allows the formation of tubular structures at the capillary scale²⁶. Although this approach generates *in vivo* like capillaries in a reproducible and controlled way, they are not perfusable.

To generate perfusable scaffolds that have controllable, *in vivo*-like viscoelastic properties and are permeable to drugs or other compounds, we propose the Primo photo patterning system (Figure 1). The Primo photopatterning system is small footprint, versatile UV-laser which can be used for 2D-cell patterning^{27,28}, microfabrication²⁹ and hydrogel patterning³⁰. A key feature of this system is that any pattern can be designed rapidly and optimized with minimal adjustments using any (open-source) graphical software. Furthermore, the controlling software has an advanced stitching algorithm which allows the fabrication of large patterns with minimal stitching artifacts and large microfluidic devices with micrometre-resolution. Furthermore, the system is capable of controlling the intensity of a single pixel which can be used to locally control height or stiffness of the hydrogel^{29,30}.

We previously reported rapid prototyping of Organ-on-a-Chip (OoC) devices using the primo photopatterning system²⁹. In this present work we demonstrated its immediate application by performing controlled hydrogel structuration on-chip using the same setup. (Synthetic) hydrogels with photo-cross linkable functional groups such as gelatin methacryloyl (GelMA) are essential for this approach and these are biocompatible because they provide cell-binding motifs and support enzymatic degradation³¹. Combined with a photo initiator, they allow fabrication of microenvironments that can be chemically and mechanically modified³⁰. By employing GelMA and lithium phenyl-2,4,6-trimethylbenzoylphosphinate (LAP) as a photo initiator, scaffolds were produced that could be seeded with cells, perfusable and had capillary dimensions (5-25 μm). Relevant mechanical properties were controlled in microfluidic chips that were 50 μm in height.

The level of control demonstrated here allows engineering of capillary-like vessels that can support *in vitro* modelling of vascular structures. Taken together, our approach opens opportunities for microvascular disease modelling and drug transport studies, since the microfluidic chips can be connected to conventional pumping systems and the microvascular networks are perfusable.

5.2 Results and Discussion

We used the Primo photopatterning-system to fabricate both the microfluidic flow-cells used in this study and hydrogel patterning (Figure 1, S1). Because the master-moulds are fragile, we replicated the cast using an epoxy-resin, which is highly durable and temperature resistant (up to 150 °C) which is ideal for PDMS curing(Figure 1a and b). This method further increased the number of casting moulds that could be produced from a single SU-8 mould. The microfluidic channels have the same footprint previously described as being compatible with future perfusion systems³². The gel-reservoir was designed such that the hydrogel could be patterned within 3 frames, minimizing printing time and increasing throughput. Using these dimensions, patterning a single microfluidic channel takes maximally 30 seconds, depending on the required UV-dose(30 mJ/mm²).

Optimizing the pre-polymer solution

GelMA is widely used as a hydrogel for tissue engineering^{31,33}. It is a gelatine-derivative that can be crosslinked using a radical forming photo-initiator and an appropriate light source. Furthermore, it can be mixed with other ECM-components like hyaluronic acid to generate tissue-specific biochemical environments³⁴. Different photo-initiators to initiate radical polymerization of the hydrogel. We tested 2 photo-initiators; Lithium phenyl-2,4,6- trimethyl-benzoylphosphinate (LAP, Advanced Biomatrix) and (PLPP, Alveole). Patterning hydrogels using PLPP as photo-initiator showed that a gap formed between the PDMS and the hydrogel due to the oxygen diffusion from the PDMS, ending the radical polymerization (Figure s2)³⁰. Because this gap limits hydrogel-PDMS crosslinking, PLPP is not recommended. We, therefore, used LAP instead of PLPP because of its high biocompatibility and water solubility. Moreover, LAP can also be activated using light sources with higher wavelengths (+400 nm) which can potentially be used when cells are incorporated inside the hydrogel as it causes less UV-damage.

To determine a suitable pre-polymer composition, an optimal GelMA-concentration was first determined. The GelMA-concentration ranged from 1%-10% and was first checked for suitability in the protocol. To inject the pre-polymer mixture, it is necessary to warm the solution to 37°C as GelMA solutions have a sol-gel transition between 25-35 °C, depending on their concentration. High concentrations (more than 6%) had a rapid sol-gel transition when removed from the heating block and were therefore considered unsuitable for injection into the microfluidic channels. We then tested the polymerisation of GelMA at concentrations ranging from 1%-5% and varied the UV dose up to 90 mJ/mm² and 0.1% LAP, using the Primo photopatterning system. With low concentration (1%) no hydrogel crosslinking was observed. With 2.5% GelMA, defined structures were observed; however these structures were fragile and unsuitable for perfusion (data not shown). Using 5% GelMA, highly defined, flexible structures were

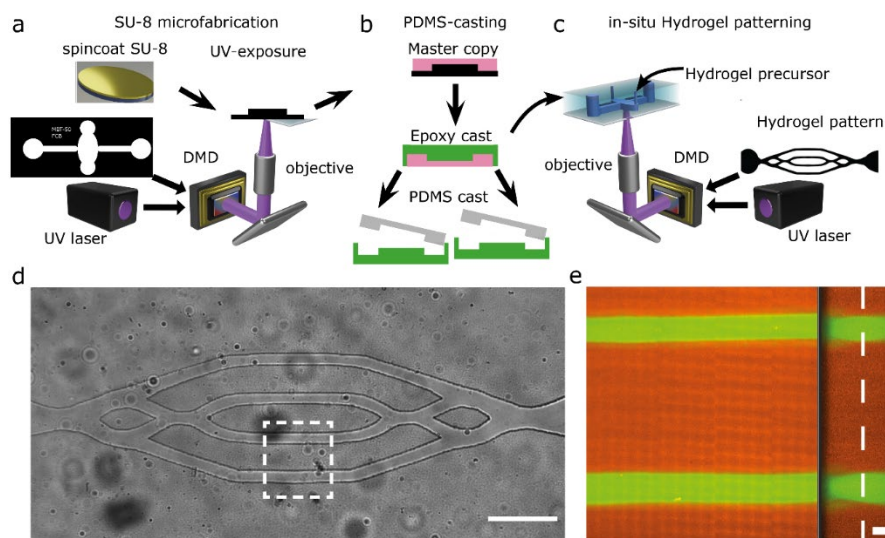


Figure 1: Protocol of hydrogel patterning. (a) the SU-8 master mould (black) is fabricated using the Primo™ photopatterning system (b) the durable master-copy (pink) is cast from the SU-8 moulds from which multiple identical and durable epoxy moulds (green) can be replicated to increase fabrication throughput from a single design (c) hydrogel patterning is performed using the same setup as microfabrication (d) result of patterned hydrogel immediately after patterning (e) hydrogel incubated with 4 kDa-TRITC(Orange) for 24 hours to image hydrogel; channels were flushed with 70 kDa-FITC(green) to enhance contrast with the fluidic channel; YZ-reconstruction shows near vertical formation of 50 μm height hydrogel scaffolds. Dashed line shows slice of interest.

formed, that were resilient to high flow rates and pressure. To determine the optimum LAP concentration, concentrations ranging from 0.01%-0.5% were tested at UV doses up to 30 mJ. Concentrations lower than 0.05% did not polymerize but at 0.1%, well-defined structures were visible even with a UV dose as low as 10 mJ/mm²; this translates to approximately 4 seconds of exposure per frame with the setup and objective used. With higher concentrations of LAP, rapid formation of highly defined structures was observed; however, unwanted crosslinking inside the developing fluidic channels occurred, limiting perfusion. This is due to radical diffusion and at higher concentrations is capable of crosslinking the pre-polymer³⁵. Therefore, a LAP concentration 0.1% was considered optimal for this purpose and setup. Using confocal microscopy, we determined that divergence of the optical pathway is minimal within the height of the microfluidic channel and that the hydrogel walls were near-vertical (Figure 1d).

Using the Primo system as we describe, hydrogels with any arbitrary shape can be patterned (Figure 1 d Figure S1b-d). As an example here, we tested a straight channel and a capillary network based on topological optimized with flow-rate equality constraints³⁶. By infusing the formed hydrogel with a low molecular weight fluorophore and counter-staining the fluidic channel with high-molecular weight dextran the shape of the hydrogel wall can be

imaged using confocal microscopy (Figure 1e). The reconstruction of the Z-stack showed that the hydrogel walls are near-vertical after 24 hours of swelling.

Controlling hydrogel parameters using UV dose.

Next, control of the hydrogel parameters using different UV-doses was determined. First, swelling of the hydrogel structure *in situ* was analysed (Figure 2a). For this, circular structures were patterned using UV doses of 10, 20 and 30 mJ/mm² with incubation for 24 hours at 37 °C. The structures measured were compared with the photomasks and the swelling ratio determined (Figure 2a). This showed dose responsive swelling of the GelMA-hydrogel, with 10 mJ/mm² giving the greatest swelling (swelling ratio of 1.2) and 30 mJ/mm² shows the smallest ratio (swelling ratio of 1.1). Because the channel width is not an intrinsic property of the hydrogel, we investigated how the channel dimensions are influenced by swelling (Figure 2b). This showed that a reduction of 28 µm in the channel width can be expected when using 10 mJ/mm² (Figure 2b and c) a reduction of 14 µm at a dose of 20 mJ/mm² and 8 µm at a dose of 30 mJ/mm². Because of the high swelling at 10 mJ/mm², it is difficult to determine the final channel dimensions exactly and for this reason this was not further investigated.

Determination of diffusion coefficient

To investigate whether the constructed hydrogels allowed compound diffusion, we examined the diffusion of dextran with different molecular weights (Figure 2c). We first patterned a straight channel and perfused it with a mixture of fluorescent dextran compounds (4 kDa, 70 kDa). This mixture was perfused at 1 µl/min using a controlled internal pressure of 20 mbar in the setup described previously to minimize advective transport³². By calculating the error function of the intensity profile, the diffusion coefficient can be determined³⁷. The diffusion coefficient of 70 kDa dextran for 20 mJ/mm² and 30 mJ/mm² was respectively $22 \pm 2 \mu\text{m}^2/\text{s}$ and $20 \pm 2 \mu\text{m}^2/\text{s}$ (Figure 2d), which is similar to values reported previously using hydrogels generated with similar parameters³⁸. The diffusion coefficient of 4 kDa for 20 mJ/mm² and 30 mJ/mm² was $69 \pm 4 \mu\text{m}^2/\text{s}$ and $63 \pm 6 \mu\text{m}^2/\text{s}$ respectively. No reference values were found in literature; however the measured values were as could be expected based on the hydraulic radius and diffusion coefficients in water³⁹. Hydrogels with higher UV doses (>60 mJ/mm²) did not show adequate diffusion ($<0.002 \mu\text{m}^2/\text{s}$ based on penetration depth) of the 70 kDa dextran and are thus not recommended for permeability studies (Figure s3). Although the parameters tested demonstrated the utility of the hydrogels, further characterization is needed. Hydrogel stiffness is an important parameter for tissue engineering and the elastic modulus for soft-tissue can range from <1 kPa for brain to 1 MPa for gut or the nerve tissue²⁵.

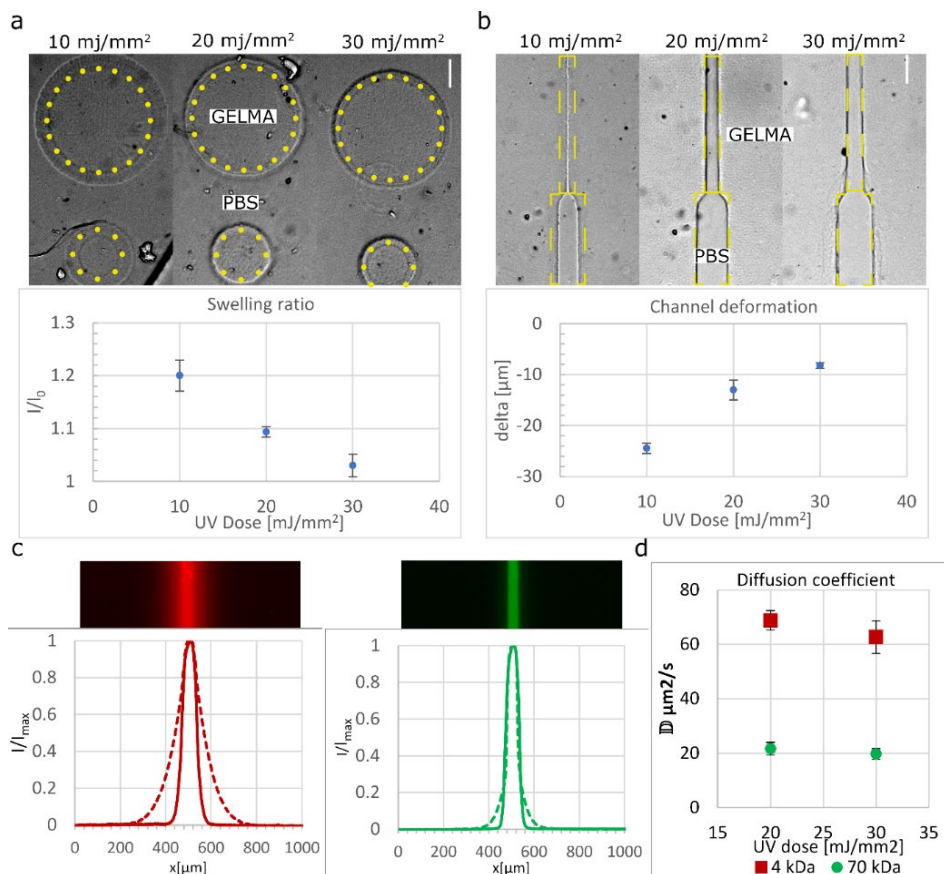


Figure 2: UV-dose related parameters of 5% GelMA and 0.1% LAP. (a) swelling ratio of 100 and 200 μm hydrogel structures **(b)** channel deformation resulting from hydrogel swelling **(c)** 4 kDa-TRITC (red) and 70 kDa-FITC (green) dextran diffusion to validate compound permeability **(d)** Diffusion coefficient of different UV-dose.

Conditions differing by only 3-fold may alter cell phenotype⁴⁰ and therefore accurate determination of mechanical parameters is vital for correct interpretation of experimental data. The stiffness of the construct is dependent on UV-dose, precursor and photo initiator concentration. Although we expected that the hydrogel formed had characteristics similar to *in vivo* (Youngs Modulus of 2 kPa)⁴¹, these parameters still need to be confirmed *in situ*, for example using nanoindentation.

Endothelial cell culture

To examine how vascular cells responded to the engineered scaffolds and test biocompatibility hiPSC-ECs were seeded into the chips using passive pumping (i.e. using the surface tension difference between the 2 mm inlet and 4 mm outlet) to prevent high shear rates and cell damage. In this way, samples could be sequentially seeded although the success rate depended on the quality of the punched inlet.

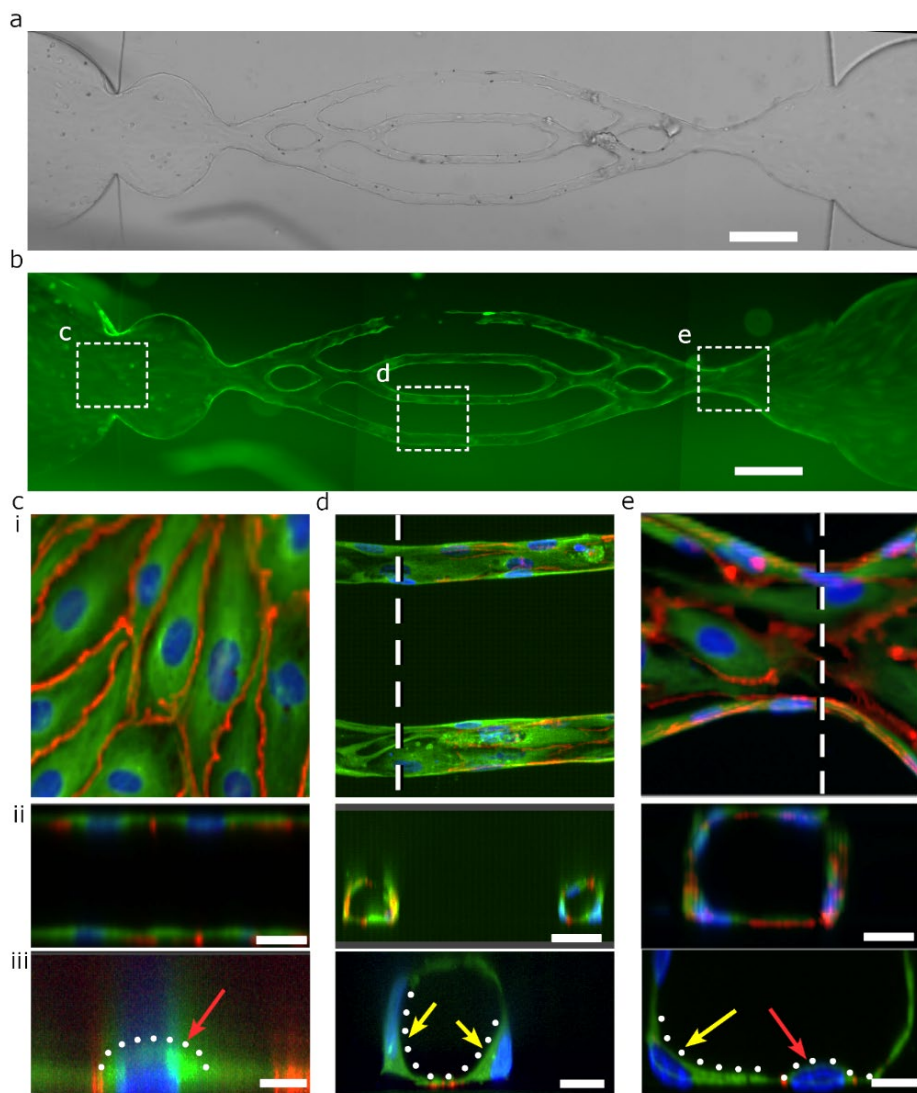


Figure 3: EC-cell culture. (a) widefield overview of cellularized hydrogel scaffold (b) fluorescent overview of cellularized hydrogel scaffold (c) (i) confocal image of 2D hiPSC-EC monolayer (ii) demonstrating coverage of both ceiling and bottom of the fluidic channel (iii) high magnification of hiPSC-EC monolayer showing a convex nucleus (red arrow) (d)(i) confocal image of capillary part of the hydrogel scaffold, (ii) demonstrating formation of tubular structures inside the hydrogel scaffold (iii) high magnification of capillary structures showing concave cell nuclei (yellow arrows) where the cell body is preferably situated in the corner of the small channel (e) (i) confocal image of the outlet of the hydrogel scaffold (ii) showing hiPSC-EC monolayer formation of the hydrogel sidewall and ceiling in the fluidic device (iii) high magnification of wider hydrogel scaffold shows a combination of concave nuclei (yellow arrow) and convex nuclei (red arrow) Scalebars: a,b 200 μm , c,d,e i,ii 20 μm Scalebars iii 10 μm . Green: TUBA1B-mEGFP, Blue: Nuclei, Red: VE-cadherin.

Confocal microscopy was used to examine the hiPSC-ECs in greater detail. This revealed that hiPSC-ECs in wide structures ($>50\text{ }\mu\text{m}$) formed confluent monolayers covering both walls and ceilings, much as in conventional 2D flow channels. However, when the channel width was smaller than $35\text{ }\mu\text{m}$, the hiPSC-ECs formed tubular structures resembling a capillary. Moreover, these tubular structures appeared symmetric, with the same height as width of the vessel. Exploiting this property allowed engineering of luminal diameters as small as $10\text{ }\mu\text{m}$. Within the microfluidic channel these capillary structures were also fully perfusable. Interestingly, within self-assembled tubular structures, the nucleus of the hiPSC-ECs was located preferably on the side of the hydrogel channel and cross sections of the nuclei appeared concave (Figure 4b), similar to those in capillaries *in vivo*⁴² but in contrast to normal planar-cell cultures where the nucleus is convex and within the flow field (Figure 4a). The nucleus has a significant amount of hydrodynamic drag and this can alter cell polarity and the EC-phenotype⁴³. In contrast to our observation in hiPSC-ECs, Human Umbilical Vein ECs (HUVECs) cultured in $30\times 30\text{ }\mu\text{m}$ PDMS- channels retained a monolayer morphology²². Whether the change in nuclear morphology in hiPSC-ECs results in functional differences remains to be investigated.

5.3 Limitations of the presented System

Despite the advantages of the system we described here, it still has some limitations. Firstly, cell seeding is not optimal, as the required inlet/outlet combination for sufficient pressure required large punched holes which resulted in large reservoirs where cells tended to accumulate. Therefore, the use of an optimized Fluidic Circuit Board is recommended to automate cell seeding steps⁴⁴. The capillary network here was designed on the assumption that the hiPSC-ECs would grow vertically on the wall. However, because the cells formed small tubular structures, the shear rates were significantly larger than expected. Therefore, other designs should be considered with a higher number of capillary-like structures to lower the shear rate (figure s1d).

5.4 Conclusion

Using a DMD photo patterning system, we were able to form near vertical hydrogel walls inside a microfluidic device, generating a perfusable network. The hydrogels had realistic (tissue-like) viscoelastic properties compared to PDMS or cell culture plastic and were permeable to large molecules like 70 kD dextran which would make them suitable for drug transport experiments. hiPSC-ECs cultured could be guided to form complex networks in the hydrogels. We found that hiPSC-ECs inside channels less than $35\text{ }\mu\text{m}$, hiPSC-ECs adopted an *in vivo*-like capillary morphology. They did not move up the hydrogel wall and ceiling. hiPSC-ECs in $50\text{ }\mu\text{m}$ channels, flattened on the glass substrate and covered the complete hydrogel wall and ceiling. Using the methodology developed here, it might be possible to engineer a capillary-

network which can be used to investigate the complex interplay between peripheral blood cells and the endothelium under controlled physiological conditions.

5.5 Materials and Methods

Mask-less photolithography to generate the microfluidic device master mould

Glass substrates containing SU-8 microstructures were used as master-moulds and were fabricated as previously described (Figure 1a)²⁹. Briefly, glass substrates coated with a 50 μm thick SU-8-2075 (Kayaku Advanced Materials, Inc) were placed into an adjustable microscope holder for backside UV exposure. A mask-less DMD-based photolithography system (PRIMO, Alvéole) connected to a Leica DMI8 inverted microscope with motorized stage was used for exposure. Binary digital photomasks were designed in an open-source vector graphics editor (Inkscape) according to manufacturers' instructions. Digital photomasks were then loaded into the Leonardo software (Alvéole) and projected by the system onto the substrate via a 5X/0.15NA objective using a 6 mJ/mm² laser dose. Finally, post-exposure bake and subsequent development of SU-8 were performed according to manufacturers' instructions.

Mould replication and Soft Lithography

The SU-8 master-mould was replicated by first generating a master-copy followed by replication to make durable epoxy-resin copies (Figure 1b). This SU-8 master-mould was laminated in 60 mm diameter polystyrene Petri dishes (Greiner Bio-One, Frickenhausen, Germany) using a thin layer of Polydimethylsiloxane (PDMS, sylgard 184, DOW), after which a master copy was made using Smooth-Sil 940 (Smooth-On) according to manufacturers' instructions. Smooth-Sil 940 components were mixed and degassed for 30 min at RT under high vacuum. 10 g was poured into the Petri dish and cured at RT for 24 hours. The Smooth-Sil 940 was then "demoulded" from the Petri dish by carefully cutting a 35 mm circle around the microstructures using a scalpel. Next, the master copies were mounted in a polypropylene cover lid and casted with EpoxAcast 670 HT (Smooth-on). EpoxAcast components were mixed with thinner (100: 17.6:10, A:B:thinner) to reduce resin viscosity according to manufacturers' instructions and degassed at RT for 30 min under high vacuum. The mixture was cast and placed in a sonication bath for 5 min to remove all air bubbles from the structures. After sonication the cast was cured at RT for 24 hours followed by 2 hours at 60 °C and 20 hours at 80 °C. The resulting epoxy moulds were then used for soft lithography to make PDMS chips. Briefly, PDMS was mixed in a 10:1 (base:curing agent) mass ratio and degassed for 30 min at RT, dispensed over the epoxy-moulds and placed at 60 °C. After curing, PDMS was cooled to RT, then the PDMS was gently peeled off. The inlets of the fluidic channels were punched using a 2

mm biopsy puncher. For the outlets, a 4 mm biopsy puncher was used and for the inlets, a 1 mm biopsy puncher.

Chemical functionalization of microfluidic channels

Prepared microfluidic devices and coverslips were treated with air plasma (50 KHz, 50 W) for 1 min (CUTE, Femto Science Inc., Gyeonggi-do, Korea), after which the devices were contact bonded onto the glass coverslips. Fluidic channels were then immediately functionalized to covalently bind the hydrogel to the channel wall. Briefly, a stock solution containing 47.5 % (3-Aminopropyl)triethoxysilane (APTES, sigma) , 50 % methanol(technical grade, Sigma) and 2.5 % distilled water(Gibco) (% v/v) was prepared. The stock solution was then diluted 1:500 to obtain a working solution with a final APTES concentration of 0.095%. The diluted APTES solution was injected in the microfluidic channels and the Petri dish sealed with Parafilm followed by 40 min incubation at RT. A reservoir of 10 ml methanol was included in the closed Petri dish to prevent methanol evaporation. The microfluidic channels were then washed with methanol, dried using a stream of clean dry air (CDA) and baked on a hotplate set at 110 °C for 30 min. 1 % glutaraldehyde solution (v/v) was then injected and the microfluidic devices incubated for 30 min after which they were flushed with distilled water and dried using a stream of CDA.

Hydrogel patterning

All of the following steps up to cell seeding were performed in a room where lighting was filtered using LITHOPROTECT® UV-filter (Litoprotect) to prevent any unwanted crosslinking. 10% gelatin methacryloyl (GelMA, Bloom 300, Sigma-Aldrich) in phosphate-buffered saline (PBS) (w/v) was filtered using a 0.2 µm Puradisc syringe filter (Whatman), aliquoted and stored at 4 °C. Before using, the solution was pre-warmed to 37 °C and mixed 1:1 with freshly prepared and filtered 0.2 % lithium phenyl-2,4,6 trimethylbenzoylphosphinate (LAP, Sigma-Aldrich) in PBS solution (w/v) to obtain a hydrogel working solution containing 5 % GelMA and 0.1 % LAP. Finally, the working solution was prewarmed to 37 °C and 3 µL was injected into the gel chambers of the prewarmed microfluidic devices. The filled microfluidic devices were immediately placed into an adjustable microscope holder for exposure using the DMD-based system (PRIMO, Alvéole, France). A digital photomask containing the GelMA scaffold pattern was designed in Inkscape, loaded into Leonardo (Alvéole) and projected by the system onto the microfluidic device gel chamber via a 5X/0.15NA objective using the specified laser dose. Microfluidic devices were then flushed using a prewarmed syringe with PBS without Ca²⁺ and Mg²⁺ (PBS-) to remove non-crosslinked GelMA and excess photo initiator.

To promote later cell adhesion, chips were incubated with a filtered fibronectin solution (10 µg/ml, bovine, Thermo Fisher Scientific) for 30 min,

flushed with cell culture medium (EGM-2) and finally incubated at 37 °C until cell seeding.

Determination of hydrogel swelling ratio

A digital photomask containing circular patterns of 100 and 200 μm in diameter was designed in Inkscape and projected using the PRIMO system at laser doses of 10, 20 and 30 mJ/mm^2 using the Leonardo software (Alvéole) and prepared as described above. The microfluidic devices were flushed with EC growth medium (EGM-2) and placed inside an incubator at 37 °C for 24 hours. After incubation, the structured hydrogels inside the devices were imaged using an EVOS M7000 microscope (ThermoFisher Scientific) and compared to the dimensions of the digital photomask. Similarly, straight fluidic channels 30 and 60 μm in width (Figure s1b) were patterned and flushed as described above. After 24 hrs incubation, the hydrogel channels were imaged and compared to the dimensions on the digital photomask.

Determination of diffusion coefficient

Straight channels (60 and 30) μm in width (Figure s1b) were generated as described above using a 20 and 30 mJ/mm^2 laser dose. EGM2 was supplemented with 4-kDa TRITC-dextran (0.03 mg/ml, 7.1 μM) and 70-kDa FITC-dextran (0.5 mg/ml, 7.1 μM). Microfluidic devices were individually connected to a custom designed perfusion system (Fluigent) controlled as previously described³², with an internal pressure lower than 20 mbar to limit advective transport towards the gel during perfusion. Devices were placed on an EVOS M7000 microscope (ThermoFisher Scientific) and sequential images were obtained at an interval of 15 seconds for 10 min. Images were analysed using a custom python script to determine the diffusion coefficient by fitting the error function on the intensity profile, as described elsewhere³⁷. The average of the first 5 timepoints was used as the diffusion coefficient.

Differentiation and expansion of hiPSC-ECs

Alpha-tubulin- monomeric Enhanced Green Fluorescent Protein-hiPSCs (TUBA1B-mEGFP, Cell Line ID: AICS-0012 cl.105, <https://hpscereg.eu/cell-line/UCSFi001-A-2>) were obtained from the Allen institute⁴⁵. hiPSC-ECs were differentiated as previously described⁴⁶. Briefly, TUBA1B-mEGFP-hiPSCs were maintained in TeSR™-E8™ medium on vitronectin-coated 6-well plates and seeded at day (-1). Twenty-four hours after seeding, E8 medium was replaced with B(P)EL medium supplemented with 8 μM CHIR. On day 3, the medium was replaced with B(P)EL medium supplemented with 50 ng/ml VEGF (R&D systems) and 10 μM SB431542 (Tocris Bioscience); cells were refreshed with the same medium on days 7 and 9. hiPSC-ECs were isolated on day 10 using CD31-Dynabeads™ (Invitrogen), expanded for 3 days and cryopreserved. hiPSC-ECs from cryo-preserved batches were used in all experiments. They were thawed and expanded in Endothelial Cell-Serum Free

Medium (EC-SFM, Gibco, cat. No. 11111-044) supplemented with 1 % human platelet poor serum, FGF2 (20 ng/mL) and VEGF (30 ng/mL), on a 0.1 % gelatine-coated T-75 culture flask. hiPSC-ECs were used at passage 2 for all experiments.

Seeding of scaffolds with hiPSC-ECs

hiPSC-ECs were harvested using TrypLE™ (ThermoFisher Scientific) and resuspended at a concentration of 15×10^6 cells/ml in EGM-2 supplemented with 50 ng/mL VEGF and PenStrep(25 Units/ml). 2 μ l of cell suspension was carefully pipetted on to the bottom of the inlet (2 mm) using gel-loader pipette tips and cells traversed the microfluidic channels via passive pumping. Once cells were stationary, medium was pipetted into the outlet and cells were incubated for 2 days. Medium was refreshed twice a day using passive pumping.

Live cell staining and microscopy

hiPSC-ECs were in culture for 48 hours on the patterned hydrogels. Prior to imaging, 10 μ l of EGM-2 with anti-VE-cadherin (CD144-mouse anti-Human Alexa-647, BD Bioscience, diluted 1:200) and Hoechst—33342 (ThermoFischer Scientific, 1 μ g /ml) was injected into the microfluidic devices and incubated for 30 min at 37 °C. Next, medium was refreshed and samples were imaged using Leica DMI8 microscope equipped with a Dragonfly® spinning disk (pinhole:20 μ m) (Andor). A HC PL APO 20x/0.75 IMM CORR CS2 objective was used with water as immersion medium. This objective was combined with 2x camera magnification to enhance lateral resolution. An iXon CCD camera was used to record the signal. Details of the capillary bed were imaged using 63x or 100x objectives using oil as immersion medium and a pinhole of 40 μ m.

Supplementary materials

See Supplementary materials for additional figures of design masks, PLPP based crosslinking, high UV-dose permeability and EC sprout-formation.

References

- 1 Glassman, P. M. *et al.* Targeting drug delivery in the vascular system: Focus on endothelium. *Adv Drug Deliv Rev* **157**, 96-117, doi:10.1016/j.addr.2020.06.013 (2020).
- 2 Reiterer, M. & Branco, C. M. Endothelial cells and organ function: applications and implications of understanding unique and reciprocal remodelling. *Febs J* **287**, 1088-1100, doi:10.1111/febs.15143 (2020).
- 3 Urbanczyk, M., Zbinden, A. & Schenke-Layland, K. Organ-specific endothelial cell heterogeneity and its impact on regenerative medicine and biomedical engineering applications. *Adv Drug Deliv Rev* **186**, 114323, doi:10.1016/j.addr.2022.114323 (2022).
- 4 Muller, W. A. Leukocyte-endothelial-cell interactions in leukocyte transmigration and the inflammatory response. *Trends Immunol* **24**, 327-334, doi:10.1016/s1471-4906(03)00117-0 (2003).
- 5 James, B. D. & Allen, J. B. Vascular Endothelial Cell Behavior in Complex Mechanical Microenvironments. *Acs Biomater Sci Eng* **4**, 3818-3842, doi:10.1021/acsbomaterials.8b00628 (2018).
- 6 Chrobak, K. M., Potter, D. R. & Tien, J. Formation of perfused, functional microvascular tubes in vitro. *Microvasc Res* **71**, 185-196, doi:10.1016/j.mvr.2006.02.005 (2006).
- 7 Jimenez-Torres, J. A., Peery, S. L., Sung, K. E. & Beebe, D. J. LumeNEXT: A Practical Method to Pattern Luminal Structures in ECM Gels. *Adv Healthc Mater* **5**, 198-204, doi:10.1002/adhm.201500608 (2016).
- 8 Polacheck, W. J., Kutys, M. L., Tefft, J. B. & Chen, C. S. Microfabricated blood vessels for modeling the vascular transport barrier. *Nat Protoc* **14**, 1425-1454, doi:10.1038/s41596-019-0144-8 (2019).
- 9 Kolesky, D. B. *et al.* 3D bioprinting of vascularized, heterogeneous cell-laden tissue constructs. *Adv Mater* **26**, 3124-3130, doi:10.1002/adma.201305506 (2014).
- 10 Ebrahimi, S. & Bagchi, P. A computational study of red blood cell deformability effect on hemodynamic alteration in capillary vessel networks. *Sci Rep* **12**, 4304, doi:10.1038/s41598-022-08357-z (2022).
- 11 Secomb, T. W., Hsu, R. & Pries, A. R. Motion of red blood cells in a capillary with an endothelial surface layer: effect of flow velocity. *Am J Physiol Heart Circ Physiol* **281**, H629-636, doi:10.1152/ajpheart.2001.281.2.H629 (2001).
- 12 Hogan, B., Shen, Z., Zhang, H., Misbah, C. & Barakat, A. I. Shear stress in the microvasculature: influence of red blood cell morphology and endothelial wall undulation. *Biomech Model Mechanobiol* **18**, 1095-1109, doi:10.1007/s10237-019-01130-8 (2019).
- 13 Ascolese, M., Farina, A. & Fasano, A. The Fahraeus-Lindqvist effect in small blood vessels: how does it help the heart? *J Biol Phys* **45**, 379-394, doi:10.1007/s10867-019-09534-4 (2019).
- 14 Kim, S., Lee, H., Chung, M. & Jeon, N. L. Engineering of functional, perfusable 3D microvascular networks on a chip. *Lab Chip* **13**, 1489-1500, doi:10.1039/c3lc41320a (2013).
- 15 Adriani, G., Ma, D., Pavesi, A., Kamm, R. D. & Goh, E. L. A 3D neurovascular microfluidic model consisting of neurons, astrocytes and cerebral endothelial cells as a blood-brain barrier. *Lab Chip* **17**, 448-459, doi:10.1039/c6lc00638h (2017).
- 16 Wan, Z. *et al.* A Robust Method for Perfusable Microvascular Network Formation In Vitro. *Small Methods* **6**, e2200143, doi:10.1002/smt.202200143 (2022).
- 17 Phan, D. T. T. *et al.* A vascularized and perfused organ-on-a-chip platform for large-scale drug screening applications. *Lab Chip* **17**, 511-520, doi:10.1039/c6lc01422d (2017).
- 18 Arakawa, C. *et al.* Biophysical and biomolecular interactions of malaria-infected erythrocytes in engineered human capillaries. *Sci Adv* **6**, eaay7243, doi:10.1126/sciadv.aay7243 (2020).
- 19 Enrico, A. *et al.* 3D Microvascularized Tissue Models by Laser-Based Cavitation Molding of Collagen. *Adv Mater* **34**, e2109823, doi:10.1002/adma.202109823 (2022).
- 20 Fenech, M. *et al.* Microfluidic blood vasculature replicas using backside lithography. *Lab Chip* **19**, 2096-2106, doi:10.1039/c9lc00254e (2019).
- 21 Tsai, M. *et al.* In vitro modeling of the microvascular occlusion and thrombosis that occur in hematologic diseases using microfluidic technology. *J Clin Invest* **122**, 408-418, doi:10.1172/JCI58753 (2012).
- 22 Tsvirkun, D., Grichine, A., Duperray, A., Misbah, C. & Bureau, L. Microvasculature on a chip: study of the Endothelial Surface Layer and the flow structure of Red Blood Cells. *Sci Rep* **7**, 45036, doi:10.1038/srep45036 (2017).
- 23 Deguchi, S., Hotta, J., Yokoyama, S. & Matsui, T. S. Viscoelastic and optical properties of four different PDMS polymers. *J Micromech Microeng* **25**, doi:10.1088/0960-1317/25/9/097002 (2015).

- 24 Johnston, I. D., McCluskey, D. K., Tan, C. K. L. & Tracey, M. C. Mechanical characterization of bulk Sylgard 184 for microfluidics and microengineering. *J Micromech Microeng* **24**, doi:10.1088/0960-1317/24/3/035017 (2014).
- 25 Guimarães, C. F., Gasperini, L., Marques, A. P. & Reis, R. L. The stiffness of living tissues and its implications for tissue engineering. *Nat Rev Mater* **5**, 351-370, doi:10.1038/s41578-019-0169-1 (2020).
- 26 Jiang, L. Y. & Luo, Y. Guided assembly of endothelial cells on hydrogel matrices patterned with microgrooves: a basic model for microvessel engineering. *Soft Matter* **9**, 1113-1121, doi:10.1039/c2sm27126e (2013).
- 27 Delepine, C. *et al.* Altered microtubule dynamics and vesicular transport in mouse and human MeCP2-deficient astrocytes. *Hum Mol Genet* **25**, 146-157, doi:10.1093/hmg/ddv464 (2016).
- 28 Strale, P. O. *et al.* Multiprotein Printing by Light-Induced Molecular Adsorption. *Adv Mater* **28**, 2024-2029, doi:10.1002/adma.201504154 (2016).
- 29 Kasi, D. G. *et al.* Rapid Prototyping of Organ-on-a-Chip Devices Using Maskless Photolithography. *Micromachines (Basel)* **13**, doi:10.3390/mi13010049 (2021).
- 30 Pasturel, A., Strale, P. O. & Studer, V. Tailoring Common Hydrogels into 3D Cell Culture Templates. *Adv Healthc Mater* **9**, e2000519, doi:10.1002/adhm.202000519 (2020).
- 31 Bupphathong, S. *et al.* Gelatin Methacrylate Hydrogel for Tissue Engineering Applications-A Review on Material Modifications. *Pharmaceuticals (Basel)* **15**, doi:10.3390/ph15020171 (2022).
- 32 de Graaf, M. N. S., Vivas, A., van der Meer, A. D., Mummery, C. L. & Orlova, V. V. Pressure-Driven Perfusion System to Control, Multiplex and Recirculate Cell Culture Medium for Organs-on-Chips. *Micromachines (Basel)* **13**, 1359, doi:10.3390/mi13081359 (2022).
- 33 Xiao, S. *et al.* Gelatin Methacrylate (GelMA)-Based Hydrogels for Cell Transplantation: an Effective Strategy for Tissue Engineering. *Stem Cell Rev Rep* **15**, 664-679, doi:10.1007/s12015-019-09893-4 (2019).
- 34 Skardal, A. *et al.* Photocrosslinkable hyaluronan-gelatin hydrogels for two-step bioprinting. *Tissue Eng Part A* **16**, 2675-2685, doi:10.1089/ten.TEA.2009.0798 (2010).
- 35 LeValley, P. J. *et al.* Fabrication of Functional Biomaterial Microstructures by in Situ Photopolymerization and Photodegradation. *ACS Biomater Sci Eng* **4**, 3078-3087, doi:10.1021/acsbiomaterials.8b00350 (2018).
- 36 Liu, Z. Y., Gao, Q. Y., Zhang, P., Xuan, M. & Wu, Y. H. Topology optimization of fluid channels with flow rate equality constraints. *Struct Multidiscip O* **44**, 31-37, doi:10.1007/s00158-010-0591-x (2011).
- 37 Park, G. Y. Diffusion coefficient calculated by complementary error function for the sublimation diffusion of disperse dye (vol 14, pg 1, 2019). *J Eng Fiber Fabr* **15**, doi:10.1177/1558925019885200 (2020).
- 38 Kaemmerer, E. *et al.* Gelatine methacrylamide-based hydrogels: an alternative three-dimensional cancer cell culture system. *Acta Biomater* **10**, 2551-2562, doi:10.1016/j.actbio.2014.02.035 (2014).
- 39 Silva, J. V., Peixoto, P. D., Lortal, S. & Floury, J. Transport phenomena in a model cheese: the influence of the charge and shape of solutes on diffusion. *J Dairy Sci* **96**, 6186-6198, doi:10.3168/jds.2013-6552 (2013).
- 40 Shen, Y. *et al.* Reduction of Liver Metastasis Stiffness Improves Response to Bevacizumab in Metastatic Colorectal Cancer. *Cancer Cell* **37**, 800-817.e807, doi:10.1016/j.ccell.2020.05.005 (2020).
- 41 Yin, J., Yan, M., Wang, Y., Fu, J. & Suo, H. 3D Bioprinting of Low-Concentration Cell-Laden Gelatin Methacrylate (GelMA) Bioinks with a Two-Step Cross-linking Strategy. *ACS Appl Mater Interfaces* **10**, 6849-6857, doi:10.1021/acsami.7b16059 (2018).
- 42 Nahirney, P. C. & Tremblay, M. E. Brain Ultrastructure: Putting the Pieces Together. *Front Cell Dev Biol* **9**, 629503, doi:10.3389/fcell.2021.629503 (2021).
- 43 Tkachenko, E. *et al.* The nucleus of endothelial cell as a sensor of blood flow direction. *Biol Open* **2**, 1007-1012, doi:10.1242/bio.20134622 (2013).
- 44 Vollertsen, A. R. *et al.* Modular operation of microfluidic chips for highly parallelized cell culture and liquid dosing via a fluidic circuit board. *Microsyst Nanoeng* **6**, 107, doi:10.1038/s41378-020-00216-z (2020).
- 45 Roberts, B. *et al.* Systematic gene tagging using CRISPR/Cas9 in human stem cells to illuminate cell organization. *Mol Biol Cell* **28**, 2854-2874, doi:10.1091/mbc.E17-03-0209 (2017).
- 46 Orlova, V. V. *et al.* Generation, expansion and functional analysis of endothelial cells and pericytes derived from human pluripotent stem cells. *Nat Protoc* **9**, 1514-1531, doi:10.1038/nprot.2014.102 (2014).

Chapter five: Supplementary materials

Perfusable Engineered capillary bed using on-Chip hydrogel guided self-assembly and iPSC derived vascular cells

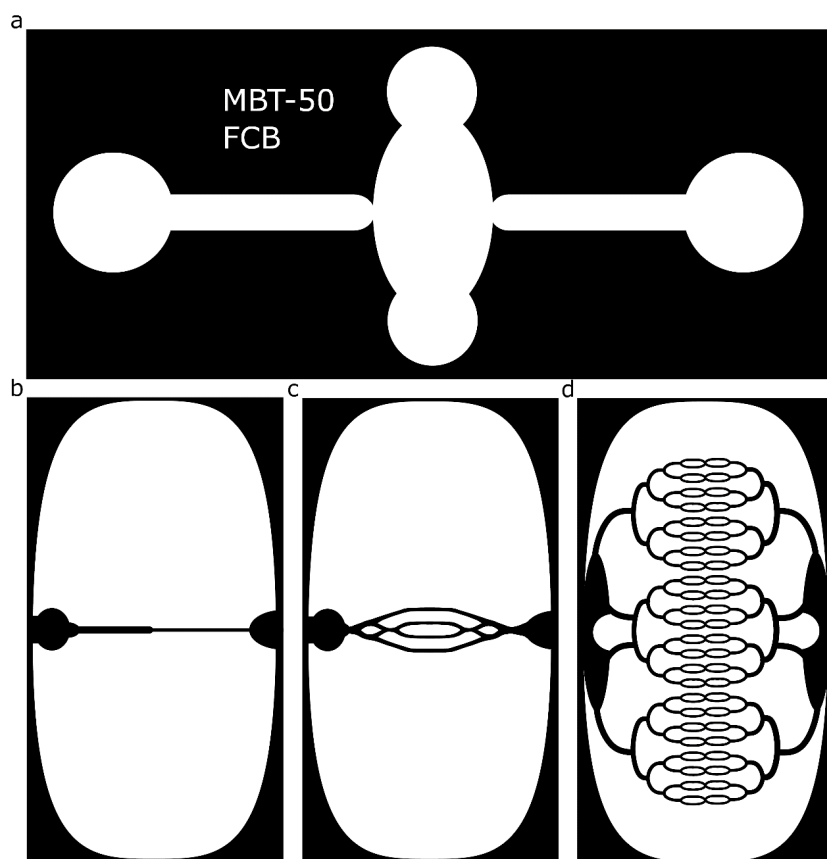


Figure S1: Used patterns for this study. (a) microfluidic channel (b) straight channels (c) topological optimized capillary network (d) proposed high density capillary network

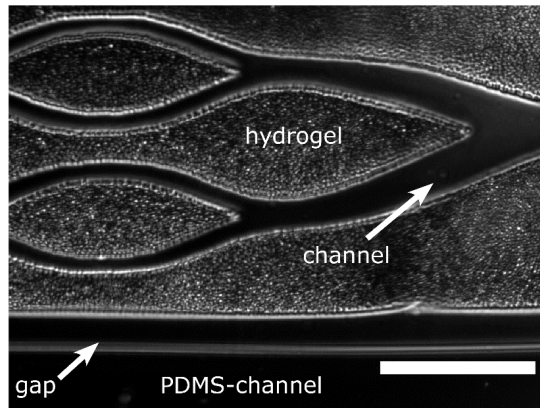


Figure S2: Hydrogel patterning with PLPP. a gap is visible between hydrogel and PDMS- side wall. Scale bar is 200 μ m

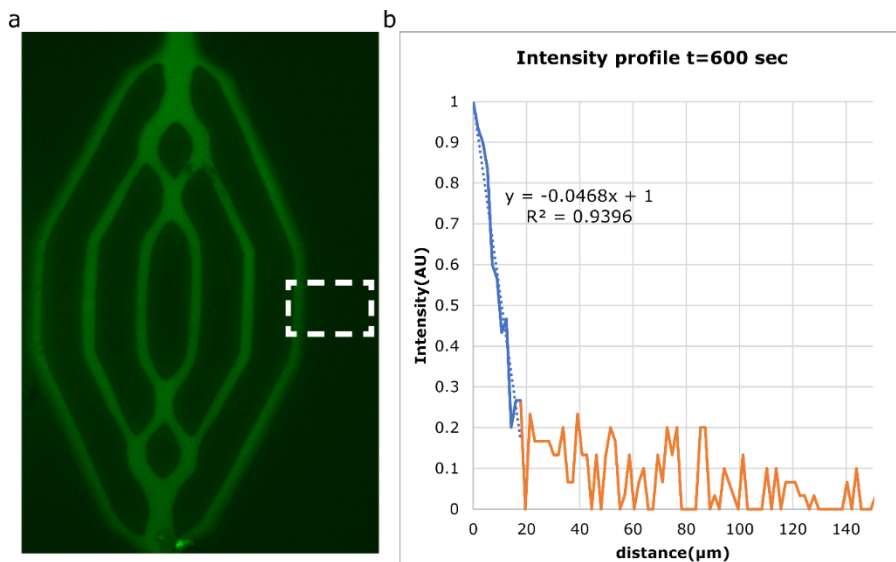


Figure S3: Permeability of 70kDa in hydro gel patterned with 60 mj/mm². Analyses shows minimal penetration of the fluorescent dextran and accompanied low diffusion coefficient.

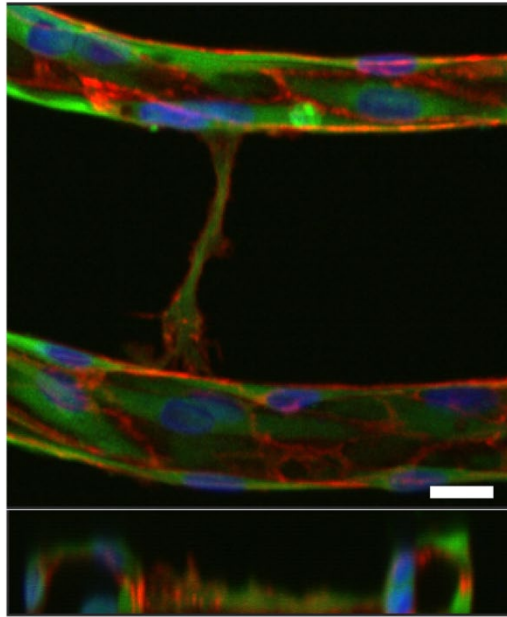


Figure S4: 3D-Sprout formation. Sprout formation demonstrates the ability of ECs to modify the patterned hydrogel. Scalebar 10 μm

Chapter six:

General discussion

Discussion

Combining differentiated pluripotent stem cells (hiPSCs) with Organ-on-Chip (OoC) technology has the potential to improve *in vitro* disease modelling and drug discovery¹. Currently, standard cell-culture models, even when based on hiPSC derivatives from patients, still fail to capture many aspects of human physiological reality, missing important information for adequate drug-effect and toxicity prediction². This failure can be partly attributed to the cell culture conditions, that typically consist of single cell-types, grown on two-dimensional culture plastic that has viscoelasticity properties that differ by orders of magnitude from that in real tissue³. Because of this, *in vitro* cell cultures miss (or have inappropriate) intracellular communication, cellular orientation and the biomechanical stimulation necessary for correct cellular phenotype and drug response^{4,5}. By modifying the extracellular environment to mimic aspects of real tissue *in vitro*, models based on OoC-technology can improve the predictive value of cultured cells for disease modelling and drug discovery compared to the standard *in vitro* assays⁶.

Despite this potential of OoCs, widespread use of this technology is still limited because it is highly multi- and interdisciplinary, with the challenges of combining advanced engineering, with complex and highly skilled stem cell biology by a single end-user⁷.

As discussed in this thesis, hiPSC can give rise to all cells of the human body but in the context of OoCs, hiPSC-derived endothelial cells (hiPSCs-ECs) are of particular interest as a cellular lining to microfluidic channels, as they provide a way of mimicking (diseased and healthy) blood vessels⁸. This thesis focused on the development of 3D vascular models that combine hiPSC-derived vascular cells (both ECs and adjacent pericytes or smooth muscle cells) and haemodynamic forces. These mechanical stimuli are essential for revealing a “true” EC-phenotype close to that of ECs in vessels of the human body⁹. The perfusable 3D-vessels-on-chip (3D-VoCs) described in this thesis were developed to bring OoC technology closer to the end user; therefore, they were developed to be scalable, reproducible and compatible with the biology carried out in laboratories modelling vascular disease and examining responses to drugs.

As described in **chapter 1**, hiPSC-ECs have many advantages compared to the primary and immortalized endothelial cell lines currently used, not least their batch-to-batch consistency¹⁰. However, their phenotype is immature and they resemble foetal rather than adult vessels in their (functional) properties and gene profile¹¹. Improving their biology to mimic more mature vessels, requires the introduction of realistic functional parameters such as fluidic flow and biomaterials with realistic viscoelastic properties and structures¹². Different methods are being developed to generate 3D vascular models. However, many methods rely on specialized equipment, reagents

and extensive know-how. Only a few methods are scalable, support controlled-perfusion and are easy to implement within biologically oriented laboratories.

Development of scalable 3D-VoCs compatible with controlled perfusion.

In **Chapter 2** we therefore described a scalable method to fabricate 3D-VoCs scaffolds, compatible with controlled perfusion. The method uses a microfluidic technique called Viscous Finger Patterning (VFP). VFP exploits a phenomenon called the Saffman–Taylor instability that occurs when a viscous fluid is displaced by a less viscous fluid on a microfluidic scale¹³. The less viscous fluid displaces the viscous hydrogel faster at the centre of the fluidic-channel than at the boundary-wall, resulting in a circular lumen inside the hydrogel. In essence, this protocol is the sequential pipetting of 2 fluids in a microfluidic channel and easily carried out by a biologically-trained end-user, without the use of highly specialized equipment. The microfluidic devices are easy to fabricate as they only require a microfluidic channel with a square flow area.

VFP was first used to generate 3D-VoCs by Bischel et al.¹⁴, who demonstrated that the method was not only simple to perform but also allows the formation of straight-, curved- and even bifurcated 3D-VoCs. Furthermore, sequential patterning of different layers of hydrogel supports the development of multi-layered lumens and different tissue specific cell types can be added to the hydrogel, demonstrating the flexibility of the methodology¹⁵⁻¹⁷. However, when implementing the protocol proposed by Bischel et al., we found that the resulting lumens have a tapered shape, i.e. a significant narrowing of the luminal diameter occurs along the length of the sample, as shown in **chapter 2**. This tapering of the lumen generates a gradient of wall-shear stress (WSS) when perfused, making it difficult to control haemodynamics and interpret results. We therefore sought methods to optimize luminal shapes such that they were compatible with perfusion studies. We demonstrate that by simply extending the entry length of the microfluidic-channel during VFP, the resulting lumens were uniform in diameter over their whole length. This scaffold is therefore capable of generating equal shear stress in the sample when perfused. This small adjustment to the original protocol resulted in lumens suitable for perfusion studies, with comparable quality as those generated with (needle)template-based approaches but retaining the scalability and ease of the original work.

Controlling OoC perfusion

A major obstacle in the use of perfusable OoC platforms is the scalability of controlled, unidirectional perfusion for extended periods of time. When medium refreshment is the only requirement, using gravity alone is sufficient to replenish the nutrients inside the microfluidic devices^{18,19}. However, when

biomechanical forces are important, more control is needed. Positive displacement pumps like syringe and peristaltic pumps are the standard for controlled perfusion as they are intuitive and straightforward to set-up. To increase throughput, OoCs can be connected via fluidic-networks to perfuse simultaneously using a single pump which is referred to as “multiplexing”. However as described in **chapter 3**, positive displacement pumps have limitations when used for the perfusion of OoCs. Due to the lack of control of mechanical stress in the OoCs, these positive displacement pumps can be detrimental to experimental success. Cell debris formation from dead, dying or detached cells, often occurs in OoC devices and can block microfluidic channels, damaging fragile (engineered) tissue structures. Furthermore, dimensional variation in OoCs does not allow for accurate control of mechanical parameters when multiplexing samples. This is because individual sample variation changes flow distribution and alters the intended mechanical stress, limiting the throughput per fluidic perfusion unit. **Chapter 3** describes a fluidic perfusion platform for the controlled and continuous recirculation of fluid in OoCs. This platform addresses 3 key limitations of the currently available systems when used for the perfusion of OoC.

Firstly, by regulating perfusion with a controlled pressure difference across the OoCs, rather than controlling the flowrate, multiplexing of samples using a single perfusion setup becomes possible. Because perfusion parameters of the individual samples are not changed when other samples have variable dimensions, intact samples are protected from unwanted mechanical stress when others become obstructed.

Secondly, pressure driven fluidic systems often require complex fluidic circuits using actively controlled valves to switch fluidic direction to generate continuous unidirectional flow²⁰. To simplify the recirculation, we developed a passively controlled hydraulic analogue to a Graetz-rectifier bridge, used in electrical AC/DC converters. The cell culture medium can be recirculated indefinitely by simply switching the pressure from the medium reservoirs when the liquid levels run low. This fluidic circuit can easily be implemented with inexpensive, off-the-shelf components allowing scaling of experiments with fewer electric components.

Finally, we also demonstrated that thermal mass-flowrate-sensors generally used in Lab-on-a-Chip devices are not suitable for long-term OoC perfusion. Due to fouling of the sensor when making measurements in cell culture medium, readouts become less accurate resulting in lower measured than reality. This inaccuracy has implications for the interpretation of the applied mechanical stimulation and should be avoided. This sensor fouling also hinders use of long term recirculation algorithms as pressure driven recirculation requires switching from one direction to another. We found that by using pressure sensors to measure the liquid level of the medium

reservoir, the precise timing of recirculation can be determined in a fail-safe manner. By combining these developments with commercially available pressure controllers, we were able to develop a flexible, controlled and unidirectional long-term perfusion platform that can be used for different of OoC devices without modification.

Multiplexing of 3D-VoCs with intrinsic variation

An important feature for the adaption of OoC for biomedical research is the ability to replicate experimental condition for multiple samples simultaneously. As already mentioned, blood flow is a vital physiological variable for blood vessels as the biomechanics resulting from blood flow are key modulators of cellular signal transduction and have to be taken into consideration for modelling a cellular response^{21,22}. By scaling the flowrate with the luminal diameter, these biomechanical variables can be scaled and different physiological conditions can be modelled in tractable models. However as described in **chapter 4**, 3D-VoCs have an intrinsic lumen diameter variation due to method of fabrication, sample handling and cellular response²³⁻²⁵. Also, sample deformation when subjected to an applied force combined with a mural-cell response, referred to as (vascular) compliance, contribute to this (intended) diameter variation²⁶. This intrinsic variation hinders multiplexing as it does not allow accurate control of the mechanical parameters when perfused. Standardising experimental conditions in each channel would then require either (i) individual pumps, set at flow-rates corrected for sample diameter or (ii) only select channels with similar diameters, which limits throughput significantly since not all samples, and valuable resources, can be used for experiments. **Chapter 4** describes a solution to bypass intrinsic variation of luminal diameters within 3D-VoCs to enable multiplexing perfusion and increasing sample numbers in a single perfusion experiment. We described a fluidic circuit board (FCB) specifically designed to standardise WSS for 3D-VoCs for a wide range of luminal diameters and ensure this is equal in all channels. The FCB relies on a tailored, fixed hydraulic resistance that scales the flowrate in lumens within a range of possible luminal diameters. The induced flow-rate of an individual 3D-VoC will generate a comparable WSS when equal pressure is applied. By allowing diameter variance rather than focusing on reducing it, more samples can be addressed using the same set of perfusion parameters and therefore allows for increasing the throughput per FCB. Using the perfusion platform we developed in **chapter 3**, the internal pressure can also be controlled, allowing independent regulation of the circumferential stress and the WSS. This can be used, for instance, to model effects of high (blood) pressure compared to low using the same WSS. Using this platform, we demonstrated that the morphology of hiPSC-ECs is influenced by both parameters as expected. By mimicking flow conditions of a vein, the cells adjusted their cytoskeleton accordingly. Future investigation of specific biomarkers will be

needed; however, the system presented can become a valuable tool to promote and investigate different endothelial phenotypes in various physiologically relevant conditions.

Controlling the formation of a perfusable capillary network

The vascular model as discussed above, is an easy-to-fabricate 3D-VoCs which can be used for various purposes. However, the model does oversimplify important aspects of the structural and biomechanical properties of the capillary vasculature. For instance, peripheral blood cells have the same dimensions as the capillary diameter. As a result, they are deformed when passing through the capillary^{27,28}. The resulting biomechanical forces on both the peripheral and endothelial cells are therefore not solely the result of continuous fluid flow. Furthermore, mural-cell interaction involves complete wrapping around the endothelial capillary, which cannot be achieved with large lumens.

The most accessible method to engineer a complex microvascular is cellular self-assembly. Endothelial cells can be mixed with mural and tissue specific cells inside a hydrogel where they form a capillary bed by themselves. However, these capillary beds all have different dimensions, which makes downstream analyses laborious as matching haemodynamic stimulation with phenotype becomes location depended²⁹. Also, it has been shown that adding different cellular components not only influence the cellular responses but also influences the formation and dimensions of the network formed³⁰. Controlling and equalizing the haemodynamic forces becomes impracticable which adds additional experimental variation between conditions. Furthermore, the majority of the self-assembled vessels are in fact larger than *in vivo* capillaries^{29,30}.

Chapter 5 describes a method to engineer and control the dimensions of a perfusable complex capillary network. To engineer capillary vessels with a predefined network, we use on-chip guided cellular self-assembly. To generate these scaffolds, we used a commercial system (called Primo, from Alveole) for UV-hydrogel patterning to construct a vascular capillary-network. To guide the hiPSC-ECs into the pre-determined perfusable format we patterned a rectangular channel with a fixed height of 50 μm composed of gelatine Gelatin methacryloyl (GelMA) inside a microfluidic device. GelMA is a widely used UV-curable hydrogel where mechanical and chemical properties can be tailored to specific needs by varying the UV-dose, concentration or premixing with other UV curable ECM components.

Using these hydrogel scaffolds we discovered a remarkable behaviour of hiPSC-ECs. When the cells are located in a channel with a width larger than 50 μm , they form an EC monolayer which covers both the walls and the ceiling of the fluidic channel. However, when the hydrogel channels were

smaller than 30 μm , the hiPSC-ECs that were seeded did not form vertical walls of endothelium but instead formed round, tubular structures.

This result suggests that by confining ECs, a predefined capillary network can be engineered. Compared to alternatives of generation true capillary structures like 2-Photon laser-ablation³¹ or laser-cavitation³² the used method is less technical complicated and easy to scale, as working designs can also be patterned using mask-lithography.

However some limitations need to be addressed before the protocol is advantageous for *in vitro* modelling. Due to the small and confined culture environment the fragile cell structures can be easily over-stressed and therefore the fluidic handling needs to be optimized. It is therefore desirable to employ a Fluidic Circuit Board to automatize and control the fluidic handling, so that operator manipulation can be minimized or circumvented³³.

Altogether, the advantages of the methods presented in this thesis bring OoC technology closer to biologists as end-users. We developed simple protocols to generate 3D-VoCs with various dimensions from 350 μm all the way down to even the smallest capillary with a diameter of 10 μm . The VoCs developed were all reproducible to produce, perfusable and implementable in biology lab, supporting steps towards the development of better *in vitro* models of vasculature. Importantly, the methodologies were all scalable in production, with up to 24 samples in one run by a single operator. This allows the simultaneous generation of sufficient technical replicates from a single experiment for different structural and functional readouts.

Future perspectives

The methods described in this work allow for the development of complex and physiologically relevant *in vitro* vascular models. Nevertheless, further refinement of the technology will be necessary before widespread adoption of OoC-technology is likely. A selection of points that particularly need refining are discussed in the following sections.

Microfluidic handling

Advances in microfabrication allow the miniaturization of cell culture devices, reducing the amount and volume of reagents and cells required, allowing better control of mechanical stress and the application of chemical gradients. However, miniaturization increases the complexity of manual handling. For instance, preventing evaporation of cell culture medium inside small devices is important as it can change concentrations of culture medium components very quickly. Furthermore, the simple insertion of a normal pipette-tip inside a fluidic channel can generate enough mechanical stress to damage delicate cellular structures.

Automated liquid handling systems could help address these limitations; however, this would require the standardization of microfluidic interfaces and

at present, no current standard can fit all purposes. Different OoCs also require different interfaces to connect with external pumping systems for example. Devices such as the Translational Organ-on-chip Platform (TOP), currently being developed in the University of Twente, is one example of how one interface can be used to accommodate many different chip devices and systems which can be very helpful in bringing the technology to the end users³⁴. The transition of the TOP system to a commercial project is eagerly awaited by many since it offers substantial flexibility in chip design yet does not require customised solutions to regulate fluidic flow.

Use of new Biomaterials

Although the models presented in this thesis do not use (living) animal models, reagents derived from animals are still widely used for the production of the necessary hydrogels. For instance, the extracellular matrix Collagen I, is generally extracted from bovine- or rat-tails and GelMA is derived from pigs. Matrigel, also an important component of many hiPSC differentiation protocols and assays, is extracted from sarcomeres induced in mice. Since these extracellular matrix components are animal derived, they are accompanied by batch-to-batch variation which means that assays often require re-optimisation when a new batch is used^{35,36}. Recombinant alternatives are often too expensive to be a feasible alternative for the generation of hydrogels, or they are ineffective as replacements. Recent advances in the development of biomaterials indicate that these should now be further explored. Materials like polyethylene glycol (PEG) linked with RDG (or other sequence)peptides that recognize receptors^{37,38} on the cell surface can be engineered on the basis of animal free- and chemically defined reagents and will increase the reproducibility and availability of essential OoC reagents³⁹.

Use of genetically encoded reporter lines

hiPSC-derived cells are beginning to change the field of not only stem cell biology as such but also drug discovery and disease modelling. This is in part because of their ability to generate all cell types of the human body and in part because they can be derived from patients with genetic or somatic disease; they thus may encompass a complete patient genotype. New developments in gene targeting and the introduction of transgenes has also provided opportunities to generate genetically encoded reporter lines, either to identify specific cell types⁴⁰ or to measure functional parameters such as calcium ion flux and action potentials of electrically active cells^{41,42}. Complex models can be generated and imaged in real time using these fluorescent readouts of cell type or function in 3D making it possible to collect information during experiments rather than only terminally, at the end-point of the experiment^{40,43,44}.

Using OoCs to accelerate drug discovery

Envisioning a future where all drugs are tested in a patient-specific model in a personalised way prior administration is already tempting but may only be a long-term outcome of the type of research described here and only for selected conditions. Nevertheless, there are more immediate and practical applications of OoC technology. For tissues that are closer to those in organs of the body because they are cultured in OoC devices, opportunities arise to study physiology and disease in humans at the cellular level.

Multiplexed devices using patient-genotypes, such as described in this thesis, will allow parallel analysis of drug or cellular responses with the number of biological replicates needed for robust conclusions without the risk for patients. Furthermore, if fluid flow-through can be collected and the cells can be extracted it will be possible to obtain multi-omics data parameters to feed *in silico* predictions of disease pathways and drugs that could be used to target them^{45,46}. OoCs can link and validate all databases of Genomics, Transcriptomics, Proteomics and Metabolomics to answer the important question: how can we improve human health? OoCs can be a stepping stone in the right direction.

References

- 1 Ingber, D. E. Human organs-on-chips for disease modelling, drug development and personalized medicine. *Nat Rev Genet* **23**, 467-491, doi:10.1038/s41576-022-00466-9 (2022).
- 2 Horvath, P. *et al.* Screening out irrelevant cell-based models of disease. *Nat Rev Drug Discov* **15**, 751-769, doi:10.1038/nrd.2016.175 (2016).
- 3 Guimarães, C. F., Gasperini, L., Marques, A. P. & Reis, R. L. The stiffness of living tissues and its implications for tissue engineering. *Nat Rev Mater* **5**, 351-370, doi:10.1038/s41578-019-0169-1 (2020).
- 4 Dewey, C. F., Jr., Bussolari, S. R., Gimbrone, M. A., Jr. & Davies, P. F. The dynamic response of vascular endothelial cells to fluid shear stress. *J Biomech Eng* **103**, 177-185, doi:10.1115/1.3138276 (1981).
- 5 Estrada, R., Giridharan, G. A., Nguyen, M. D., Prabhu, S. D. & Sethu, P. Microfluidic endothelial cell culture model to replicate disturbed flow conditions seen in atherosclerosis susceptible regions. *Biomicrofluidics* **5**, 32006-3200611, doi:10.1063/1.3608137 (2011).
- 6 Orlova, V. V. *et al.* Vascular defects associated with hereditary hemorrhagic telangiectasia revealed in patient-derived isogenic iPSCs in 3D vessels on chip. *Stem Cell Rep* **17**, 1536-1545, doi:10.1016/j.stemcr.2022.05.022 (2022).
- 7 Busek, M., Aizenshtadt, A., Amirola-Martinez, M., Delon, L. & Krauss, S. Academic User View: Organ-on-a-Chip Technology. *Biosensors (Basel)* **12**, doi:10.3390/bios12020126 (2022).
- 8 Cochrane, A. *et al.* Advanced in vitro models of vascular biology: Human induced pluripotent stem cells and organ-on-chip technology. *Adv Drug Deliv Rev* **140**, 68-77, doi:10.1016/j.addr.2018.06.007 (2019).
- 9 He, M., Martin, M., Marin, T., Chen, Z. & Gongol, B. Endothelial mechanobiology. *APL Bioeng* **4**, 010904, doi:10.1063/1.5129563 (2020).
- 10 Halaidych, O. V. *et al.* Inflammatory Responses and Barrier Function of Endothelial Cells Derived from Human Induced Pluripotent Stem Cells. *Stem Cell Rep* **10**, 1642-1656, doi:10.1016/j.stemcr.2018.03.012 (2018).
- 11 Orlova, V. V. *et al.* Functionality of endothelial cells and pericytes from human pluripotent stem cells demonstrated in cultured vascular plexus and zebrafish xenografts. *Arterioscler Thromb Vasc Biol* **34**, 177-186, doi:10.1161/ATVBAHA.113.302598 (2014).
- 12 Helle, E., Ampuja, M., Antola, L. & Kivela, R. Flow-Induced Transcriptomic Remodeling of Endothelial Cells Derived From Human Induced Pluripotent Stem Cells. *Front Physiol* **11**, 591450, doi:10.3389/fphys.2020.591450 (2020).
- 13 Saffman, P. G. & Taylor, G. The Penetration of a Fluid into a Porous Medium or Hele-Shaw Cell Containing a More Viscous Liquid. *Proc R Soc Lon Ser-A* **245**, 312-&, doi:DOI 10.1098/rspa.1958.0085 (1958).
- 14 Bischel, L. L., Lee, S. H. & Beebe, D. J. A practical method for patterning lumens through ECM hydrogels via viscous finger patterning. *J Lab Autom* **17**, 96-103, doi:10.1177/2211068211426694 (2012).
- 15 Herland, A. *et al.* Distinct Contributions of Astrocytes and Pericytes to Neuroinflammation Identified in a 3D Human Blood-Brain Barrier on a Chip. *Plos One* **11**, e0150360, doi:10.1371/journal.pone.0150360 (2016).
- 16 Bischel, L. L., Beebe, D. J. & Sung, K. E. Microfluidic model of ductal carcinoma in situ with 3D, organotypic structure. *Bmc Cancer* **15**, 12, doi:10.1186/s12885-015-1007-5 (2015).
- 17 Bischel, L. L., Young, E. W., Mader, B. R. & Beebe, D. J. Tubeless microfluidic angiogenesis assay with three-dimensional endothelial-lined microvessels. *Biomaterials* **34**, 1471-1477, doi:10.1016/j.biomaterials.2012.11.005 (2013).
- 18 Wang, Y. I., Abaci, H. E. & Shuler, M. L. Microfluidic blood-brain barrier model provides in vivo-like barrier properties for drug permeability screening. *Biotechnol Bioeng* **114**, 184-194, doi:10.1002/bit.26045 (2017).
- 19 Wang, Y. I. & Shuler, M. L. UniChip enables long-term recirculating unidirectional perfusion with gravity-driven flow for microphysiological systems. *Lab Chip* **18**, 2563-2574, doi:10.1039/c8lc00394g (2018).
- 20 Vivas, A., van den Berg, A., Passier, R., Odijk, M. & van der Meer, A. D. Fluidic circuit board with modular sensor and valves enables stand-alone, tubeless microfluidic flow control in organs-on-chips. *Lab Chip* **22**, 1231-1243, doi:10.1039/d1lc00999k (2022).

- 21 Dai, G. *et al.* Distinct endothelial phenotypes evoked by arterial waveforms derived from atherosclerosis-susceptible and -resistant regions of human vasculature. *Proc Natl Acad Sci U S A* **101**, 14871-14876, doi:10.1073/pnas.0406073101 (2004).
- 22 Amaya, R., Pierides, A. & Tarbell, J. M. The Interaction between Fluid Wall Shear Stress and Solid Circumferential Strain Affects Endothelial Gene Expression. *Plos One* **10**, e0129952, doi:10.1371/journal.pone.0129952 (2015).
- 23 de Graaf, M. N. S. *et al.* Scalable microphysiological system to model three-dimensional blood vessels. *APL Bioeng* **3**, 026105, doi:10.1063/1.5090986 (2019).
- 24 van Steen, A. C. I. *et al.* Transendothelial migration induces differential migration dynamics of leukocytes in tissue matrix. *J Cell Sci* **134**, doi:10.1242/jcs.258690 (2021).
- 25 Chrobak, K. M., Potter, D. R. & Tien, J. Formation of perfused, functional microvascular tubes in vitro. *Microvasc Res* **71**, 185-196, doi:10.1016/j.mvr.2006.02.005 (2006).
- 26 Dessalles, C. A., Ramon-Lozano, C., Babataheri, A. & Barakat, A. I. Luminal flow actuation generates coupled shear and strain in a microvessel-on-chip. *Biofabrication* **14**, doi:10.1088/1758-5090/ac2baa (2021).
- 27 Secomb, T. W., Hsu, R. & Pries, A. R. Motion of red blood cells in a capillary with an endothelial surface layer: effect of flow velocity. *Am J Physiol Heart Circ Physiol* **281**, H629-636, doi:10.1152/ajpheart.2001.281.2.H629 (2001).
- 28 Hogan, B., Shen, Z., Zhang, H., Misbah, C. & Barakat, A. I. Shear stress in the microvasculature: influence of red blood cell morphology and endothelial wall undulation. *Biomech Model Mechanobiol* **18**, 1095-1109, doi:10.1007/s10237-019-01130-8 (2019).
- 29 Kim, S., Lee, H., Chung, M. & Jeon, N. L. Engineering of functional, perfusable 3D microvascular networks on a chip. *Lab Chip* **13**, 1489-1500, doi:10.1039/c3lc41320a (2013).
- 30 Wan, Z. *et al.* A Robust Method for Perfusable Microvascular Network Formation In Vitro. *Small Methods* **6**, e2200143, doi:10.1002/smt.202200143 (2022).
- 31 Arakawa, C. *et al.* Biophysical and biomolecular interactions of malaria-infected erythrocytes in engineered human capillaries. *Sci Adv* **6**, eaay7243, doi:10.1126/sciadv.aay7243 (2020).
- 32 Enrico, A. *et al.* 3D Microvascularized Tissue Models by Laser-Based Cavitation Molding of Collagen. *Adv Mater* **34**, e2109823, doi:10.1002/adma.202109823 (2022).
- 33 Vollertsen, A. R. *et al.* Modular operation of microfluidic chips for highly parallelized cell culture and liquid dosing via a fluidic circuit board. *Microsyst Nanoeng* **6**, 107, doi:10.1038/s41378-020-00216-z (2020).
- 34 Vollertsen, A. R. *et al.* Facilitating implementation of organs-on-chips by open platform technology. *Biomicrofluidics* **15**, 051301, doi:10.1063/5.0063428 (2021).
- 35 Aisenbrey, E. A. & Murphy, W. L. Synthetic alternatives to Matrigel. *Nat Rev Mater* **5**, 539-551, doi:10.1038/s41578-020-0199-8 (2020).
- 36 Nguyen, E. H. *et al.* Versatile synthetic alternatives to Matrigel for vascular toxicity screening and stem cell expansion. *Nat Biomed Eng* **1**, doi:10.1038/s41551-017-0096 (2017).
- 37 De Mel, A., Jell, G., Stevens, M. M. & Seifalian, A. M. Biofunctionalization of Biomaterials for Accelerated in Situ Endothelialization: A Review. *Biomacromolecules* **9**, 2969-2979, doi:10.1021/bm800681k (2008).
- 38 Ruoslahti, E. RGD and other recognition sequences for integrins. *Annual Review of Cell and Developmental Biology* **12**, 697-715, doi:10.1146/annurev.cellbio.12.1.697 (1996).
- 39 Hersel, U., Dahmen, C. & Kessler, H. RGD modified polymers: biomaterials for stimulated cell adhesion and beyond. *Biomaterials* **24**, 4385-4415, doi:https://doi.org/10.1016/S0142-9612(03)00343-0 (2003).
- 40 Roberts, B. *et al.* Systematic gene tagging using CRISPR/Cas9 in human stem cells to illuminate cell organization. *Mol Biol Cell* **28**, 2854-2874, doi:10.1091/mbc.E17-03-0209 (2017).
- 41 Joshi, J., Rubart, M. & Zhu, W. Optogenetics: Background, Methodological Advances and Potential Applications for Cardiovascular Research and Medicine. *Front Bioeng Biotechnol* **7**, 466, doi:10.3389/fbioe.2019.00466 (2019).
- 42 Lee, S. Y. *et al.* Optogenetic control of iPS cell-derived neurons in 2D and 3D culture systems using channelrhodopsin-2 expression driven by the synapsin-1 and calcium-calmodulin kinase II promoters. *J Tissue Eng Regen Med* **13**, 369-384, doi:10.1002/term.2786 (2019).
- 43 Yiangou, L. *et al.* Optogenetic Reporters Delivered as mRNA Facilitate Repeatable Action Potential and Calcium Handling Assessment in Human iPSC-Derived Cardiomyocytes. *Stem Cells* **40**, 655-668, doi:10.1093/stmcls/sxac029 (2022).
- 44 Jiang, Y. *et al.* An Ultrasensitive Calcium Reporter System via CRISPR-Cas9-Mediated Genome Editing in Human Pluripotent Stem Cells. *iScience* **9**, 27-35, doi:10.1016/j.isci.2018.10.007 (2018).

Chapter six

- 45 Norris, J. L. *et al.* Integrated, High-Throughput, Multiomics Platform Enables Data-Driven Construction of Cellular Responses and Reveals Global Drug Mechanisms of Action. *Journal of Proteome Research* **16**, 1364-1375, doi:10.1021/acs.jproteome.6b01004 (2017).
- 46 Hasin, Y., Seldin, M. & Lusis, A. Multi-omics approaches to disease. *Genome Biology* **18**, doi:10.1186/s13059-017-1215-1 (2017).

Addendum

Summery

To improve the predictive capability of pre-clinical models and reduce the use of animal models in drug discovery and disease modelling, advanced *in vitro* models are being developed. These microphysiological systems (MPS) or “Organs-on-Chip” (OoC) are being developed to include all aspects of the human physiology to improve the *in vitro* cellular response. OoCs combined with differentiated human induced pluripotent stem cells (hiPSC) allow the use of cells with patient specific genotypes and aid the development of personalized and precision medicine.

In this thesis, the development of tractable models of the vasculature is described. These models allow for the combination of hiPSC-derived vascular and tissue specific cells with haemodynamics to recapitulate essential stimuli of blood vessels.

In **Chapter 1**, the importance of blood vessels for organ function, drug transport, and the immune response are described. The endothelial cell (EC) phenotype is essential for proper organ function and drug response. Next, various cell sources used in biomedical research, including hiPSC-derived ECs, are summarized. Haemodynamics are essential for the vascular phenotype and to include these important modulators, 3D-VoCs were developed. Finally, common methodologies are described to engineer 3D-Vessels-on-Chips.

Chapter 2 describes a scalable methodology to generate hydrogel scaffolds that can be used for seeding of hiPSC-derived vascular cells. It uses a microfluidic technique called viscous finger patterning (VFP) and the protocol comprises simply of sequentially pipetting 2 fluids with different viscosities. These scaffolds are fully perfusable to apply realistic haemodynamic forces. The described method results in uniform lumens, important for perfusion studies.

Chapter 3 describes a fluidic perfusion platform using pressure controllers optimized for long term perfusion of 3D-OoCs. It also describes a simple distributing Fluidic Circuit Board (FCB) to increase throughput.

Chapter 4 describes a FCB specifically designed for the perfusion of the 3D-VoC described in **chapter 2**. The microfluidic circuit can be used with a range of luminal diameters, while maintaining the same mechanical stimulation, multiple samples can be perfused simultaneously. Using this system, the EC morphology changes in response to both circumferential stress and wall shear stress (WSS) are investigated.

Chapter 5 describes a methodology to engineer a perfusable model of the smallest capillaries of the vascular system. A specialized method is described to print a complex capillary bed into a hydrogel that can be seeded with vascular cells. The mechanical properties of this hydrogel can be tuned for

tissue specific conditions and allows to design complex capillary beds to generate complex flow patterns.

Chapter 6 is a general discussion of the findings presented in this thesis and summarizes the advantages of the methods and work still required to improve the presented models. Because the described methods do not rely on highly specialized materials and techniques, it brings OoC-technology closer to the end-user: the biomedical researcher. Scope for future work in the field is also proposed.

Samenvatting

Om preklinisch onderzoek te verbeteren en om het gebruik van dierproeven te reduceren wordt er een nieuwe klasse *in vitro* modellen ontwikkeld. Deze micro-fysiologische systemen of "Organen-op-Chips" worden ontwikkeld om alle aspecten van menselijke fysiologie na te bootsen, om op deze manier de *in vitro* cellulaire reactie te verbeteren. De OoCs worden gecombineerd met humaan geïnduceerde stamcell (hiPSC) afgeleide cellen en kunnen worden gebruikt voor de ontwikkeling van gepersonaliseerde en precisie medicijnen.

In deze thesis worden vasculaire modellen beschreven die hiPSC-vasculaire cellen combineert met hemodynamische krachten om een verbeterde cel-reactie te verkrijgen.

In **hoofdstuk 1** wordt het belang van bloedvaten voor orgaanfunctie, medicijntransport en immuunreactie beschreven. Bloedvaten zijn aan de binnenkant bedekt met endotheelcellen, omringd met pericyten of gladde spiercellen. Hemodynamica is een belangrijke modulator van het vasculaire fenotype. Om deze mechanische krachten op een realistische wijze na te bootsen worden er 3D-Vaten-op-Chips (3D-VoCs) ontwikkeld.

Hoofdstuk 2 beschrijft een schaalbare methode voor het maken van een 3D-VoC. Het maakt gebruik van micro-fluidica voor het vormen van hydrogel in de vorm van een bloedvat. Het protocol bestaat uit het sequentieel injecteren van 2 vloeistoffen met verschillende viscositeit, zodat er een lumen wordt gevormd. Het protocol is uit te voeren zonder het gebruik van speciale materialen en is daarom uitermate geschikt om op te schalen. De beschreven 3D-VoCs zijn in staat om uniforme en realistische hemodynamische krachten te genereren.

Hoofdstuk 3 beschrijft een perfusie systeem speciaal ontwikkeld voor de perfusie van 3D-Organen-op-Chips. Dit systeem is in staat om voor langere perioden accuraat multiplex perfusie te garanderen en maakt gebruik van simpele concepten zodat het een goedkoop alternatief is voor het opschalen van OoC experimenten.

Hoofdstuk 4 beschrijft een fluidisch circuit bord (FCB) speciaal ontwikkeld voor de perfusie van 3D-VoCs zoals beschreven in **hoofdstuk 2**. Omdat de 3D-VoCs een inherente variatie hebben door het gebruik van zachte hydrogels is het accuraat multiplexen van perfusie niet mogelijk. Het fluidisch circuit van dit FCB is zo ontworpen dat de diameters van de 3D-VoCs in een domein van diameters mogen zitten terwijl de hemodynamische krachten gelijk blijven. Op deze manier is het mogelijk om dezelfde perfusie parameters te gebruiken voor verschillende diameters en kunnen er meerdere 3D-VoCs tegelijkertijd getest worden. Met dit systeem is de morfologie van endotheelcellen onder perfusie onderzocht.

Hoofdstuk 5 beschrijft een methode om de complexe haarvaten te reconstrueren op een chip. Het maakt gebruik van een speciale laser om een capillaire structuur in een hydrogel te printen en kan gebruikt worden om vasculaire cellen te kweken met complexe stroming.

Tot slot worden er in **hoofdstuk 6** de resultaten van dit proefschrift en de toekomstperspectieven beschreven. Door het gebruik van gespecialiseerde materialen en apparaten zoveel mogelijk te limiteren kunnen de beschreven methoden makkelijker worden geïmplementeerd. De beschreven methodes brengen OoC technologie dichterbij de eindgebruiker: de biomedisch onderzoeker. Verwacht wordt dat de OoC technologie het medicijnonderzoek kan versnellen door het linken en valideren van meerdere biomedische databanken om zo beter inzicht te geven in de werking van nieuwe en oude medicijnen in de populatie.

Curriculum Vitae

Mees de Graaf was born on August 13th, 1985 in Weesp, the Netherlands. After graduating from secondary school, he pursued a career in yacht racing before obtaining his bachelor-degree in Life Science and Technology at Leiden University and Delft University of technology. During his bachelor he did an internship at Crucell BV (now Janssen Vaccines), engineering expression cassettes for Adenovirus based vaccines.

His bachelor research focused on protein engineering for solid-state nanopore sequencing under the supervision of Prof. Dr. Chirlmin Joo and Prof. Cees Dekker at the department of Bionanoscience at Delft University of Technology.

He obtained his master degree Life Science and Technology at Leiden University, focusing on chemical biology, immunology and biomaterials. His master research at Leiden University Medical Center under the supervision of Dr. Valeria Orlova, focused on the development of 3D-vascular models using human induced pluripotent stem cells.

He continued this work during his PhD-research under the supervision of Dr. Valeria Orlova and Prof. Dr. Christine Mummery, and further developed 3D-hiPSC derived vascular models. The results are presented in this thesis.

List of publications

Scalable microphysiological system to model three-dimensional blood vessels

Mees N. S. de Graaf, Amy Cochrane, Francijna E. van den Hil, Wesley Buijsman, Andries D. van der Meer, Albert van den Berg, Christine L. Mummery, and Valeria V. Orlova
APL Bioengineering 3, 026105, 2019;
<https://doi.org/10.1063/1.5090986>

Multiplexed blood–brain barrier organ-on-chip

M. Zakharova, M. A. Palma do Carmo, M. W. van der Helm, H. Le-The, **Mees N. S. de Graaf**, V. Orlova, A. van den Berg, A. D. van der Meer, K. Broersend and L. I. Segerink
Lab Chip, 20, 3132-3143, 2020;
<https://doi.org/10.1039/D0LC00399A>

Rapid Prototyping of Organ-on-a-Chip Devices Using Maskless Photolithography

Dhanesh G. Kasi, **Mees N. S. de Graaf**, Paul A. Motreuil-Ragot, Jean-Phillipe M. S. Frimat, Michel D. Ferrari, Pasqualina M. Sarro, Massimo Mastrangeli, Arn M. J. M. van den Maagdenberg, Christine L. Mummery and Valeria V. Orlova
Micromachines 13 (1), 49, 2022;
<https://doi.org/10.3390/mi13010049>

Pressure-Driven Perfusion System to Control, Multiplex and Recirculate Cell Culture Medium for Organs-on-Chips

Mees N. S. de Graaf, Aisen Vivas, Andries D. van der Meer, Christine L. Mummery, Valeria V. Orlova
Micromachines, 13(8), 1359, 2022;
<https://doi.org/10.3390/mi13081359>

Three-Dimensional Vessels-on-a-Chip Based on hiPSC-derived Vascular Endothelial and Smooth Muscle Cells

Merve Bulut, Marc Vila Cuenca, **Mees N.S. de Graaf**, Francijna E. van den Hil, Christine L. Mummery, Valeria V. Orlova
Current Protocols, 2, e564;
<https://doi.org/10.1002/cpz1.564>

On-chip analysis of glycolysis and mitochondrial respiration using extra-cellular flux validated in human-induced pluripotent stem cell

Stefanie Fuchs, Ruben W.J. van Helden, Maury Wiendels, **Mees N.S. de Graaf**, Valeria V. Orlova, Christine L. Mummery, Berend J. van Meer, Torsten Mayr
Materials Today Bio, 17, 100475
<https://doi.org/10.1016/j.mtbio.2022.100475>

Multiplexed fluidic circuit board for continues controlled perfusion of 3D blood vessels on a chip

Mees N. S. de Graaf, Aisen Vivas, Dhanesh G. Kasi, Francijna E. van den Hil, Robbert Passier, Albert van den Berg, Christine L. Mummery, Andries D. van der Meer, Valeria V. Orlova
Lab Chip, 2023, 23, 168-181
<https://doi.org/10.1039/D2LC00686C>

In preparation

Perfusable Engineered capillary using hydrogel guided self-assembly on-Chip and human iPSC-derived vascular cells

Mees N. S. de Graaf, Dhanesh G. Kasi, Francijna E. van den Hil, Arn van Maagdenberg, Christine L. Mummery, Valeria V. Orlova

Acknowledgement

This thesis is the result of the work and effort of many people who I would like to thank for their inspiration and support.

Valeria, thank you for the opportunity to be part of your research group.

Dear Christine, thank you for your guidance, patience and understanding during my research.

Lisa, I could not go without your support. I am so grateful you helped me out with everything possible, both in and out of the lab. Both Gia and I will miss you.

To the rest of Orlova group; Amy, Marc, Dennis, Dhanesh, Ulgu and Merve. I wish you all the best for the future.

All the people of the NOCI-consortium. Although I am going to miss you all, I will not miss the apenkoppen. I wish you all the very best on your own projects!

I would like to express my gratitude to the whole department of Anatomy and Embryology especially to Bert, for the help in scavage hunts through the depths of the LUMC.

Andries van der Meer, Wesley Buijsman and Aisen Vivas from the University of Twente, for their technical input and ingenuity.

Lennard Voortman and Annelies Boonzaier-van der Laan of the Light Microscopy Facility for their support over the years. You helped me to show to everybody what I was doing, probably the most important part of this work.

The late Mevrouw Esther Elkerbout, her interest in our research made this work possible. We are all very grateful for her contributions to our lab.

My dear parents, thank you for all the support during my whole academic career. My sister and brothers; Mare, Dirk and Olivier, thank you for being there for me when I was around.

Lieve Gia, het was zo'n feest om dit werk met jou te hebben mogen delen. Hier staan ook jouw eerste experimenten en jouw eerste poster presentatie in Graz. We gaan nog samen veel ontdekken.

Lieve Luc, dank voor je gezelschap in de nacht tijdens het laatste deel van dit verhaal. Samen schrijven is veel gezelliger, maar nu kunnen we weer vooral samen spelen.

Dear Banu, the greatest sacrifices come from the partner of the PhD-candidate. Thank you for being next to me with your wit and inspiration, your support and understanding and most of all: your patience.

It is finished now (really).

Addendum

nunc est bibendum

Stellingen behorend bij het proefschrift:

Engineered 3D-Vessels-on-Chip to study effects of dynamic fluid flow on human induced pluripotent stem cell derived-endothelial cells

1. **3D-VoCs produced with VFP can be used to apply uniform shear stress to all cells.**
This thesis
2. **TEQ resistors improve the throughput of 3D-VoC perfusion by allowing variation instead of eliminating it.**
This thesis
3. **hiPSC-derived endothelial cells can swiftly adapt to changing haemodynamic conditions.**
This thesis
4. **Confined hiPSC-derived endothelial cells prefer to adopt a tubular morphology; unconfined hiPSC-derived endothelial cells prefer to form monolayers.**
This thesis
5. **Vascular models without correct haemodynamics should be considered a pathophysiological model.**
This has implications for the translation to *in vivo*.
Ming He et al.(2020) APL Bioengineering 4, 010904
6. **3D-models can be better disease models than 2D models.**
However the clues are well hidden.
Orlova et al. (2022) Stem Cell Reports 12;17(7):1536-1545
7. **Sticking feathers to something does not make it a chicken**
By only looking at the parameters a model should have, one could overlook the features it shouldn't.
Tyler M. Lu et al. (2021) PNAS vol 118(8) e2016950118
8. **"It is evident that the use of human organ chips instead of animal models for drug development and as living avatars for personalized medicine is ever closer to realization."**
Donald E. Ingber (2022) Nature Reviews Genetics, 23, pages 467–491
Now legislation is in, the field must now deliver.
9. **Anything worth doing, is worth doing right.** *Raoul Duke (1971)*
Refine and validate a proof of concept before generating data.
10. **Assumptions are the mother of all failures.** *Eugene Fordsworthe*
For interdisciplinary research assumptions are essential, however it is vital to understand how to extrapolate other people's assumptions.
11. **"All problems in microfluidics are small".** *Lisa van den Hil (2020)*
Most problems encountered in microfluidic prototyping are not intrinsic to the design but fabrication and are easy to solve. However, the smallest imperfection still has detrimental effects on success and morale.
12. **"Mother Nature is a mad scientist".** *Kramer (1997)*
Attempting to recapitulate it on a chip, makes you appreciate it even more.